

Modifying ultrasound waveform parameters to control,
influence, or disrupt cells

Thesis by

David Reza Mittelstein

In Partial Fulfillment of the Requirements for

the degree of

Doctor of Philosophy

The logo for the California Institute of Technology (Caltech), featuring the word "Caltech" in a bold, orange, sans-serif font.

CALIFORNIA INSTITUTE OF TECHNOLOGY

Pasadena, California

2020

(Defended February 26, 2020)

© 2020

David Reza Mittelstein

ORCID: 0000-0001-8747-0483

All Rights Reserved

ACKNOWLEDGEMENTS

I am so grateful for having had the incredible opportunity to undergo my graduate training at the California Institute of Technology. This institution and the wonderful people that I have taught me so much about science, professionalism, and life in general. I am deeply grateful for the guidance by my mentor Mory Gharib, who supported and led me throughout these formative years in my career as a scientist.

I feel incredibly lucky to have had the opportunity and support to take on the very ambitious oncotripsy research project and to have the support of three different principle investigators at Caltech. Mory Gharib, who first recruited me to the project and empowered me to work with multiple investigators at Caltech. Michael Ortiz, for his depth of knowledge, research advice, and for his faith in me to put his theory of oncotripsy to the test. And a special note of gratitude for Mikhail Shapiro, who has not only co-advised me throughout my PhD, but constantly provided his insight on how to plan experiments and the overall direction of my research. I would also like to thank Dr. Tim Colonius, for leading my candidacy and thesis defense committees.

I would also like to thank our clinical and research collaborators from City of Hope. Dr. Yuman Fong and Dr. M Houman Fekrazad who I worked with in the early stages of the project were excellent role models for my MD/PhD training who grounded their scientific curiosity with a deep concern and focus on patient care. I am also very grateful to Dr. Peter Lee and his laboratory group who have taken the mantle of oncotripsy experiments and have brought their keen minds and vast knowledge about immunotherapy that will be necessary to take this project to the next level.

My fellow researcher colleagues have been an incredibly important part of my learning experience here at Caltech, and I would like to give an extra special acknowledgement to them. First of course, to Stefanie Heyden who introduced me to the project and fielded many of my first solid mechanics questions. Then to Erika Figueroa who I have worked with consistently over the years as she has refined the oncotripsy theory with the experimental data. To Jian Ye, the postdoctoral researcher at City of Hope who helped us to complete the oncotripsy experiments and is guiding the next

stage of the research, I thank you profoundly. And finally to Spencer Bryngelson who assisted in some cavitation modeling. I have learned so much from all of you and greatly appreciate your friendship and support as we worked together on this challenging yet rewarding project.

I am grateful for the funding sources that have allowed me to pursue this project at Caltech and receive a world-class education in medical engineering in the process. I am grateful for the Medical Engineering program for funding my first year at Caltech. My research would not have been possible without the support of the Jones Family Trust Caltech Innovation Initiative (CI²) and the funding of the Amgen Bioengineering Research Program.

I would like to commend all the contributors to the experimental design and running of the oncotripsy project. Ankita Roychoudhury is a committed undergraduate student with a great work ethic, a keen mind, and an optimistic attitude that will serve her well throughout her future career. Sara Leyre Troyas, while only here for a few months, made a remarkable contribution to the oncotripsy theory.

I've had the good fortune, due to being co-advised, to have been able to make friends in two of the most incredible lab groups at Caltech. I've truly enjoyed working along side with you all, and hanging out together as well. I've always felt as though I was part of the family of researchers here, and I greatly appreciate everyone for being so welcoming and understanding.

Lastly, I want express my most profound gratitude to my loving and supportive family. My parents Soheila Mirhashemi, and Caltech alumni Michael Mittelstein, have been so wonderful in guiding me throughout life, and I would not have had the opportunities to succeed at Caltech without them. I would also like to thank my brother Daniel, for keeping me grounded and always being there for me when I needed him. As well as the rest of my family, cousins, aunts, uncles, etc. who have all been so supportive. My dear friends from all parts of my life for their constant support and inspiration. And finally, I want to thank my partner Helena Yu, who has always supported and believed in me. I love her dearly and could not have accomplished what I have in life without her.

ABSTRACT

Ultrasound can be focused into deep tissues with millimeter precision to perform non-invasive ablative therapy for diseases such as cancer. In most cases, this ablation uses high intensity ultrasound to deposit non-selective thermal or mechanical energy at the ultrasound focus, damaging both healthy bystander tissue and cancer cells. Here we describe an alternative low intensity pulsed ultrasound approach known as “oncotripsy” that leverages the distinct mechanical properties of neoplastic cells to achieve inherent cancer selectivity. We show that when applied at a specific frequency and pulse duration, focused ultrasound selectively disrupts a panel of breast, colon, and leukemia cancer cell models in suspension without significantly damaging healthy immune or red blood cells. Mechanistic experiments reveal that the formation of acoustic standing waves and the emergence of cell-seeded cavitation lead to cytoskeletal disruption, expression of apoptotic markers, and cell death. The inherent selectivity of this low intensity pulsed ultrasound approach offers a potentially safer and thus more broadly applicable alternative to non-selective high intensity ultrasound ablation.

In this dissertation, I describe the oncotripsy theory in its initial formulation, the experimental validation and investigation of testable predictions from that theory, and the refinement of said theory with new experimental evidence. Throughout, I describe how careful modifications to the ultrasound waveform directly can significantly impact how the ultrasound bio-effects control, influence, or disrupt cells in a selective and controlled manner.

PUBLISHED CONTENT AND CONTRIBUTIONS

Mittelstein, David R., Ye, Jian, Schibber, Erika F., Roychoudhury, Ankita, Martinez, Leyre Troyas, Fekrazad, M. Housman, Ortiz, Michael, Lee, Peter P., Shapiro, Mikhail G. and Gharib, Morteza, *Selective ablation of cancer cells with low intensity pulsed ultrasound*. Applied Physics Letters, 2020. **116**(1): p. 013701. <https://doi.org/10.1063/1.5128627>

DRM participated in the conception of the project, developed the collaboration among labs to experimentally investigate the oncotripsy theory. DRM designed, constructed, and performed the experiments *in vitro*, prepared the data, and was the lead author in the writing the manuscript

Schibber, Erika F., **Mittelstein, David R.**, Gharib, Mory, Shapiro, Mikhail G., Lee, Peter Ortiz, Michael A *Dynamical Model of Oncotripsy by Mechanical Cell Fatigue: Selective Cancer Cell Ablation by Low-Intensity Pulsed Ultrasound (LIPUS)*. Proc Math Phys Eng Sci, 2020. **476**(2236): p. 20180692. <https://doi.org/10.1098/rspa.2019.0692>

DRM designed, constructed, and performed the experiments *in vitro*, prepared the data, and participated in the writing of the manuscript. As the experimentalist, DRM was consulted by EFS as she was developing the theoretical framework of this model.

Bar-Zion, Avinoam, Nourmahnad, Atousa, **Mittelstein, David R.**, Yoo, Sangjin, Malounda, Dina, Abedi, Mohamad, Lee-Gosselin, Audrey, Maresca, David and Shapiro, Mikhail G., *Acoustically Detonated Biomolecules for Genetically Encodable Inertial Cavitation*. bioRxiv, 2019: p. 620567. <https://doi.org/10.1101/620567>

DRM participated in designing, constructing the experimental setup, performing, and analyzing data from a subset of these experiments.

Yoo, Sangjin, **Mittelstein, David R.**, Hurt, Robert, Lacroix, Jerome, Shapiro, Mikhail G., *Focused ultrasound excites neurons via mechanosensitive calcium accumulation and ion channel amplification*, bioRxiv, 2020.05.19.101196; doi: <https://doi.org/10.1101/2020.05.19.101196>

DRM participated in designing, constructing the experimental setup, performing, and analyzing data from a subset of these experiments.

Wu, Di, Baresche, Diego, Cook, Colin, Malounda, Dina, Maresca, David, Abundo, Maria Paulene, **Mittelstein, David R.**, Shapiro Mikhail G., *Genetically encoded nanostructures enable acoustic manipulation of engineered cells*, bioRxiv 691105; doi: <https://doi.org/10.1101/691105>

DRM participated in designing and fabricating the experimental setup for these experiments.

TABLE OF CONTENTS

Acknowledgements.....	iii
Abstract.....	v
Published Content and Contributions	vi
Table of Contents	viii
List of Illustrations.....	x
List of Tables.....	xi
<i>Chapter 1</i> Ultrasound as a Cancer Therapeutic Modality	1
1.1 Introduction	1
1.2 Advances in Cancer Therapy due to Enhanced Tumor Selectivity	1
1.3 Therapeutic Ultrasound	2
1.4 Linear Acoustics: Reflection, Interference, Scattering, Refraction	4
1.5 Non-linear Acoustics: Attenuation, Radiation Force, Cavitation.....	9
1.6 Ultrasound Mechanisms of Biological Effects.....	11
1.6.1 Heating (Thermal Ultrasound)	12
1.6.2 Non-Thermal Ultrasound	12
1.7 Thesis Outline	14
<i>Chapter 2</i> Theoretical Framework of Oncotripsy	15
2.1 Introduction	15
2.2 Oncotripsy as a Inherently Selective Ablation Approach	15
2.3 Transient Response Simulations Oncotripsy (Heyden).....	17
2.4 Modification of Low Intensity Pulsed Ultrasound Waveform for Oncotripsy Effects	22
<i>Chapter 3</i> LIPUS cancer-selective ablation of oncotripsy	30
3.1 Introduction	30
3.2 Experimental Support of Oncotripsy Theory	30
3.2.1 Approach.....	30
3.2.1 Results.....	31
3.2.1 Discussion	34
3.3 Cellular Biomolecular and Structural Responses to LIPUS.....	34
3.3.1 Approach.....	34
3.3.2 LIPUS cytodisruption associated with cytoskeletal damage and activation of apoptotic, immunogenic cell death pathways	35
3.3.3 LIPUS results in translational motion of cells	37
3.3.4 Discussion	38
3.4 Ultrasound Mechanisms Involved in LIPUS Bioeffects	38
3.4.1 Approach.....	38
3.4.2 Standing waves are necessary for LIPUS cytodisruption	38
3.4.3 Cell mediated cavitation is required for LIPUS cytodisruption.....	41
3.4.4 LIPUS cytodisruption attenuated in solid media	44
3.4.5 Discussion	45
3.5 Conclusion.....	46
3.6 Methods	47

3.6.1 High Throughput Ultrasound Experiments	47
3.6.2 Analysis of biomolecular pathways of cytodisruption	49
3.6.3 Investigation of standing waves and acoustic radiation force in cytodisruption.....	49
3.6.4 Role of cavitation in cytodisruption	50
3.6.5 Solid model investigation.....	51
3.6.6 High speed camera visualization of cell deformation	51
3.7 Supplemental Figures	52
<i>Chapter 4</i> Refinement of Oncotripsy Theory, Future Directions	54
4.1 Introduction	54
4.2 Inconsistencies between Transient Response Oncotripsy Model and Experimental Data..	54
4.3 Reduced Cytoskeleton Constitutional Model (Figueroa)	56
4.4 Conclusions	60
<i>Chapter 5</i> Alternative Waveforms for Cellular Modification / Control	61
5.1 Introduction	61
5.2 Modification of Pulsed Ultrasound Parameters.....	61
5.2 Ultrasound to Detonate Acoustically Active Biomolecules	63
5.2.1 Background	63
5.2.2 High Speed Camera Experiments	65
5.3 High Intensity Focused Ultrasound for Thermal Control.....	68
5.3.1. Background	68
5.3.2 Thermal Control with PID Circuit	69
<i>Chapter 6</i> Conclusions and future experiments	71
6.1 Introduction	71
6.2 Investigation of the Mechanism of Oncotripsy	71
6.3 Application of Oncotripsy to Solid Tumor Models.....	74
6.4 Synergistic capabilities of oncotripsy with chemotherapy and immunotherapy.....	75
6.5 Closed loop device for tuning oncotripsy parameters	76
6.6 Conclusion.....	77
APPENDIX A: Keller-Miksis Simulation of Cavitating Bubble in Ultrasound Field.....	78
APPENDIX B: Scripts, Protocols, and Models on Github	84
References.....	85

LIST OF ILLUSTRATIONS

Figure 1-1 Ultrasound Reflecting Off Of Interface.....	6
Figure 1-2 Spatial Standing Wave Pattern.....	6
Figure 1-3 Refraction of Ultrasound.....	8
Figure 1-4 Multi-Element Beam Steering.....	9
Figure 2-1 Finite Element Mesh for Transient Oncotripsy Theory	18
Figure 2-2 Lowest, non-rigid-body eigenfrequencies versus cell cancerous potential.....	19
Figure 2-3 Time Domain Simulation of Cellular Oscillation at Two Different Frequencies	20
Figure 2-4 Transient response of cancer cell and healthy simulated cell to ultrasound stimulation.....	21
Figure 2-5 Pulsed Sinusoidal Waveform Degrees of Freedom.....	23
Figure 2-6 Relationship between Acoustic Pressure and Intensity in Focused Ultrasound Beams.....	24
Figure 2-7 Spatial-Peak Temporal-Average Intensity of Ultrasound	26
Figure 2-8 Mechanical Index	27
Figure 3-1 Screening reveals ultrasound parameters that induce cancer-cell selective cytodisruption.	33
Figure 3-2 Ultrasound cytodisruption associated with apoptotic and pro-phagocytic pathways.....	36
Figure 3-3 High-speed video demonstrates no large-scale cell deformation during ultrasound insonation.....	37
Figure 3-4 Standing waves required for LIPUS cytodisruptive effect.....	40
Figure 3-5 Cell-mediated cavitation is mechanically necessary for cytodisruption.	43
Figure 3-6 Cells suspended in gel medium undergo attenuated cytodisruption in response to our targeted LIPUS parameters.	45
Figure 3-7 No temperature change induced by LIPUS.....	52
Figure 3-8 Flow cytometry gates used for phagocytic, apoptotic analysis.....	53
Figure 4-1 Schematics of Improved Computational Oncotripsy Models Error! Bookmark not defined.	
Figure 4-2 Evolution of Cytoskeletal Element Damage during Ultrasound Stimulation	57
Figure 4-3 Cytoskeletal damage evolution with reduced dynamical oncotripsy model	59
Figure 5-1 Ultrasound Waveforms for Different Bioeffects.....	62
Figure 5-2 Gas vesicles as nuclei for inertial cavitation	64
Figure 5-3 Ultrafast optical imaging of GV-seeded bubble formation and cavitation	67
Figure 5-4 PID Control System Used for Thermal Control.....	70
Figure 6-1 Proposed setup for high speed fluorescence imaging	73
Figure 6-2 Poor image acquisition of fluorescent dyes with high speed microscopy.....	74
Figure A-1 Simulated Bubble Emissions Simulated by Keller-Miksis Equation.....	82
Figure A-2 Radius over Time for Simulated Bubble.....	81

LIST OF TABLES

Table 1-1 Acoustic Impedance Values Per Tissue.....	7
Table 1-2 Ultrasound Attenuation Coefficients	10
Table 2-1 Waveform Parameters Suggested for Oncotripsy Effect.....	29
Table 3-1 Cell Models Tested.....	32
Table A-1 Variables and Coefficients for Keller-Miksis Simulation	80

Chapter 1

ULTRASOUND AS A CANCER THERAPEUTIC MODALITY

1.1 Introduction

In this chapter, I will discuss the necessary background required to discuss ultrasound's use as a cancer therapeutic modality. First, I will provide an overview of the current state of cancer therapy and some key challenges that remain in the selective targeting of cancer cells necessary for safe and effective therapy. Next, I will introduce ultrasound as a therapeutic modality, describing its history of medical use and characteristics that make it well suited for use in the human body. Following this, I will provide an overview of the relevant acoustic physics that are necessary for understanding the interaction of ultrasound in the body. Finally, I will conclude with a literature review including several clinical and pre-clinical applications of ultrasound as a cancer ablative tool, with a critical analysis of their shortcomings in addressing cancer therapy. This chapter shall serve as an introduction into my dissertation about designing inherently cancer selective ultrasound waveforms.

1.2 Advances in Cancer Therapy due to Enhanced Tumor Selectivity

Cancer, a disease of rapidly dividing mutated human cells within the body, poses several unique challenges for clinicians. Chief among them has developing a therapeutic modality that selectively destroys the cancer cells without harming the surrounding healthy cells in the body. Historically cancer therapies have used extremely radical surgical removals of afflicted body parts, and it was only in the late 1970s that the cytostatic chemotherapeutic regimes of bleomycin, vinblastine, or cisplatin became mainstays of cancer therapy coupled with local surgical interventions. However, these therapies mechanism of action to target the cell cycle exerts significant stress on healthy cells in the body and thus induces significant side effects. The dosages and treatment regimens are constantly limited in their applicability due to the risks of excessive chemotherapy [1]. Over the past fifty years, cancer therapy has made great strides by developing

more precise therapeutic instruments and intervention that enhancing the capability to target the cancer cells selectively. New chemotherapeutic agents including small molecule inhibitors or monoclonal antibodies, immunotherapeutic interventions such as chimeric antigen receptor T cells or checkpoint inhibitors, or additional biological therapies such as oncolytic viruses have all been developed to enhance tumor selectivity by taking advantage of the unique molecular biology of cancer cells for a more selective approach [2, 3]. Surgical interventions have also greatly benefitted from enhanced imaging technology [4] and new minimally invasive or fully non-invasive ablative techniques [5] that can provide more spatially precise removal or ablation of cancer tissue from the human body. By enhancing tumor selectivity, more aggressive therapeutic approaches can be taken without causing the harmful side effects.

However, several cancers today continue to pose significant challenges for therapy, specifically because they are difficult to target selectively. Many of the most therapeutically challenging cancers involve a solid tumor mass with poorly defined borders and invasion into healthy tissue [6, 7]. Moreover, the solid tumor microenvironment can have areas of high interstitial pressure and poor perfusion that prevent the penetration of chemotherapeutic agents [8]. A clinical need exists for a new paradigm of targeting cancer cells that can be combined with existing therapies to enhance the selectivity and therefore applicability of cancer ablation. In this dissertation, I plan to discuss how ultrasound can offer a solution for this clinical need.

1.3 Therapeutic Ultrasound

Ultrasound has been used widely in the medical field as a low-cost, real-time diagnostic/imaging system since the 1960s, and is considered a mature and well-developed area of research. Ultrasound imaging is also an active and productive field of research with numerous breakthroughs in medical imaging including elastography, super resolution imaging, multiple element array transducers, functional/targeted contrast agents, and many other developments [9]. Less known however are the numerous experimental and clinically proven applications of ultrasound as a therapeutic modality. Acoustic energy can penetrate well within the body's soft tissue, with a depth of up to 20 cm depending on the signal frequency, and can be focused to

deposit energy at depth within the body. It also boasts sub-millimeter resolution, also dependent on frequency, which can be used for high-resolution images, but also to spatially target ultrasound used as therapy. As such since its development, clinicians and researchers have found multiple therapeutic applications that take advantage of the unique physical properties of ultrasound [10].

In fact, a historical review shows that therapeutic applications for ultrasound predated its use as an imaging modality. The modern ultrasound transducer technology of sandwiched quartz piezoelectric crystals arose as an outgrowth of sonar technology used in World War 1 to detect submarines using echo-location [11]. This system generates ultrasound waves by applying an alternating electric voltage across a piezo-electric material. In response to electrical stimulation, this piezo element undergoes tension and compression, thus generating pressure waves in the surrounding media. With the advent of acoustic lenses, materials that could be shaped to allow the focusing of acoustic energy at depth within living tissue, therapeutic applications for acoustic energy quickly emerged. The field of therapeutic ultrasound began in 1938, with devices that provided mild heating within the body as an anti-inflammatory therapy for conditions such as tendinitis or bursitis [12]. With further enhancements in focused ultrasound, the field of high intensity focused ultrasound was initiated in 1942. High intensity focused ultrasound (HIFU) used continuous waves of high intensity ultrasound that was focused to a specific target region in the body to thermally ablate undesirable tissue, forming cigar-shaped thermal lesions [13]. This technique carried the risk of unintentional adverse bio-effects due to mis-targeting of the ablative beam. However, the advantage of non-invasive tissue ablation led to some early use of the technology to ablate aberrant tissue in neurosurgery and later in tumor ablation [14]. In the 1960s, acoustic researchers began to investigate the mechanical effects of ultrasound, in the form of shock wave lithotripsy. Short bursts of very high pressure ultrasound began to be used as a standard of care for the treatment of kidney and bladder stones, as it again allowed for non-invasive destruction of the undesired material [15]. The safety of both these mechanical and thermal ultrasound therapies greatly improved with improved imaging and guidance systems in the 1980s – in particularly MRI-guided focused ultrasound machines allowed for HIFU to be applied to a wider variety of cancer ablation scenarios [16]. Currently ultrasound therapy combines both the thermal and mechanical aspects of ultrasound and is clinically used in many non-invasive tissue ablation

practices, including several tumors where surgical access is challenging or complex, with research being performed in a variety of applications from disruption of blood clots [17] to enhanced drug delivery into tissue or through the blood-brain barrier [18]. A key challenge in the field of ultrasound as a tumor ablation approach, similarly to as described above for other cancer therapies, is achieving sufficient target specificity to reduce the risk of off-target ablation. In this dissertation, we will discuss how careful control of the ultrasound waveform used may enhance the selectivity of the ultrasound ablative effect.

1.4 Linear Acoustics: Reflection, Interference, Scattering, Refraction

To provide a scientific context to our discussion of improving the safety margins for ultrasound ablation in cancer therapy, we will include a discussion of the acoustic properties of ultrasound and its relevance for producing bioeffects. Sound is mechanical energy comprised of longitudinal pressure waves that pass through a material medium via the action of elastic stresses and involving local compression and rarefaction. Ultrasound is a simply sound, where the frequency of these pressure waves is above the range of human hearing (>20 kHz). At low acoustic pressure, ultrasound waves propagate as described through the linear wave equation, where the rate of change of particle velocity is proportional to the negative of the gradient of acoustic pressure. This leads to a spatially distributed periodic pattern of compression and rarefaction that propagates through media with properties of compressibility and inertia. The square of the speed of wave propagation in this linear approximation is directly proportional to the media's pressure-density relation, and as such depends directly on the bulk material properties of the medium through which it propagates. The product of the speed of sound of a medium and its density gives the acoustic impedance of that medium which is an important acoustic property that describes the reflection and transmission of sound at a boundary [19].

When the pressure wave reaches an interface, a wave is reflected back while another wave is transmitted. The fraction of the wave that is reflected depends upon the mismatch of the impedance of the medium of the incident wave to that of the new medium the wave is entering, as demonstrated in Figure 1-1. The incident wave, the transmitted wave, and the reflected wave,

must obey the wave equation as well as the continuity of pressure and normal particle velocity boundary conditions. The human body contains many interfaces with slightly different acoustic impedances as organs, blood vessels, fat, and bones all have unique impedance values (Table 1-1). As such, an ultrasound wave transmitted into the body, will form many reflected signals that can be used to generate an image of the interior of the body [20]. The acoustic impedance also helps us to calculate the acoustic intensity of the ultrasound waveform. Acoustic impedance (Z) relates the particle velocity (v_0) to the acoustic pressure (p_0) at that position in a sound wave through $v_0 = p_0 / Z$. The instantaneous power per unit area in sound for a one-dimensional planar sound wave is $I(t) = p(t) * v(t)$, which in this formulation becomes $I(t) = p(t)^2 / Z$. Assuming a sinusoidal waveform, which is a valid assumption for low intensity, single frequency ultrasound waveforms, we arrive at an average intensity of $I_{avg} = p_0^2 / (2*Z)$ [19].

The waves described above are traveling waves, with areas of compression and rarefaction that propagate forward over time. The sum of two traveling waves passing opposite one another, which is achieved when a single standing wave reflects off a boundary and interferes with the incident wave, is referred to as a standing wave. This occurs due to the linearity of acoustic pressure that occurs with low intensity ultrasound. In these standing waves, a static spatial pattern of pressure nodes and anti-nodes appears as demonstrated in Figure 1-2. At nodes, the acoustic pressure remains zero due to destructive interference between the incident and reflected wave. At anti-nodes, the acoustic pressure oscillates with double the amplitude of the incident wave, due to the constructive interference of the two waves [19].

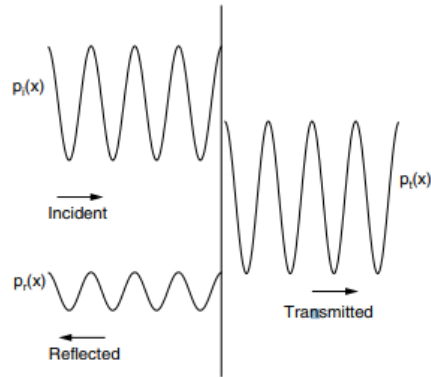


Figure 1-1 / Ultrasound Reflecting Off Of Interface

An incident traveling sound wave (pressure p_i) travels from tissue 1 (impedance Z_1) to tissue 2 (impedance $Z_2 = 2 * Z_1$). Acoustic mismatch between tissue leads to generation of reflected traveling wave (pressure p_r) and transmitted traveling wave (p_t) Reproduced from [19].

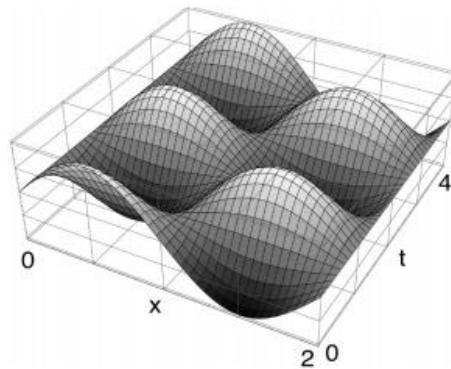


Figure 1-2 / Spatial Standing Wave Pattern

The following is the plot of an acoustic standing wave $f(x,t) = \sin(\pi x) * \cos(\pi t)$ demonstrating the nodes and antinodes of the pressure field evolving with time. Reproduced from [19].

tissue type	sound speed c_0 (m/s)	density ρ_0 (kg/m ³)	$Z =$ $\rho_0 c_0$ (Rayls)	B/A
air at STP	330	1.2	400	0.4
water at 20°C	1480	1000	1.48×10^6	5.0
water at 37°C	1530	990	1.51×10^6	5.4
blood	1585	1060	1.68×10^6	6
brain	1560	1035	1.62×10^6	6.5
breast	1510	1020	1.62×10^6	9.6
fat	1430	930	1.33×10^6	10.3
heart	1555	1060	1.65×10^6	5.8
kidney	1560	1050	1.64×10^6	9.0
liver	1580	1050	1.66×10^6	6.7
muscle	1580	1040	1.65×10^6	7.4
spleen	1565	1055	1.65×10^6	7.8
bone	3200	1990	6.36×10^6	-

Table 1-1 / Acoustic Impedance Values Per Tissue

Acoustic impedance values, measured in Rayls ($\text{kg m}^{-2} \text{s}^{-1}$) and non-linearity parameter (B/A) for various tissues and acoustic environments in the body. Reproduced from [20].

Ultrasound also experiences scattering when it passes through heterogeneous media with characteristic containing multiple reflectors. Scattering is required for ultrasound imaging as it is the interaction between the incident ultrasound wave and the various reflectors in the body that generates the reflected waves from which the ultrasound image is reconstructed. Agents that induce scattering can be categorized as specular or diffractive based on their size. Specular scattering agents generally have a characteristic length much larger than the wavelength of transmission, and cause a straightforward reflection of the ultrasound wave allowing the visualization of boundaries between different tissue types. Diffractive agents include small cysts or micro calcifications and up the texture of the ultrasound image conveying information about the tissues that are being imaged. Tissue in the body is largely heterogeneous, and different measures of heterogeneity can be representative of certain physiological or pathological conditions in organ systems. As such, ultrasound can provide information about the interior of organ systems along with the interfaces between different structures within the body [20].

Ultrasound also has the capability to refract as it passes at an angle from one medium to another with a different acoustic impedance. This is a consequence of the continuity of pressure and particle velocity required at the interface that maintains similar acoustic frequency. Huygen's principle, describing each point on a wavefront as a point source for a wavelet that defines the next wavefront illustrates this process effectively in Figure 1-3. The relevance of this for therapeutic ultrasound is that the capability to refract allows for the construction of acoustic lenses that can focus the acoustic energy into a small area. This allows for the localization of the ultrasound energy necessary for targeting of ultrasound induced bioeffects [20]. Multi-element arrays also have the ability to use electronic steering to focus ultrasound energy at depth by implementing a programmed pattern of delays in each of their array elements, show in Figure 1-4. Many modern therapeutic HIFU systems involve multi-element array to achieve spatially targeted therapeutic ultrasound ablation [19, 21].

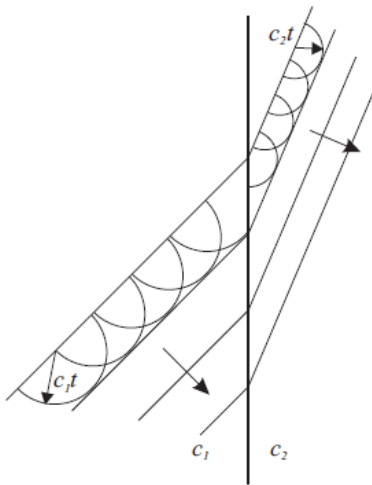


Figure 1-3 / Refraction of Ultrasound

Ultrasound wavefronts refract when moving into a different medium. Here with $c_2 < c_1$, the wavefront is refraction away from the normal of the boundary in an illustration of Huygen's principle. Reproduced from [20].

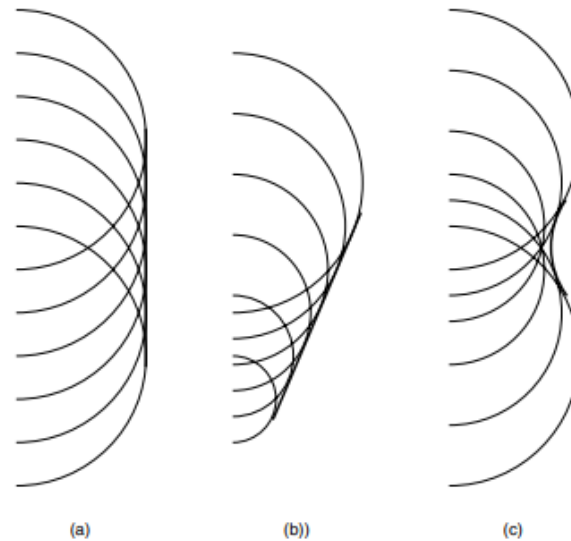


Figure 1-4 / Multi-Element Beam Steering

This illustration of a delayed-pulse phase array's function shows 5 point source transducer generating a) plane waves, b) downward steered plane waves, c) focused beam by altering the delay on each of transducer element. Reproduced from [19]

1.5 Non-linear Acoustics: Attenuation, Radiation Force, Cavitation

However, with higher-pressure ultrasound waves, the linear model begins to breakdown, and a more complete model that incorporates some non-linearities helps to describe some of the key behavior of ultrasound waves relevant for tumor ablation. Firstly, as the ultrasound passes through the body, it does not maintain all of its acoustic energy. A portion of the acoustic energy is converted into heat and dissipated throughout the tissue that the ultrasound is passing through. This process is referred to as attenuation, and has consequences for penetration depth of ultrasound in the body, but also for ultrasound's capability to be used as a thermal therapeutic agent. The acoustic energy loss is caused by viscous losses as particles in the media oscillate due to the pressure wave. Viscous friction converts some of this kinetic energy into heat, in a process highly

dependent on frequency and on the medium. In general, attenuation is much stronger at higher frequencies, as demonstrated by the positive exponential in Table 1-2 [20]. As such, ultrasound imaging of deep tissue generally involves lower frequency ultrasound transducer. Also, thermal ablation techniques tend to avoid very low frequencies in order to find a balance between penetration depth and heat generation [22].

tissue type	absorption coefficient (dB/cm/MHz ^y)	frequency dependence y
water at 20°C	2.17×10^{-3}	2
blood	0.14	1.21
brain	0.58	1.3
breast	0.75	1.5
fat	0.6	1
heart	0.52	1
kidney	10	2
liver	0.45	1.05
muscle	0.57	1
spleen	0.4	1.3
bone	3.54	0.9

Table 1-2 | Ultrasound Attenuation Coefficients

Attenuation coefficients for various tissue types, reproduced from [20]

Ultrasound can also apply a constant linear force on tissue. This is evident by observing the momentum balance that occurs at an interface where the ultrasound wave is completely reflected. A radiation pressure, force per area, is observed at this interface. Similarly, in medium where the ultrasound wave is attenuated as it passes through said medium, there is a corresponding radiation pressure caused by the momentum balance on a theoretical interface that is formed as the pressure wave decays. This pressure gradient corresponds to a force on the medium that leads to acoustic streaming or the acoustic radiation force [20]. The imaging modality known as ultrasound elastography takes advantage of this property to apply a shear force to tissue with a short pulse of high pressure ultrasound to apply a “tap” of radiation force to tissue, and then run diagnostic

imaging to observe the tissue responding to the applied shear force [23]. Acoustic radiation force has also been considered as a potential mechanism through which several low intensity ultrasound induced bioeffects have been observed. For example, low intensity ultrasound has been shown to stimulate or inhibit neurons from firing, a process known as ultrasound neuromodulation [24]. One potential theory for this mechanism, which is still not well understood, is acoustic radiation force applied on the tissue, which is mechanically transduced into the cells [25].

Gases in ultrasound fields also behave highly non-linearly. As ultrasound passes through a liquid medium, the local pressure is a sum of the ambient pressure and the acoustic pressure. When the acoustic pressure becomes very negative, the local pressure in the liquid can become negative, corresponding to a tensile force on the intermolecular bonds in the liquid. In response to these tensile forces, existing gas bubbles can rapidly expand or new bubbles can be formed within the fluid. As the pressure increases, the sizes can shrink. At low amplitude pressures, this causes a stable oscillation in bubble size that is referred to as stable cavitation. This can exert some mechanical forces on nearby structures. At higher pressures, rectified diffusion occurs as more gas diffuses into the bubble during expansion phase than diffuses out during compression phase. At a certain size, the bubble undergoes inertial collapse, a rapid reduction in radius caused by the pressure of the surrounding liquid. This inertial cavitation is highly non-linear and can lead to asymmetrical microbubble collapse and jetting [20].

1.6 Ultrasound Mechanisms of Biological Effects

This physical understanding of acoustics helps us to characterize how these ultrasound waves interact with cells in the body. Ultrasound bioeffects are a result of thermal or non-thermal mechanisms. Thermal effects occur with continuous wave ultrasound, where acoustic energy is deposited through attenuation in the focal area, temperatures can reach 80 degrees and lead to coagulative necrosis. Precisely shaped ultrasound waveforms can lead to sharp lesion boundaries, with separation between lethal and sub-lethal effects that are only a few cells thick. Non-thermal ultrasound effects are seen with pulsed ultrasound and include acoustic cavitation, acoustic radiation forces, and acoustic streaming [26].

1.6.1 Heating (Thermal Ultrasound)

Some of the earliest applications of ultrasound used unfocused transducer applied directly against the body to generate heat deep within tissue. This technique is still currently used today as a therapy for diseases of painful inflammation such as bursitis of the shoulder or tendonitis. Temporarily increasing the temperature of muscles, tendons, and other tissue improves blood flow which accelerates healing, enhance drug uptake, and promote pain relief [14]. With larger increases in temperature, cells can be subjected to conditions that cause them to suffer from hyperthermia, which has been briefly investigated as a cancer therapeutic approach to arrest growth. High intensity focused ultrasound (HIFU) is a non-invasive therapeutic modality used clinically for tumor ablation in prostate, breast, liver, pancreas, bone, and brain tumors [10, 26-29]. By producing local hyperthermia and destructive cavitation [30], HIFU induces cell lysis, increases chemotherapeutic uptake [28, 31], and stimulates systemic anti-tumor immune responses [29, 32]. However, high intensity ($I_{SPTA} > 100 \text{ W/cm}^2$) and high pressure ($> 10 \text{ MPa}$) focused ultrasound indiscriminately destroys healthy tissue as well as tumors [33, 34]. Consequently, safely implementing HIFU often requires costly MRI targeting [35] and is challenging in cancers near or invading into critical tissue [26].

1.6.2 Non-Thermal Ultrasound

Cavitation is used as a therapeutic modality in many different venues of medicine. High Intensity Focused Ultrasound (HIFU) uses sufficiently high-pressure ultrasound that both thermal and cavitation effects contribute to the tumor ablation. However, several medical approaches use cavitation exclusively to cause localized effects. Shockwave lithotripsy involve the administration of shockwaves, very high pressure, but single or few cycle pulses of ultrasound that converges on a renal calculi. The stone is then exposed to not only strong pressure gradients, but also cavitation vents that erode and shatter the stone [36]. Another such technique is phacoemulsification, where the lens of an eye clouded by cataracts can be broken down by localized low frequency high pressure ultrasound stimulation that breaks apart tissue at the tip of a surgical instrument [37].

Cavitation has also been investigated as a non-invasive tissue ablation technique, called histotripsy, where clouds of cavitating bubbles are maintained by a pulses of high intensity ultrasound that can mechanically disrupt tissue in a tight spatial focus with an apparatus similar to what is used for HIFU [38].

There is also a growing number of ultrasound bioeffects that fall under the category of mechanical (non-thermal) ultrasound, but whose mechanism of action still remains relatively poorly understood. Ultrasound induces mechanical stress in cells through shear stress and stretch/compression distributions near the cellular surface through microstreaming around bubbles. [39] Ultrasound can enhance the passage of drugs through cellular lipid bilayers. [40, 41] Metastatic cancer cells have a unique mechanical response to deformation compared to less malignant or senescent cells as measured through optical microscopy [42]. Studies show that highly metastatic epithelial breast cancer cells have a less dense cytoplasm and more pliable cytoskeleton [43]. Breast tumor cells also have differing compositions of fatty acids in their cell membranes compared to normal breast tissue [44]. Low intensity ultrasound may have a selectively strong effect on highly metastatic cancer cells [45]. Chemotherapy is complicated by non-specific chemotherapeutic agents and high interstitial pressure inside tumors due to poor vascularity and lymphatic drainage that prevents drug uptake. Ultrasound insonation, particularly in combination with microbubble contrast agents, can enhance the permeability of these areas to chemotherapy [46]. A study shows that ultrasound alone, without contrast agents, can also enhance uptake of the chemotherapeutic adriamycin in U937 suspension cell models [47]. In vivo studies suggest that ultrasound can enhance chemotherapeutic tumor control possibly through distribution of injected chemotherapeutic agents into poorly vascularized regions of a fibrosarcoma [48]. This technique was also shown to allow for lower doses of chemotherapeutic agents and still maintain localized chemotherapeutic effects, as demonstrated with low dose scutellarin therapy efficacy on human tongue cancer carcinoma xenograft when coupled with low intensity ultrasound [49].

Several approaches aim to increase ultrasound's specificity. Molecularly targeted contrast agents, such as microbubbles [50, 51] locally amplify ultrasound's disruptive effects, but are

challenging to deploy in tumors due to the agents' poor extravasation [52]. An alternative approach involves low intensity pulsed ultrasound (LIPUS). Low intensity ($I_{SPTA} < 5 \text{ W/cm}^2$) and low frequency ($< 1 \text{ MHz}$) pulsed ultrasound, as defined in [53], produces mechanical effects without hyperthermia, resulting in neurostimulation [54], chemotherapy uptake [46], and bone repair [46, 55, 56]. However, its ability to selectively ablate cancer cells has not been studied, and its mechanisms of action are not fully understood [57-59].

1.7 Thesis Outline

This thesis describes my research at Caltech investigating how modifications of ultrasound waveforms can lead to disparate ultrasound effects. Throughout my graduate studies, I have been involved in a variety of project using different ultrasound parameters optimized to generate distinct physical responses in biological tissue.

Chapter 2 describes the theory of oncotripsy that was originally conceived of by Stephanie Heyden and my attempts to formulate the theory as a set of testable predictions that can be investigated. Chapter 3 describes the experimental results of those testable predictions as well as an investigation into the mechanism of how low intensity pulsed ultrasound can cause cancer-cell selective cytodisruption. Chapter 4 describes the refinements to the oncotripsy theory run by Erika Figueroa based on the experimental results and the implications for future research of the oncotripsy theory and its potential clinical application. In Chapter 5, I also describe my involvement in other projects as a primer for the discussion of how alternative ultrasound waveforms can lead to alternative physical effects in biological tissue.

Chapter 2

THEORETICAL FRAMEWORK OF ONCOTRIPSY

2.1 Introduction

In this chapter, I discuss the theoretical framework behind the oncotripsy theory. The oncotripsy theory suggests that specifically tailored waveforms of ultrasound can selectively damage cancer cells by taking advantage of mechanical differences in their cellular structure that distinguishes them from healthy cells. Erika Figueroa and Stephanie Heyden performed the research work included in this chapter, and I was honored to have the opportunity to assist as we converged the experimental and theoretical work on this project. I will begin by describing the clinical need for such as cancer selective ablation technique and introducing oncotripsy. This will include a literature review of the various mechanical distinctions between healthy cells and cancerous cells and their implications for responding to ultrasound stimulation. Next, I will summarize the theoretical models that have been developed to model the cellular response to ultrasound by Heyden and Figueroa, with particular consideration to their implications for cancer therapy. Last I will introduce describe how an ultrasound waveform can be modified in order to take advantage of the oncotripsy effect.

2.2 Oncotripsy as a Inherently Selective Ablation Approach

The oncotripsy theory suggests that cell's mechanical response to ultrasound is highly dependent on their mechanical properties. As such, the biomechanical differences between cancerous and healthy cell types cause these cells to have different responses to ultrasound, allowing selective ablation of cancer cells with targeted ultrasound waveforms. By stimulating a cancer cell using ultrasound at a frequency it is sensitive, the theory predicts that cancer cells will undergo more rapid and high amplitude oscillation that lead to cell lysis whereas a healthy cell exposed to the same ultrasound parameters will remain unscathed.

There is ample evidence in biomechanical literature that a mechanical difference exists between cancer cell and healthy cell sub-populations. Cancer therapy approaches function by targeting the most rapidly dividing cancer cells, as these are the most problematic cells that can lead to disease prevention, metastasis, and other negative sequelae. By nature of being actively dividing, these cells are also likely to have several distinguishing biomechanical properties that may be exploited by an oncotripsy therapy. For example, atomic force microscopy measurements have suggested that cancer cells may have a more loosely organized cytoskeletal structure which corresponds to decreased cytoskeletal stiffness and altered cellular morphology [60-62]. Cells that are in the process of dividing will have more DNA content which is unpacked [63] thus influencing the mechanical properties of the nucleus. The increased cellular activity is also associated with an increase in the size of the nucleoli of cancer cells [64]. Magnetic resonance elastography performed on the liver have demonstrated distinct changes in viscoelastic properties in the cellular microenvironment associated with hepatic tumors [65]. In fact, the mechanical properties of cancer cells are sufficiently distinct from those of healthy cells that their deviation as measured through micro-pipette aspiration can be used as a metric of a cancer's metastatic potential [66, 67]. Overall, cancer cells' altered cellular/nuclear morphology, DNA content, nuclear-nucleolar volume ratios, cytoskeletal stiffness, and viscoelastic properties [60, 62, 65, 68] imply that they may be considered a mechanically distinct subpopulation from healthy cells, at least in the same tissue structural context.

The theory implies that a new paradigm of achieving cancer selectivity in therapy is possible. Rather than relying on positional information that distinguishes cells in a tumor from healthy tissue or relying on unique molecular targets that are expressed only by cancer cells, oncotripsy suggests that it is possible to target cancer cells for disruption based on their inherent mechanical properties. This has significant clinical implications. For example, oncotripsy theoretically does not require tumor tracking or the enforcement of therapeutic margins. By taking advantage of its cancer-cell selective mechanism, an oncotripsy system can administer therapy to an entire organ and only disrupt the invading cancer cells. This provides clinicians with a powerful and novel therapeutic technique to locally administer targeted cancer therapy without harming healthy tissue. Many of the most therapeutically challenging cancers involve a solid tumor mass

with poorly defined borders and invasion into healthy tissue [6, 7]. While HIFU may be unable to safely ablate these tumors, oncotripsy's mechanism may be specifically suited to targeting these invading cells.

Cancers with tissues that differ in mechanical properties of stiffness or structure from surrounding healthy tissue may be candidates for oncotripsy therapy. The treatment of glioblastoma multiforme (GBM), the most common primary brain tumor in adults, is a massive challenge in neuro-oncology due to the difficulty of establishing effective surgical margins in brain tissue [26, 69, 70]. However, the shear elastic moduli is substantially different between normal brain tissue and glioma tissues [68]. This contrast in mechanical properties between cancerous and non-cancerous cells suggests that oncotripsy may be a therapy to noninvasively destroy GBM. Similar applications for oncotripsy can be observed in liver and breast cancer. The liver is the second most common site for tumor metastases and the site of hepatocellular carcinoma (HCC), the fifth most common malignancy [71]. Current standard of care is surgical resection or transplantation [72] with ablation therapies used as a recourse. However, common liver metastases and HCC have a significantly different elastic moduli than normal liver parenchyma [65], making them an ideal potential candidate for oncotripsy therapy. Breast cancer is the leading cause of death among solid tumors in women, the most lethal phenotypes are highly invasive [61], and similar evidence exists of a cellular mechanical property mismatch between normal and metastatic cancer breast cells [73] suggesting an application for oncotripsy. Oncotripsy could also be effective at targeting hematological malignancies such as leukemia or lymphoma, or even circulating tumor cells, cancer cells that have hematogenously spread from primary tumor sites. Metastasis is a major cause of morbidity and mortality in patients suffering from cancer [63]. An oncotripsy system focusing over a major vein could disrupt circulating tumor cells before they have a chance to metastasize.

2.3 Transient Response Simulations Oncotripsy (Heyden)

Dr. Stephanie Heyden, from Dr. Michael Ortiz's solid mechanics laboratory at Caltech, posited the initial formulation of the oncotripsy theory that a cell's mechanical response to

ultrasound excitation may be frequency-dependent due to that cell's unique mechanical properties. This section will summarize the work and include figures from her published work [74]. They explored this theory by developing a geometric finite element model of a cell that allowed frequency-domain and time-domain analysis of excitation with ultrasound stimulation. The structural and physical properties of the simulation were populated from literature analyses of hepatocellular carcinoma cancer cells and healthy liver hepatocytes. This model included several simplifying assumptions, including neglecting the viscosity of the cells and the biological heterogeneity of mechanical properties present within each of the studied subpopulations. The cell modeled in this finite element model was an idealized set of three nested spheres, corresponding to the cytoplasm, nucleus, and nucleolus. This model also included elements that correspond to the spaces between these interfaces: the extracellular matrix, the cytoplasm, the nucleoplasm as shown in Figure 2-1. This preliminary numerical study used a Mooney-Rivlin-type strain energy density study. A full description of the computational methods and mechanical laws used to develop this model are beyond the scope of this dissertation, however its conclusions were key in informing our approach to this project.

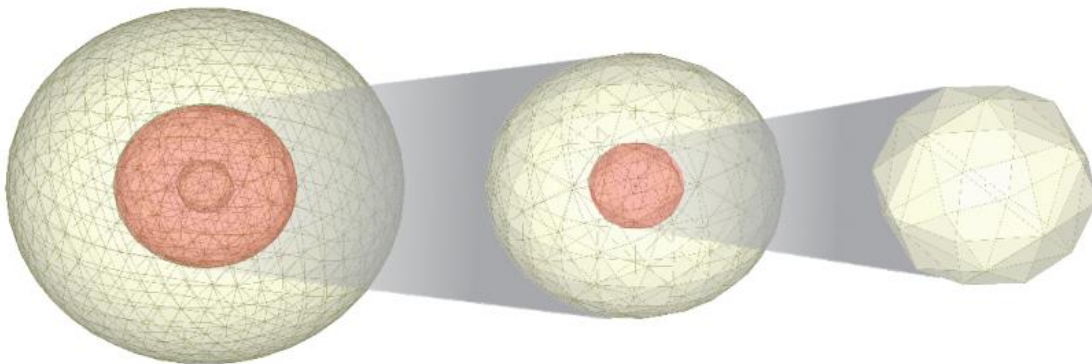


Figure 2-1 / Finite Element Mesh for Transient Oncotripsy Theory

The finite element model used in the transient response formulation of the oncotripsy theory as formulated by Stefanie Heyden incorporated three nested spheres that represent the plasma membrane, the nuclear membrane, and the nucleolus, as well as the extra-cellular space, the cytoplasm, and the nucleoplasm. Reproduced from [74]

Frequency-domain analysis revealed that the cellular model exhibited eigenfrequencies at which the cell model underwent resonant oscillation with the ultrasound stimulation. Moreover, a spectral gap existed between the eigenfrequencies of the healthy and cancer cell models. This suggested that an ultrasound frequency may exist at which the cancer cell undergoes a resonant response and oscillates very efficiently while healthy cells do not undergo as vigorous an oscillation. In other words, this analysis suggests a differential response between healthy and cancer cell types in response to specific waveforms of ultrasound.

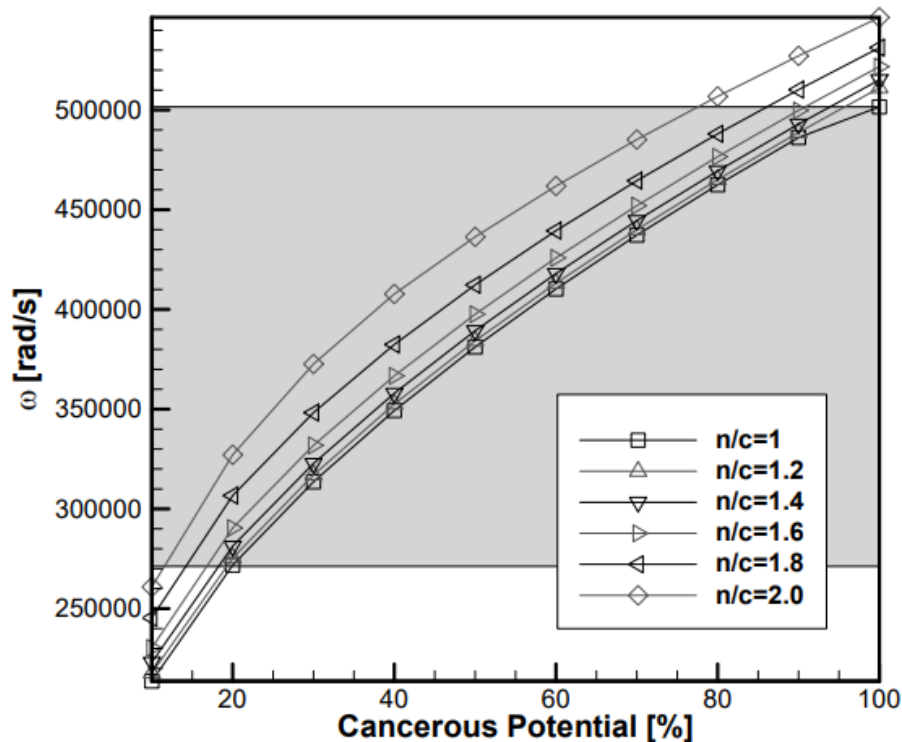


Figure 2-2 / Lowest, non-rigid-body eigenfrequencies versus cell cancerous potential

The first non-rigid body eigenfrequency for each cell model investigated through frequency-domain analysis of the finite element model analysis. The x-axis represents cancerous potential, which is a linear scaling of the physical properties of the cell model to be that of the noncancerous hepatocyte to the cancerous hepatocellular carcinoma cell based on literature review. Variance in

the ratio between nuclear volume to cytoplasmic volume (“n/c”) are also represented in the plot. This figure demonstrates a clear “spectral gap” between the cancerous and healthy cells resonant frequencies based on mechanical properties. Reproduced from [74]

This same model was used for time domain analysis which provided further insight into how this technique could be adopted for targeted cytodisruption based upon frequency and timing of ultrasound stimulation. The simulation demonstrated that the elements of the cell models had a growing oscillation in response to ultrasound stimulation. The growth rates of these oscillations were highly dependent on frequency of ultrasound stimulation and distinct for the cancer and healthy models.

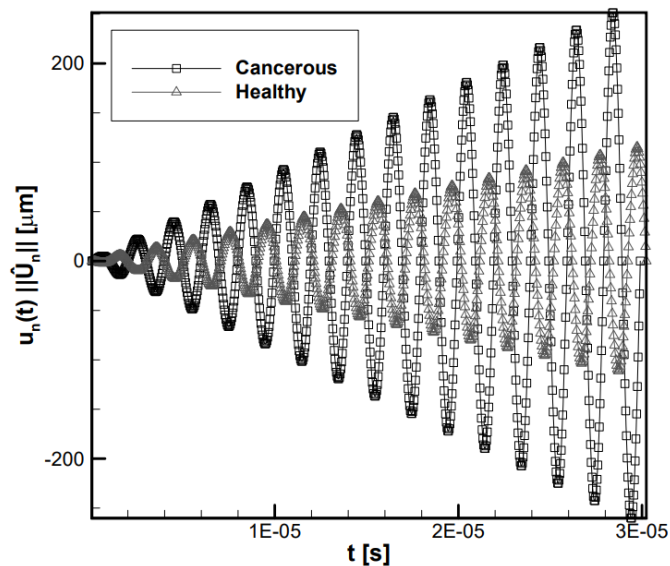


Figure 2-3 / Time Domain Simulation of Cellular Oscillation at Two Different Frequencies

Maximum element oscillation of cell model over time for two different resonant frequencies. This figure demonstrates that the oscillation growth rates of cancerous and healthy cells are distinct and frequency dependent. Reproduced from [74]

By assuming a threshold of oscillation amplitude above which cell death will occur, ultrasound frequencies that would achieve the desired outcome of cancer cell disruption while sparing healthy cells could be identified by comparing oscillation growth rates. In Figure 2-3, the plot on the right demonstrates a frequency of stimulation where the oscillation in the cancer cell model grows rapidly, while the healthy cell has a muted response.

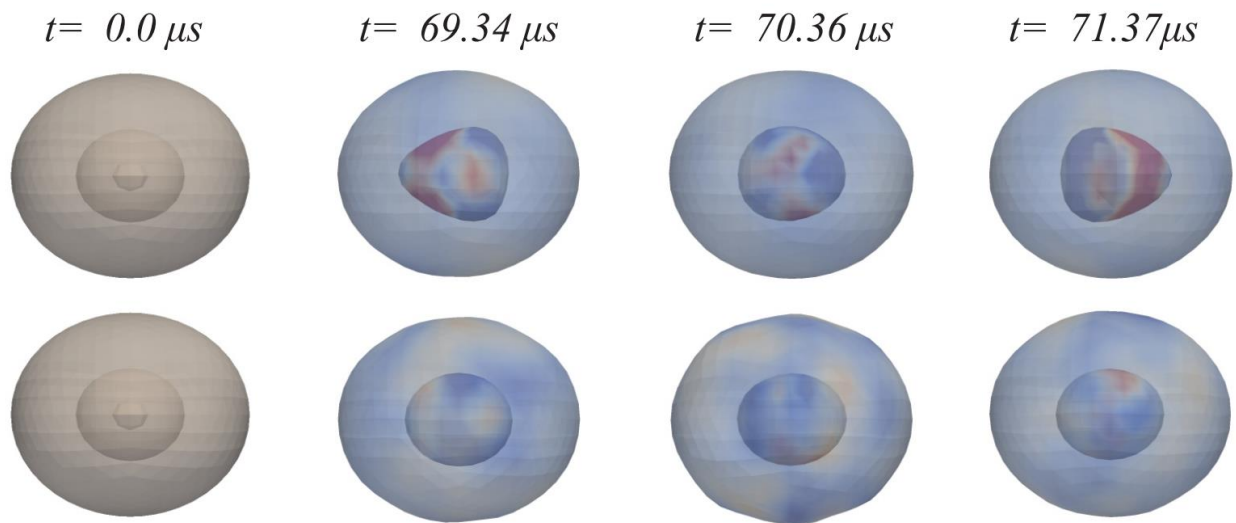


Figure 2-4 | Transient response of cancer cell and healthy simulated cell to ultrasound stimulation

The simulated transient response of the finite element model of a cancerous cell (top) and a healthy cell (bottom) at a target frequency. Note that the Probenius norm of first Piola-Kirschhoff stress tensor experienced by the cancer cell is more pronounced than that of the healthy cell. Reproduced from [74]

This computational study established the oncotripsy theory, that cells have resonant responses to ultrasound stimulation and the mechanical differences between cancerous and healthy cells may allow for an element of selectivity in ultrasound ablation by selecting a resonant frequency. This theory had two important implications for selecting the ultrasound ablation

waveform. First, the frequency dependence suggests that the signal frequency of ultrasound must be carefully selected to induce rapid oscillation growth in the cancer cell to lead to preferential lysis. Second, the duration of the ultrasound pulse must be also carefully controlled. If sufficiently long pulses were used, the oscillation in both the cancerous and healthy cells would both develop to lethal levels. As such, the computational model as described calls for both control of frequency and the ultrasound pulsing.

2.4 Modification of Low Intensity Pulsed Ultrasound Waveform for Oncotripsy Effects

The implications of this research are that oncotripsy predicts that cells have an inherent mechanical response to the pressure waves of ultrasound, independent of thermal effects or bulk tissue effects. Furthermore, cancer cells and healthy cells are predicted to have a frequency-dependent resonant response to the ultrasound stimulation. Finally, the damage that is produced by ultrasound is highly dependent on the temporal pattern with which ultrasound is applied. From this, we can intuit that to achieve the oncotripsy effect experimentally, we must stimulate our cell model with ultrasound of a pulsed single-frequency sinusoidal waveform. This waveform gives us the capability to control the temporal pattern of ultrasound stimulation while administering the single-frequency pressure waves necessary to induce oncotripsy. A pulsed sinusoidal waveform for the ultrasound signal has five degrees of freedom that completely define the waveform.

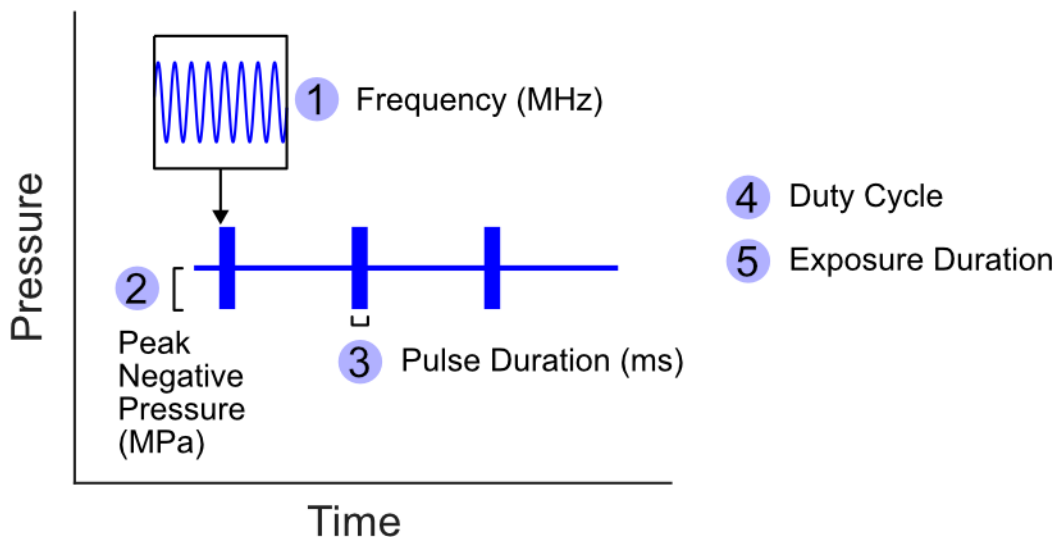


Figure 2-5 / Pulsed Sinusoidal Waveform Degrees of Freedom

Pulsed single-frequency sinusoidal waveforms have 5 degrees of freedom and allow for sufficient control of an ultrasound waveform to produce an oncotripsy effect in cells. This graphic demonstrates the change in acoustic pressure over time in this waveform. 1) Frequency – the number of acoustic pressure cycles per second throughout the pulse of ultrasound as being applied. In ultrasound, frequency is generally in units of MHz. 2) Peak Negative Pressure – the largest negative acoustic pressure, caused within one cycle of ultrasound measured. In this sinusoidal signal, the peak negative pressure is equivalent to half the peak-to-peak pressure. 3) Pulse Duration - the length in time of each ultrasound pulse train, measured in milliseconds for ultrasound. 4) Duty Cycle –the percentage of total time that the ultrasound is active. 5) Exposure Duration – defines the total time that the pulsed ultrasound signal is repeating.

In order to achieve the non-thermal ultrasound waveform required to mechanically stimulate the cells to achieve the oncotripsy effect, certain constraints must be placed on the pulsed sinusoidal waveform. To avoid heating, the ultrasound intensity must be kept below a specific

value. The term “low intensity pulsed ultrasound” specifically refers to ultrasound with a spatial-peak-temporal-average intensity (I_{SPTA}) of $<5 \text{ W/cm}^2$. This benchmark value provides some guidance into the waveform that we should select to avoid thermal effects from dominating the desired mechanical effect of oncotripsy. The I_{SPTA} can be modified by lowering the acoustic pressure OR by modifying the duty cycle, as represented in Figure 2-6.

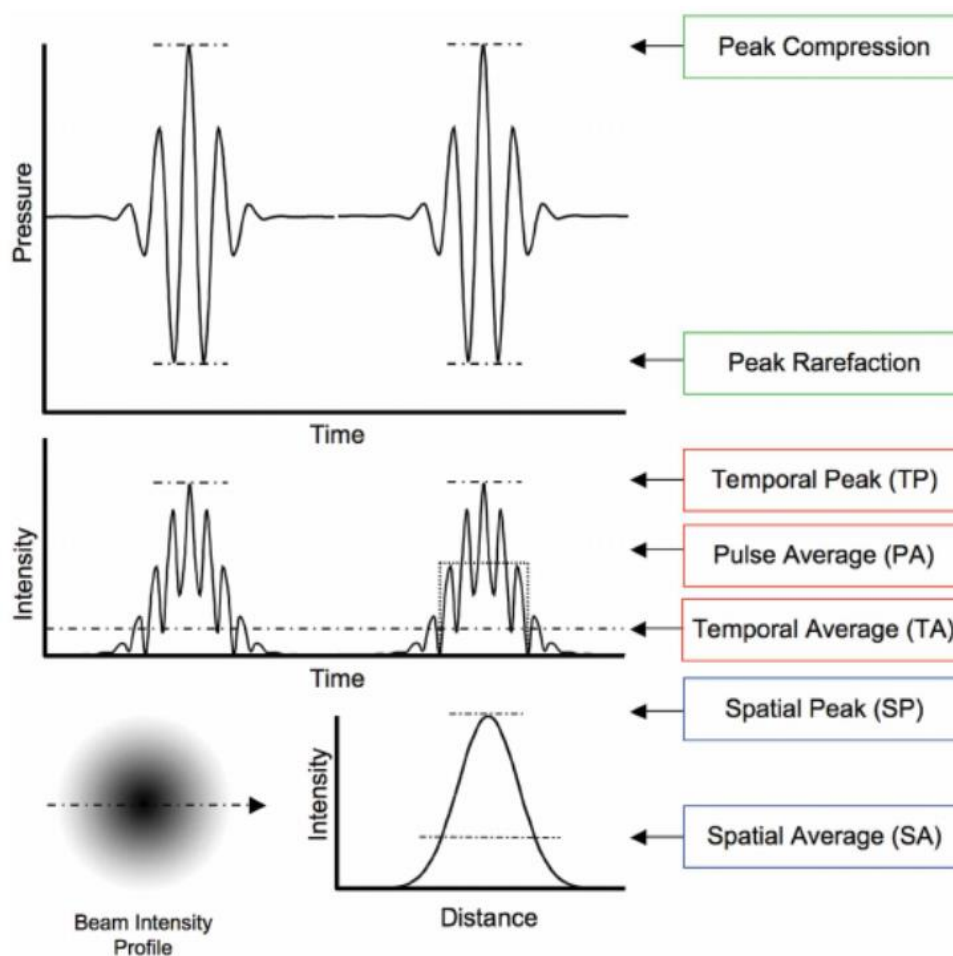


Figure 2-6 | Relationship between Acoustic Pressure and Intensity in Focused Ultrasound Beams

The acoustic intensity of focused pulsed ultrasound waves can be represented through many metrics. Throughout this dissertation, we will be referring to the spatial-peak, temporal-average

intensity (I_{SPTA}) as an important metric for representing the heating generated by ultrasound. Reproduced from [53]

I_{SPTA} can also be calculated given the following equation [24], where $p(t)$ is the acoustic pressure, Z_0 is the characteristic impedance, which in tissue can be approximated as $1.5e6 \text{ kg m}^{-2} \text{ s}^{-1}$, and PRF is the pulse repetition frequency:

$$I_{SPTA} = PRF * \int_{\text{one pulse}} \frac{p^2(t)}{Z_0} dt$$

For our pulsed single frequency sinusoidal signal, this can be simplified as follows where u_{pulsed} is a gating function that is 1 when the ultrasound is active, and 0 during the ultrasound rest period:

$$p_{\text{sinus}}(t) = u_{\text{pulsed}}(t) * PNP * \sin(k * t)$$

$$I_{SPTA} = \frac{PNP^2}{2} * \frac{DC}{Z_0}$$

As such, we can arrive at a parameter space of pressures and duty cycles that would not correspond to significant heating, assuming that the heating within one pulse is insignificant.

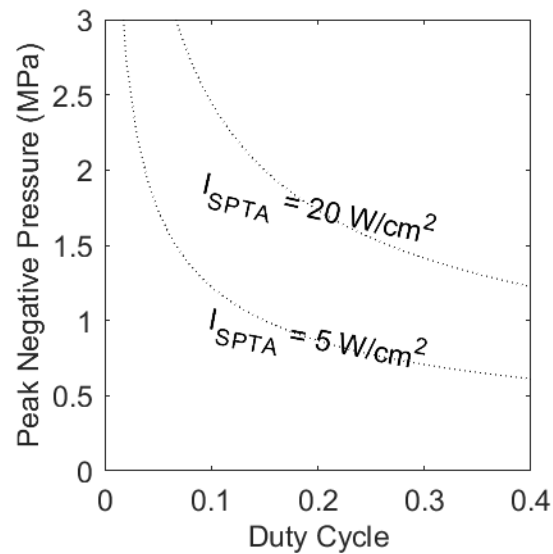


Figure 2-7 / Spatial-Peak Temporal-Average Intensity of Ultrasound

This figure demonstrates that the acoustic intensity of a pulsed ultrasound signal depends on both its duty cycle and peak negative pressure

Moreover, we aim to avoid vapor cavitation, a highly non-linear process where the peak negative pressure enables bubble nucleation and inertial cavitation, as discussed in Chapter 1. Cavitation is a result of a sustained negative pressure applied to the liquid medium, where the tension on the water promotes gas bubble formation. As such, the chance of cavitation is increased with high acoustic pressure (with resultant high peak-negative-pressure) ultrasound applied at a low signal frequency. The “mechanical index” [75] is a term used to quantify propensity to cavitation, it is calculated as:

$$MI = \frac{(\text{Peak Negative Pressure in MPa})}{\sqrt{\text{Frequency in MHz}}}$$

The lower the mechanical index, the lower the likelihood of cavitation. An FDA safety standard of $MI = 1.9$ has been set as an upper limit for diagnostic imaging without contrast agents. To avoid cavitation the pressure and frequency must be controlled for as represented in Figure 2-8.

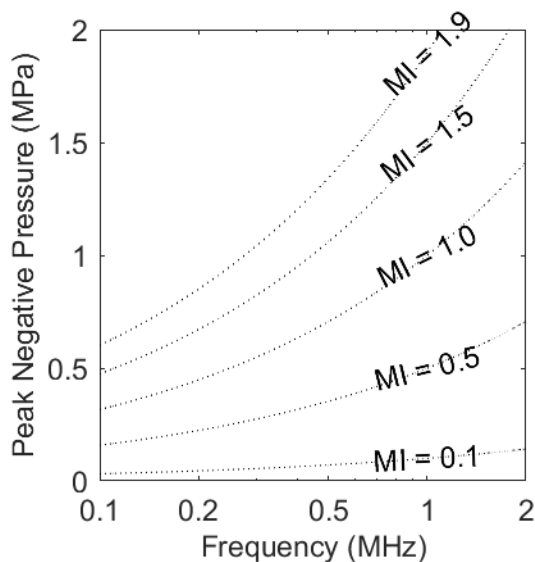


Figure 2-8 / Mechanical Index

The peak negative pressure corresponding to various mechanical indices at different frequencies of stimulation. Lower mechanical indices reduce the chance of cavitation, with an FDA safety limit for diagnostic ultrasound at $MI = 1.9$.

So by setting boundary conditions that prevent the non-linear effects of heating and cavitation from taking place, we have begun to define the parameters space that we can use to investigate the oncotripsy effect. Next we can look at the parameters suggested by the computational study. These numbers should be taken with a grain of salt as they come from a computational model with certain necessary simplifying assumptions, however, they offer a point of reference. The paper suggests that “carefully tuned ultrasound pulses in the frequency range of 80 kHz, duration in the range of 70 μ s and [spatial peak temporal peak acoustic intensity] in the

range of 0.8 W/cm^2 could induce the oncotripsy effect [74]. An I_{SPTP} of 0.8 W/cm^2 corresponds to a peak negative pressure of 0.15 MPa.

In terms of frequency, the computational theory of oncotripsy suggests a very low frequency of 80 kHz is ideal in inducing cytodisruption. There is a technical challenge in producing focused ultrasound beams with frequencies that low. This frequency can be compared to a literature review of ultrasound frequencies that have been demonstrated to show ultrasound bioeffects without heating or cavitation. A number of studies specifically referencing mechanical and non-thermal low-intensity ultrasound tend to use lower frequency ($<1 \text{ MHz}$) pulsed ultrasound. These studies reference that this form of ultrasound produces mechanical effects without hyperthermia, resulting in neurostimulation [54], chemotherapy uptake [46], and bone repair [46, 55, 56]. However, its mechanisms of action are not fully understood [57-59]. Since low frequency, low-intensity ultrasound has been documented to produce bioeffects, though the mechanism is unknown, this would seem to be an adequate parameter space to test to investigate the oncotripsy theory. If we consider technical limitations, that make it challenging to focus ultrasound generated at signal frequencies of less than 0.2 MHz, we have arrived at a window of frequencies to evaluate for the oncotripsy effect. From Figure 2-8, in order to achieve a mechanical index of <1.9 with a signal frequency of 0.2 MHz, we must keep the peak negative pressure of our acoustic signal at no more than 0.7 MPa. From Figure 2-7, in order to achieve a $I_{SPTA} < 5 \text{ W/cm}^2$ with a peak negative pressure of 0.7 MPa, we need a duty cycle of $< 25\%$. For the purposes of ensuring minimal thermal build-up throughout the experiment, and because it is a common experimental convention with pulsed ultrasound, we will select a duty cycle of 10%. Exposure duration will be selected to be 2 minutes, from experimental convention and to allow for high throughput analyses of multiple different ultrasound waveforms.

The remaining parameter that has not been addressed that is crucially important for the oncotripsy theory is the pulse duration. The oncotripsy theory suggests that cells exposed to mechanical ultrasound for sufficiently long pulse durations will ultimately be disrupted. The cancer selectivity of oncotripsy arises from the fact that, at specific target frequencies, the critical pulse duration to destroy cancer cells is significantly lower than the pulse duration to destroy

healthy cells. Using the upper bound of signal frequency from literature review of 1 MHz, a one cycle pulse would correspond to a pulse duration of 1 μ s. The computational theory suggests that pulse durations of 70 μ s could induce cytodisruption, so we can consider that parameter. On the upper bound, for the purposes of this dissertation we suggest that 100 ms pulses are an arbitrary cut-off, above which the heating within one pulse cannot be discounted. From a literature review, the pulse duration of pulsed ultrasound used for imaging generally corresponds to less than 10 cycles, or 10 μ s assuming a 1 MHz signal. Implementations of LIPUS that have incurred bioeffects tend to have pulse durations somewhere within the millisecond range. As such, we have placed limits on some of the key degrees of freedom for the ultrasound waveform, see Table 2-1. In Chapter 3, we will describe the experimental validation of oncotripsy and investigation of the effect of this waveform on an *in vitro* cell model.

	Selected Range to Investigate	Reasons
Frequency	0.2 MHz – 1 MHz	0.2 MHz – technical limitations in focusing low frequency 1 MHz – literature review of a variety of unexplained bio-effects for low intensity, low frequency ultrasound
Peak Negative Pressure	< 0.7 MPa	Necessary to maintain MI<1.9 at 0.2 MHz
Duty Cycle	0.1	Needed to be below 0.25 to maintain $I_{SPTA} < 5$ W/cm ² . Lowered to 0.1 for increased thermal safety margin
Exposure Duration	2 minutes	Experimental convention to allow for high-throughput experiments
Pulse Duration	10 μ s – 100 ms	Diagnostic ultrasound (10 μ s) and 100 ms to prevent thermal effects

Table 2-1 / Waveform Parameters Suggested for Oncotripsy Effect

Chapter 3

LIPUS CANCER-SELECTIVE ABLATION OF ONCOTRIPSY

3.1 Introduction

In this chapter, I describe the experimental investigation used to test the oncotripsy theory and further investigate the mechanism of low intensity pulsed ultrasound (LIPUS) cytodisruption in an *in vitro* suspension cell model. First, I describe an experiment where we swept various parameters of the pulsed sinusoidal ultrasound waveform and evaluated the response of target cancer cell and off-target healthy cell subpopulation. Next, I include the mechanistic analysis of the ultrasound physical processes in the observed cancer cell cytodisruption. Finally, I conclude with a proposed unified theory that connects experimental findings of this investigation of LIPUS with the protested oncotripsy theory. I was the project lead on designing and performing these experiments, and the results are published in Applied Physics Letters [76].

3.2 Experimental Support of Oncotripsy Theory

3.2.1 Approach

For the purposes of the initial investigation into the oncotripsy model, we elected to insonate cells in suspension. This is a well-established method of applying ultrasound to cells that streamlines experimental design and allows for high-throughput experiments. Moreover, suspension cells represent a simple mechanical model, with each cell relatively mechanically isolated from their surrounding cells, which would enable simpler computational modeling as we refine the computational model for oncotripsy. Several clinically relevant diseases involve cells floating in suspension, namely hematological malignancies such as leukemia [77, 78]. Metastasis, the spread of malignant cells throughout blood vessels, also involves cancer cells in suspension [79]. The clinical significance of a therapy targeted at solid tumor cells is more pressing, however, beginning with suspension cells offers a proof of concept that can be expanded upon in future work.

As described in Chapter 2, we predicted that low frequency (<1 MHz) pulsed ultrasound with an $I_{SPTA} < 5 \text{ W/cm}^2$ and a mechanical index of < 1.9 could potential incur a cancer-selective effect as predicted with the oncotripsy theory. The oncotripsy theory makes specific testable predictions that distinguish it from other potential theories for ultrasound cytodisruption. These predictions are: 1) frequency-dependence of ultrasound cytodisruption, with stronger disruption taking place a cell's resonant frequency, 2) cyto-disruption is a result of a growth in mechanical oscillations in cell membranes, as such, a minimum pulse length is required. This implies that non-monotonically frequency dependent and pulse-duration dependent cytodisruption that also had distinct effects on healthy and cancer cells would be supportive evidence of the oncotripsy theory. To perform these tests, we needed to isolate the effect of modifying frequency and pulse duration during the ultrasound trials.

3.2.1 Results

To test the hypothesis that LIPUS can selectively ablate cancer cells, we applied LIPUS to suspensions of human K562 and U937 cancer lines and primary T cells isolated from human peripheral blood mononuclear cells (PBMC), chosen as representative malignant and healthy cell types. Cell suspensions were placed in acoustically transparent-bottomed 24-well plates and insonated with a focused ultrasound transducer positioned in a water bath below (**Figure 3-1a**). First, we performed a pressure sweep to determine the pressure of ultrasound that corresponded to a cytodisruptive effect. We used pulsed ultrasound (10% duty cycle) with peak negative pressure (PNP) <1.2 MPa that corresponded to an $I_{SPTA} < 5 \text{ W/cm}^2$. We confirmed that 60 seconds LIPUS at 0.67 MHz, 20ms pulse duration (PD) induced significant and irreversible cytodisruption of K562 cells at $PNP > 0.6 \text{ MPa}$, as measured with ethidium homodimer-1 (Ethd-1) uptake (**Figure 3-1b**). Heating was always <1°C (**Figure 3-7**). For further experiments, we selected 0.7 MPa PNP, which induced moderate cytodisruption. This pressure corresponds with a $1.63 \text{ W/cm}^2 I_{SPTA}$ and $16.3 \text{ W/cm}^2 I_{SPTP}$ at the 10% duty cycle. At the lowest frequency tested in this study, 0.3 MHz, this corresponds to a mechanical index of 1.3, which is beneath the FDA safety limit of 1.9 [53]. The lack of heating and the low mechanical index suggests that the ultrasound applied remains within the realm of LIPUS.

To test different pulsing patterns, PD and pulse repetition frequency were varied simultaneously to maintain a constant duty cycle (**Fig 1c**). This resulted in the application of the same total acoustic energy by each ultrasound waveform, allowing comparisons across frequencies and pulse durations. We swept PD from 2-40ms with each of the 0.3, 0.5, and 0.67 MHz transducers (**Figure 3-1d**). We observed that cytodisruption was highly dependent on frequency, PD, and cell type. 20ms PD and 0.5 MHz maximized the selectivity with near complete cytodisruption for K562 and U937 and >80% survival for T cells (**Figure 3-1e**). We found that cytodisruption increases with longer PD, despite the same total energy applied. Next, we assessed a broader panel of cell types at 0.5 MHz, using cancer cells in co-culture with PBMC (**Table 3-1**). The cancer cell models showed significantly more cytodisruption than subpopulations within PBMC at >10ms PD. (**Figure 3-1f**). RBCs exhibited virtually no disruption, as measured by hemoglobin leakage, under any condition.

4T1	Mouse Cell Line	Mammary Gland, Epithelial (human breast cancer)
CT26		Colon, Fibroblast (Carcinoma)
MCF7	Human Cell Line	Mammary Gland, Epithelial (adenocarcinoma)
SK-BR-3		
MDA-MB-231		
CD4	Human Primary Cells, Peripheral Blood Cells	CD3+, CD4+
CD8		CD3+, CD8+
B		CD3-, CD19+
NK		CD3-, CD19-, CD56+
RBC	Bovine Primary Cells	Peripheral Blood Cells

Table 3-1 / Cell Models Tested

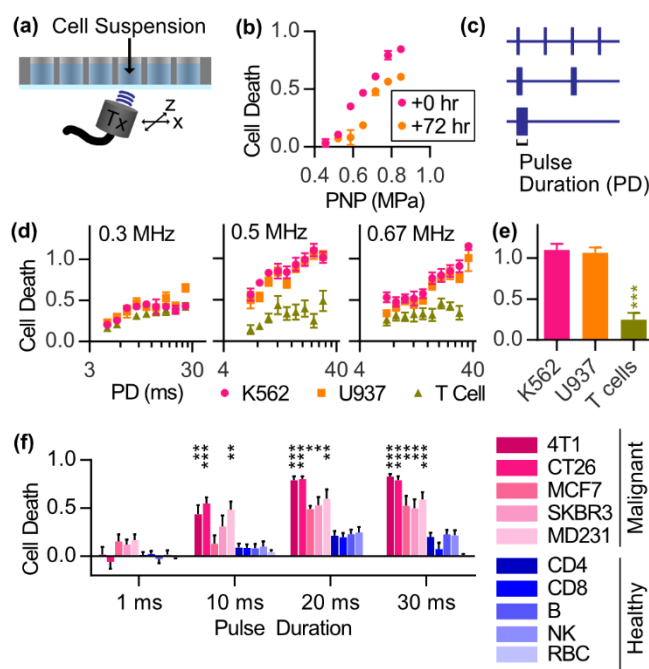


Figure 3-1 | Screening reveals ultrasound parameters that induce cancer-cell selective cytodisruption.

a, Schematic of mylar-bottom 24-well plate over water bath containing focused ultrasound transducer. **b**, K562 cell death (N=3, error bars SEM) in response to 0.67 MHz, 20ms PD, 10% duty cycle, 60 seconds, LIPUS at various peak negative pressures (PNP). 0.7 MPa PNP selected for future experiments. **c**, Diagram depicting constant energy while sweeping PD. **d**, 0.3 (N=4), 0.5 (N=9), 0.67 (N=9) MHz LIPUS induces frequency-, PD-, and cell-dependent cytodisruption. **e**, 0.5 MHz, 20ms PD LIPUS induces significantly less cell death (N=9, $p < 0.001$) on T cells compared to either K562 or U937. **f**, 0.5 MHz LIPUS induced cancer-selective cell death (N=9) in mixed sample of healthy PBMC and cancer models (**Table 3-1**), measured through cytometry. RBC death assessed using hemoglobin release. Significance indicated as largest p-value from 2-tailed t-test between each cancer and each healthy cell model. (* $p < 0.05$, ** $p < 0.01$, *** $p < 0.001$).

3.2.1 Discussion

The observed cytodisruption from LIPUS was frequency dependent, pulse-duration dependent, and cancer-cell selective, as predicted by the oncotripsy theory. In the *in vitro* model, LIPUS applied at 0.5 MHz with a 20ms PD had the largest therapeutic margin in disrupting a diverse panel of cancer cells while leaving healthy blood and immune cells largely intact. Cytodisruption at 0.3 MHz was largely ineffective on either cell, while at 0.67 MHz the cancer cells were only moderately disrupted. Our results demonstrate that specific parameters of low intensity pulsed ultrasound (LIPUS) can induce cancer cell-selective cytodisruption. While the acoustic intensity of the ultrasound is similar to that of diagnostic ultrasound, we found that cytodisruption only occurred with pulse durations (PD) of greater than 10 ms, while diagnostic ultrasound uses PD of about 10 μ s [53]. Simply modifying the ultrasound parameters within the previously outlined limits of mechanical ultrasound allowed for cancer-cell selective cytodisruption.

3.3 Cellular Biomolecular and Structural Responses to LIPUS

3.3.1 Approach

As we had observed experimental evidence that fit several of the testable predictions of oncotripsy, we then endeavored to understand the effects of the ultrasound stimulation on the cellular level. The oncotripsy theory predicts that cellular elements undergo deformation in response to ultrasound due to a build-up of resonant oscillation. When the oscillation reaches a certain threshold, the theory suggests that cell death occurs. In order to investigate this, we performed a biochemical assay of a cancer cell model and its response to LIPUS to investigate the bio-chemical mechanisms of cell death. We followed this up with high speed videos to attempt to gain insight on the biomechanics involved at the cellular level.

3.3.2 LIPUS cytodisruption associated with cytoskeletal damage and activation of apoptotic, immunogenic cell death pathways

To characterize LIPUS cytodisruption's biomolecular mechanisms, we evaluated CT-26 cells 2 days after 2-minute treatment with 0.5 MHz, 0.7 MPa LIPUS with flow cytometry. At >10ms PD, increased cell death and apoptosis was observed (**Figure 3-2a**). Also, cells expressing calreticulin, a pro-phagocytic signal [80], increased while proliferative marker Bcl-2 [81] decreased (**Figure 3-2b**). The activation of apoptotic and phagocytic pathways may enhance LIPUS' effectiveness as an anti-cancer therapy by promoting anti-tumor immune response. To evaluate LIPUS' effect on the cytoskeleton, we performed confocal microscopy on CT-26 immediately after LIPUS. The actin cytoskeleton, stained with phalloidin, is qualitatively and quantitatively disrupted after insonation with 30ms PD LIPUS. This agrees with literature that states that LIPUS disrupts the cellular cytoskeleton [82, 83]. We demonstrate at 1ms PD LIPUS, the cytoskeleton appears unchanged from the negative control (**Figure 3-2c**).

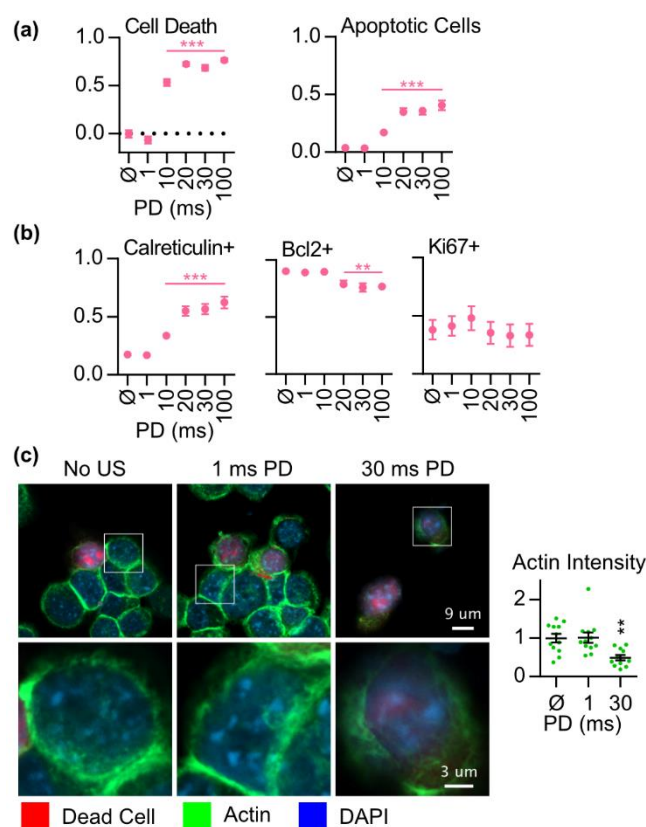


Figure 3-2 / Ultrasound cytodisruption associated with apoptotic and pro-phagocytic pathways.

a, CT-26 cells assessed 2 days after LIPUS (0.5 MHz, 0.7 MPa 20ms PD, 10% DC, 2 min). Fraction of surviving cells and apoptotic cells assessed using flow cytometry Ethd-1 vs Annexin V graphs (**Fig Sup 2**). X-axis from no ultrasound (\emptyset) to 1-100ms PD. Significantly increased cell death and apoptosis with >10ms PD LIPUS (N=12, error bars SEM). **b**, Increase in pro-phagocytic marker calreticulin (N=12) and decreased survival marker Bcl2 (N=8) but no change in proliferation marker Ki67 (N=8) with >20ms PD US. **b**, Confocal microscopy of CT-26 cells immediately after LIPUS. 30 ms PD LIPUS disrupted actin ring and significantly decreased actin stain intensity (N=12). (** $p < 0.01$, *** $p < 0.001$).

3.3.3 LIPUS results in translational motion of cells

To visualize LIPUS' effect on target cells, we imaged K562 cells in suspension under transmitted 2 W laser illumination using an ultra-high speed camera. Laser light was only applied during image acquisition to prevent heating of the cells. Cells were floating between two acoustically transparent films near an acoustic reflector generating standing waves. We recorded video at 5 Mfps starting 100ms after the beginning of insonation. We observed cells translating several microns along the axis of insonation at the ultrasound frequency, but not undergoing large-scale deformation (**Figure 3-3**). This suggests that either that LIPUS' effect on cell shape are on the nanoscale and thus not detectable in this imaging paradigm or involve deformation or displacement of sub-cellular organelles relative to the cytoplasm.

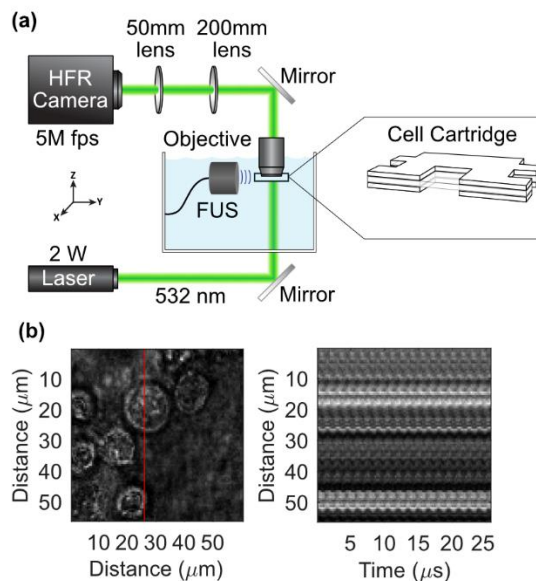


Figure 3-3 / *High-speed video demonstrates no large-scale cell deformation during ultrasound insonation.*

a, Schematic of high frame rate camera setup enabling cellular imaging at 5 Mfps. **b**, 1d trace over time demonstrates translation of cell of ~ 1 micron after 100ms of 0.67 MHz ultrasound exposure.

3.3.4 Discussion

This analysis suggests that the LIPUS parameters that induce cytodisruption do so through a variety of cellular mechanisms including direct cytodisruption, cytoskeletal damage, and the activation of apoptotic pathways. There is also evidence that pro-phagocytic pathways are activated, which are important for the clinical and combined therapy applications of the technology and worthy of further study. The high-speed camera footage provided insight into the mechanical forces that are applied onto the cells. Though this analysis is limited by the resolving power of the optics used in this experiment, it does provide an upper bound on the cellular deformations that are involved in the response to LIPUS. The high speed camera video analysis shows cell translation, but no detectable (micron-scale) deformation. Future experiments with enhanced resolving power or contrast agents that could provide clearer tracking of sub-cellular components could prove very useful in quantifying the cellular deformation in response to ultrasound.

3.4 Ultrasound Mechanisms Involved in LIPUS Bioeffects

3.4.1 Approach

This experimental data serves as the first investigation of the applicability of the oncotripsy theory. As such, we wished to evaluate other potential explanations for the frequency-, pulse-duration-, and cell-type- dependency for our LIPUS induced cytodisruption. To accomplish this, and to gain further insight into the acoustic mechanisms for the ultrasound response that we observe, we investigate the role that acoustic standing waves, cavitation, and the acoustic medium play in transducing LIPUS into cellular effects.

3.4.2 Standing waves are necessary for LIPUS cytodisruption

Literature suggests that acoustic standing waves affect the mechanical forces experienced by cells [84, 85]. Such waves can result from interference of an incident ultrasound wave with its reflection, forming a spatially static pattern of pressure nodes and anti-nodes. The pressure profile

in acoustic 24-well plates revealed a standing wave pattern near the water-air interface. To examine whether this plays a role in cytodisruption, we constructed an acoustically transparent cuvette, where standing waves could be optionally introduced using a reflector (**Figure 3-4a**). We found that cells insonated in the absence of standing waves (0.67 MHz, 100ms PD) did not show significant cytodisruption, while cells treated in the presence of a reflector reproduced the cytodisruption observed in the 24-well plate (**Figure 3-4b**). Doubling the PNP in the reflector-free configuration to match the maximal pressure at standing wave anti-nodes did not induce significant cytodisruption. This suggests that standing waves are mechanistically required for LIPUS cytodisruption.

Among other effects, acoustic pressure spatial gradients in standing waves give rise to acoustic radiation force that pushes cells toward pressure nodes [86]. We tracked the motion of fluorescently labeled K562 cells in response to continuous LIPUS in an imaging chamber and observed that 0.5 MHz ultrasound in a standing wave configuration propelled cells toward the nodes (**Figure 3-4c**). A 100ms PD was not sufficient for cells to aggregate at nodes, which happened after ~1 second under continuous ultrasound.

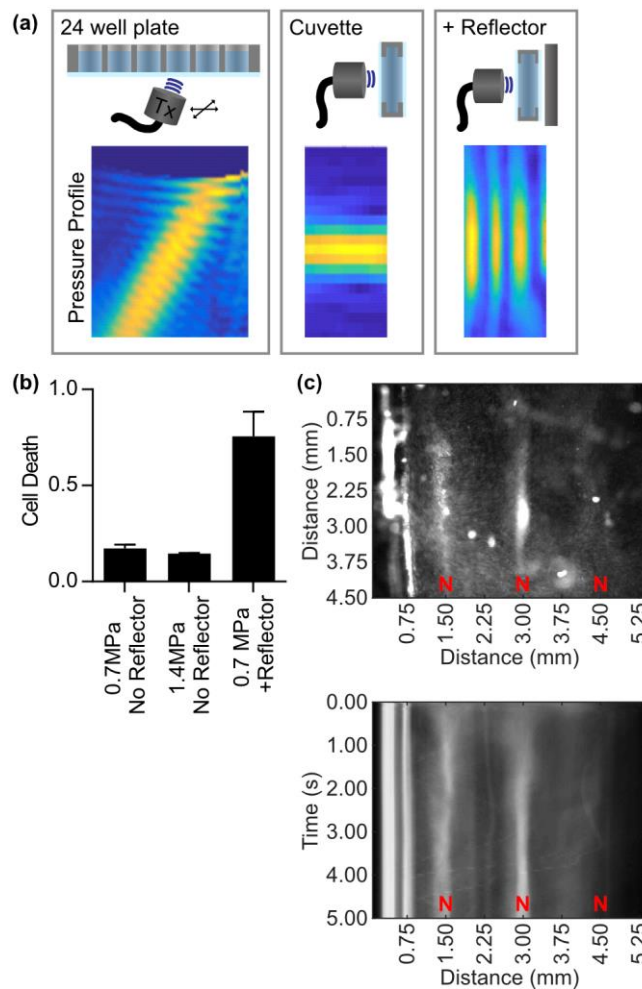


Figure 3-4 / Standing waves required for LIPUS cytotoxic effect.

a, Schematics of experimental setups with pressure field measurements. Standing waves present in 24-well plate, but not in acoustic cuvette unless a metal reflector is introduced. **b**, 0.67 MHz, 100ms PD, 0.7 MPa LIPUS does not induce cell death in acoustic cuvette without reflector, even when doubling the pressure. However, when the reflector is added, cell death occurs as observed previously. **c**, Fluorescence microscopy demonstrates that cells accelerate toward nodes (N) in response to continuous 0.5 MHz, 0.7 MPa US. Upper image is still frame after 5 seconds of ultrasound, lower image represents average of y dimension (perpendicular to ultrasound) versus time. Cells achieve aggregation within 1 second.

3.4.3 Cell mediated cavitation is required for LIPUS cytodisruption

Cavitation is a known mechanism for local amplification of acoustic pressure and cell killing [87]. To examine its role in LIPUS cytodisruption, we measured the acoustic emissions of cells treated with LIPUS in the acoustic cuvette using single-element passive cavitation detector orthogonally co-focused with the LIPUS transducer (**Figure 3-5a**). We measured the signature of inertial cavitation (emissions with broad spectral content) and stable cavitation (harmonics of the transmitted frequency). As controls, we confirmed that no cavitation was measurable in degassed PBS cell buffer, while stable and inertial cavitation were detected from commercial Definity microbubbles, which were suspended in the degassed PBS for consistency (**Figure 3-5b**).

K562 cells generated both stable and inertial cavitation when exposed to 0.5 MHz, 100ms PD LIPUS in the presence of a reflector. The cavitation magnitude increased during the LIPUS pulse with an inflection point around 20ms (**Figure 3-5b**), a timescale similar to the PD needed for cytodisruption. No cavitation was seen without a reflector. Laser illumination of the cuvette revealed bubble formation in a standing wave pattern in response to long-PD ultrasound in the presence of the reflector (**Figure 3-5d**).

The conditions resulting in LIPUS-induced cavitation in K562 cell suspensions correlate with those causing cytodisruption, with both requiring standing-waves and PD >20ms (**Figure 3-5c**). However, cavitation is not sufficient for cytodisruption, since PBMC, which are not strongly disrupted by tested LIPUS conditions, nevertheless produced similar amounts of cavitation (**Figure 3-5c**).

To determine which components of cell suspensions could be responsible for cavitation, we measured acoustic signal from LIPUS-exposed solutions of cell-sized 10 μm polystyrene beads and liposomes. These liposomes were formed in the lab in degassed conditions to prevent gas core formation, and degassed again prior to experiment. No cavitation was detected from the beads.

However, degassed liposomes did produce cavitation, suggesting that cell's lipid contents may have a role in promoting cavitation (**Figure 3-5c**).

Finally, to confirm that cavitation is necessary for cytodisruption, we suppressed cavitation by placing the cell solution within an acoustically transparent pressure-chamber comprising a plastic pipette bulb and applying hydrostatic pressure by connecting the sealed chamber to a compressed air source pressurized to 400 kPa above ambient atmospheric pressure (**Figure 3-5e**). Elevating the hydrostatic pressure within the bulb created an environment where cavitation was suppressed by decreasing the absolute magnitude of the peak negative pressure induced by ultrasound insonation [88-90]. With the bulb pressurized to 400 kPa above ambient pressure, there was an almost complete reduction of cytodisruption of K562 cells in the chamber by 100ms PD LIPUS. This confirms that cavitation is mechanistically necessary.

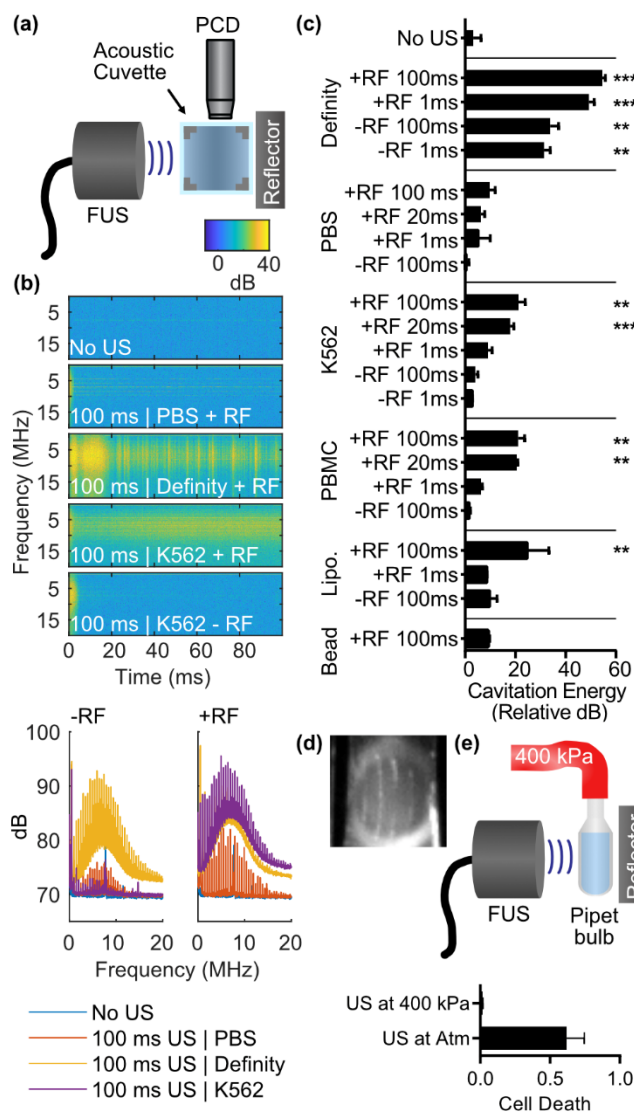


Figure 3-5 / Cell-mediated cavitation is mechanically necessary for cytodisruption.

a, Schematic of passive cavitation detection setup using 10 MHz transducer orthogonally positioned to FUS transducer. **b**) Spectrogram of scattered signal from 100ms pulse of 0.5 MHz ultrasound transducer. Broadband signal of cavitation demonstrated with Definity positive control. No cavitation in PBS, however cavitation present in K562 suspensions only with reflector. **c**) Cavitation energy ($\int P^2 dt$) partially correlates with cytodisruption. Significant cavitation (compared to “No US”, ** $p < 0.01$, *** $p < 0.001$) observed with Definity, with K562 / PBMC with reflector (RF) and >20ms PD, and with liposomes with RF and 100ms PD. Note: PBMC cells

induce cavitation, though they are resistant to LIPUS cyto-disruption. **d**, 100ms PD LIPUS with reflector induces cavitation bubbles formed in standing wave pattern in K562 sample. **e**, Schematic of pipet bulb pressurized to 400 kPa to form pressure chamber. At over-pressure, which suppresses cavitation, LIPUS cytodisruption is suppressed.

3.4.4 LIPUS cytodisruption attenuated in solid media

To investigate whether LIPUS cytodisruption occurs in cells embedded in solid media, we suspended K562 cells in agarose and acrylamide gels. We placed these gels in our acoustic cuvette with the reflector to generate standing waves (**Figure 3-6a**) and exposed them to ultrasound. Cell death in the LIPUS treated gels was assessed using Ethd-1 fluorescence and compared to untreated control gels (**Figure 3-6b**). While statistically significant cytodisruption in agarose gels was observed, it was greatly attenuated compared to liquid suspensions (**Figure 3-6c**). This suggests that either the mechanical rigidity or the translational motion restriction imposed by a solid extracellular medium inhibits LIPUS cell killing.

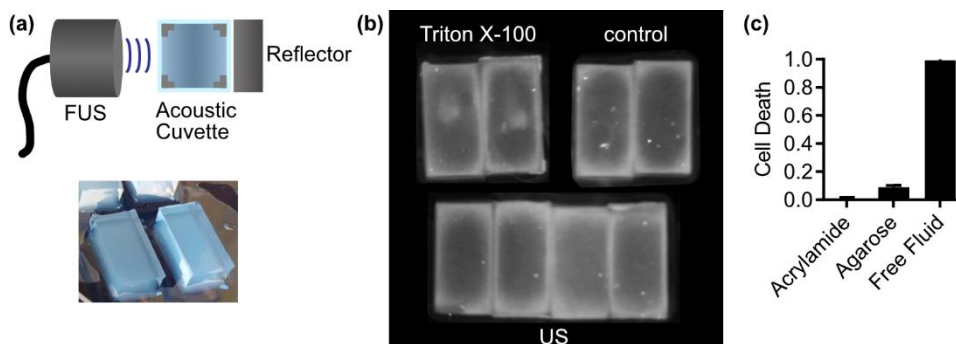


Figure 3-6 / Cells suspended in gel medium undergo attenuated cytodisruption in response to our targeted LIPUS parameters.

a, Schematic diagram and picture demonstrating 1 cm thick 1% agarose gels containing K562 cells and their placement between the 0.5 MHz transducer and the metal reflector. **b**, Cytodisruption was assessed using ethidium homodimer assessed in gel reader, positive control had injection of Triton X-100 in center of gel. **c**, Cell death is completely attenuated in acrylamide gels compared to free fluid condition. Cell death is attenuated, but still significant in agarose gels. Observed using ethidium homodimer-1 fluorescence after ultrasound at 0.5 MHz, PD 100 ms.

3.4.5 Discussion

These experiments revealed that the formation of standing waves and the emergence of cavitation were necessary to disrupt cancer cells. However, the presence of cavitation, which was seeded by cells and enhanced by standing wave ARF, was not sufficient to guarantee the disruption of any particular cell type. This is consistent with our finding that the most significant cytodisruption took place at 0.5–0.67 MHz and not 0.3 MHz, despite an expected increase in cavitation at lower frequency. This suggests that while cavitation may locally amplify the pressure supplied LIPUS, a given cell type’s response to the resulting mechanical stress depends on its biophysical properties. This is consistent with the “oncotripsy” theory developed by Ortiz et al [74, 91], which suggests that cells respond to ultrasound at different resonant frequencies and with

different fatigue behavior based on their distinct mechanical properties [92, 93]. Additional studies are needed to probe the biophysical underpinnings of this response.

3.5 Conclusion

Cancer-selective cytodisruption by LIPUS could fulfill the clinical need for safe non-invasive tumor ablation, complementing positional or molecular targeting approaches. Based on our results in suspension cell models, LIPUS applied within blood vessels could target blood cancer or circulating tumor cells [94]. The needed standing waves could be generated by engineering the acoustic field of one or more array sources or leveraging endogenous reflective surfaces such as bones. In addition, the acoustic field may need to be sufficiently large to enable appropriate continuous exposure of cells during flow. In addition, our data indicating that LIPUS-disrupted cells show markers of apoptotic and immunogenic cell death (ICD) suggest that disruption of cancer cells in circulation could stimulate immune responses against solid tumors elsewhere and strengthen the effect of conventional chemotherapeutic regimens [95-103]. Additional work is needed to extend this technology into the solid tumor context. While in our experiments cells in hydrogel phantoms responded weakly to LIPUS, this biochemical and mechanical context may not accurately represent the solid tumor milieu. In addition, even partial killing of solid tumor cells could be effective if it can precipitate an abscopal immune effect. Future cell monolayer, 3D culture, and finally *in vivo* studies are needed to test these hypotheses.

Emerging protocols for cancer therapy are increasingly using synergistic therapy involving chemotherapeutics, immunotherapy, and surgery. Novel immunotherapy drugs that assist in the formation of a systemic anti-neoplastic immune response, such as anti-PD1 or TLR9 agents are showing promise in tumor remission and prevention of recurrence [104]. Ultrasound oncotripsy has a strong synergistic potential in its capability to selectively increase the membrane permeability of target cells. This can allow for increased uptake of a chemotherapeutic or release tumor-specific antigen to induce a systemic anti-cancer immune response.

In summary, ultrasound oncotripsy could have significant clinical benefits, particularly in clinically challenging tumors, where enforcement of therapeutic margins is difficult [70].

Combining local surgical resection with regional ultrasound oncotripsy that selectively targets cancer cells distributed throughout healthy tissue and enhances systemic chemotherapy and immunotherapy could not only remove the bulk tumor, but help address micro-metastasis that lead to tumor recurrence.

3.6 Methods

3.6.1 High Throughput Ultrasound Experiments

We developed a high through-put experimental system that allowed for Acoustically transparent 2.5 μm mylar film (Chemplex #100) was placed on the bottom of 24-well no-bottom plates (Greiner Bio-One #662000-06) that have been painted with a thin film of Sylgard 184 PDMS (Fisher Scientific # NC9285739) and heat treated at 60 °C for 24 hours. The resulting 24 well plates are watertight and have acoustically transparent bottoms. The plates were sterilized and loaded with cell samples as required for ultrasound exposure.

24 well plates were placed on a metal stage such that the mylar film was in contact with a water bath. One of the three available FUS transducers (0.3 MHz: Benthowave BII-7651/300, 0.5 MHz: Benthowave BII-7651/500, and 0.67 MHz: Precision Acoustics PA717) was attached to a metal arm angled 20 degrees from the normal of the water bath. A Velmex X-Slide motorized positioning system allowed the 3d motion of the arm allowing the transducers to be targeted at each well individually. The transducers were aligned using a Precision Acoustics fiber optic hydrophone to target the bottom center of well A1 on the 24 well plate. A MATLAB script controlled a signal generator (B&K #4054B) which generated a unique RF signal for each well of the plate and the Velmex positioning system. This signal was then amplified (AR #100A250B) and sent to drive the FUS transducers. The water bath was filled with distilled water that was degassed by a water conditioning system (ONDA #AQUAS-10) and heated to 37 degrees Celsius prior to experiments.

Fiber optic thermometry was used to measure the effect of insonation at the highest frequency 0.67 MHz and highest pressure 1.2 MPa PNP tested to confirm that no heating would

occur in LIPUS experiments. Fiber was placed at ultrasound focus within acoustically transparent 24 well plate and temperature measurements were made for 1 ms and 100 ms pulse duration insonations. (**Figure 3-7**)

For the parameter search experiments (**Figure 3-1d**) K562, U-937, or T cells were spun down and carefully resuspended in vacuum degassed PBS containing 2 μ M ethidium homodimer-1 (Ethd-1) at 2 million cells in 2 mL PBS in each well of an acoustic 24 well plate. On each plate, 2 wells were loaded with 0.1% Triton X-100 as a positive control (pos) and 2 wells were uninsonated as a negative control (neg). Immediately after insonation, cell death for each well was estimated as Ethd-1 signal (s) as measured through plate reader as: $\text{cell death} = (S_{\text{well}} - S_{\text{neg}}) / (S_{\text{pos}} - S_{\text{neg}})$.

For the broad cell panel experiments (**Figure 3-1e**), 2×10^6 4T1, CT26, MCF7, SK-BR-3 or MDA-MB-231 cancer cells were mixed with 2×10^6 PBMCs in 2 mL degassed PBS respectively and loaded into each well of an acoustic 24 well plate. After insonation, 2×10^4 cells are cultured on 96 well plates for 2 days, and resuspended in PBS with 2 μ M Ethd-1 prior to analysis with flow cytometry. For immune cell surface marker analysis, single-cell suspensions were stained with antibodies in PBS containing 2% fetal bovine serum. Antibodies to CD3(UCHT1), CD4(SK3), CD8(RPA-T8), CD19(SJ25-C1), CD33(P67.6) and CD56(5.1H11) were used to gate the CD4 T cells, CD8 T cells, B cells, myeloid cells and NK cells respectively. Myeloid cells, which are largely undifferentiated cells with similar mechanical properties as cancer cells and comprise <1% of the PBMC cells, were excluded from analysis. Cell death for each subpopulation was determined from the count of cells that did not uptake Ethd-1 in comparison to untreated control.

Heparinized bovine red blood cells (Sierra for Medical Science), were diluted to 10% hematocrit in degassed PBS, then insonated as described above. After ultrasound, RBCs were centrifuged so that samples of supernatant could be assessed for hemoglobin release (Abcam ab234046). RBC death in response to LIPUS calculated as hemoglobin release compared to positive control 0.1% Triton X-100 and negative control of no ultrasound. (**Figure 3-1e**)

3.6.2 Analysis of biomolecular pathways of cytodisruption

For CT26 cell apoptosis and proliferation marker analysis, 2 days after ultrasound treatment, CT26 cells were stained with anti-Calreticulin (Abcam) 30 min at room temperature. Annexin V binding buffer (Biolegend) was used for Annexin V staining. Fixation and permeabilization was performed with BD Cytotfix/Cytoperm buffers (BD Biosciences) for Ki-67 and Bcl-2 intracellular antibodies staining. **(Figure 3-2a)** Cell death was determined from the count of cells that did not uptake Ethd-1 in comparison to untreated control. The percentage of apoptotic cells reported is the fraction of Annexin V positive and Ethd-1 negative cells measured through flow cytometry. Cell signaling pathway markers Bcl-2 and Ki-67 were the fraction of Bcl-2 or Ki-67 stain positive and Aqua (fixable dead cell stain) negative cells. The pro-phagocytic marker calreticulin percentage reported was the fraction of calreticulin stain positive in all cells, live or dead. Flow cytometry gates are shown in **Figure 3-8**.

For confocal experiments, CT-26 cells were allowed to settle on PDL-coated 1.5 μm coverslips for 1 hour. Slides were treated with fixable LIVE/DEAD stain (ThermoFisher #L34971), fixed in 4% paraformaldehyde and stained with phalloidin (Cayman #20549). Coverslips are then mounted with mountant containing DAPI (ThermoFisher #P36971). Four color confocal images were acquired with a 100x oil immersion objective at the Caltech Beckman Imaging Facility. **(Figure 3-2b)** To quantify, the actin signal intensity was measured on 12 cells imaged in each ultrasound treatment condition.

3.6.3 Investigation of standing waves and acoustic radiation force in cytodisruption

Pressure measurements performed using the fiber optic hydrophone positioned using the Velmex X-Slide. Color scale pressure maps represent peak negative pressure at each position within well or acoustic cuvette. Acoustic cuvettes were 1 cm x 1 cm 3d printed chambers with walls made of mylar film fixed with super glue. The cuvette was mounted to the bottom of the water tank and surrounded by distilled, degassed water. The center of cuvettes were aligned with the FUS transducer focus using fiber optic hydrophone and Velmex positioning system. A 3"x3"x0.5" rectangular prism block of aluminum was used as an acoustic reflector and positioned

directly opposite from the transducer next to the cuvette (**Figure 3-4a**). K562 were loaded into the acoustic cuvette at 1 M cells / mL containing 0.2 μ M Ethd-1. A 3d printed imaging chamber submerged in a water bath positioned the 0.5 MHz transducer a fixed position from an acoustic reflector, such that fluorescent imaging of a compartment containing GFP-labeled K562 at the focal point of the transducer could be achieved. Imaging was obtained through a 4x air objective (Olympus) (**Figure 3-4c**).

3.6.4 Role of cavitation in cytodisruption

Using the same setup for standing wave experiments, a 10 MHz single element transducer (Olympus #U8421024) was positioned orthogonally to the FUS transducer, also aligned using the fiber optic hydrophone (**Figure 3-5a**). The signal from the single element transducer was captured directly by an oscilloscope (Keysight InfiniiVision 3000 X-series) without pre-amplification. 4M data points were acquired during the signal transmission period of LIPUS. Frequency spectral analysis was then performed to generate logarithmic spectral graphs of frequency intensity at various representative time points during the pulse (**Figure 3-5b**) and quantification of total signal energy (**Figure 3-5c**). Samples were loaded into the acoustic cuvette. Vacuum degassed PBS used as negative control. 10 μ L of freshly resuspended Definity microbubbles (Lantheus Medical Imaging, Inc.) in degassed PBS used as positive control. Aluminum reflector used as described above to introduce standing waves. K562 or PBMC cells loaded at 1 M cells / mL in degassed PBS. Liposomes were generated from 14.0-18.0 PC Avanti Polar lipid suspended in chloroform which was lyophilized to remove chloroform, rehydrated using degassed 300 mOsm sucrose solution, sonicated for 10 minutes, heated at 40°C for 10 minutes, then degassed. Liposomes solution resuspended in degassed PBS to approximate lipid concentration in cell samples. 10 μ M polystyrene beads at 1 M beads / mL also measured. Cavitation energy assessed in relative units by integrating the square of the pressure signal over time (**Figure 3-5c**). Image of cavitation bubbles taken using camera facing the single element transducer, with plane of laser illumination generated from laser light source and 1D diverging lens positioned above the acoustic cuvette (**Figure 3-5d**). A pressure chamber was constructed by attaching a compressed air line with a gauge pressure of 400 kPa onto an acoustically transparent plastic pipet bulb. Acoustic

transmission through the pipet bulb was confirmed using hydrophone measurements. 1 M/mL K-562 cells loaded in degassed PBS containing 2 μ M Ethd-1 into the pipet bulb. Cavitation from in samples loaded into the pipet bulb in place of the acoustic cuvette could be measured as described above. Cell death assessed using Ethd-1 signal (**Figure 3-5e**).

3.6.5 Solid model investigation

Agarose gels were prepared by mixing 2% agarose in vacuum-degassed PBS at 65 °C with 2 M/mL K562 cells in PBS, adding 2 μ M Ethd-1, and poured into 1 cm x 1 cm x 2.5 cm molds. Acrylamide gels were prepared as in this reference [105] with a final concentration of 1 M/mL K562 and 2 μ M Ethd-1. Gels were insonated in the acoustic cuvette as described above. Cell death was calculated as magnitude of Ethd-1 signal observed at LIPUS focus on gel reader in comparison to signal from gels injected with 0.1% Triton X-100 and gels not treated with LIPUS.

3.6.6 High speed camera visualization of cell deformation

We assembled a high-speed microscopy setup capable of directly visualizing the effect of ultrasound on K562 cells. Our setup used a 2 W 532-nm laser (CNI, MLL-F532-2W) controlled by an optical beam shutter (Thorlabs SH05, KSC101). Right angle prism mirrors directed the laser light through a water bath and into a sample chamber containing the imaged samples. K562 cells were loaded into a custom-made acrylic cartridge containing an inner pocket surrounded by mylar film. A 3d printed holder positioned the cartridge such that the inner pocket was at the focus of the 0.5 MHz transducer. The cells were freely floating between two acoustically transparent films near an acoustic reflector that generate standing waves. A 100x water immersion Plan Fluor objective (Olympus) was used to image the target cells. A series of prism mirrors and converging lenses with focal lengths of 200 mm and 50 mm delivered the image into a Shimadzu HPV-X2 camera, which acquired 256 images over 51.2 μ s, at a sampling rate of 5 million frames per second. To account for acoustic propagation through water, the camera was externally triggered to begin acquisition 100 ms after the start of the ultrasound pulse. A single pulse of 100 ms at 0.5 MHz and 0.7 MPa PNP was used to insonate the sample in these experiments.

3.7 Supplemental Figures

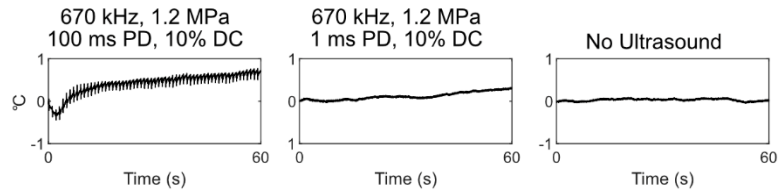


Figure 3-7 / No temperature change induced by LIPUS.

Assessed temperature change using fiber optic hydrophone system at focus of FUS transducer in 24-well plate configuration. LIPUS applied at 0.67 MHz, 1.2 MPa PNP, with 10% duty cycle did not induce any appreciable change (<1 °C) in temperature even with 100 ms pulse duration.

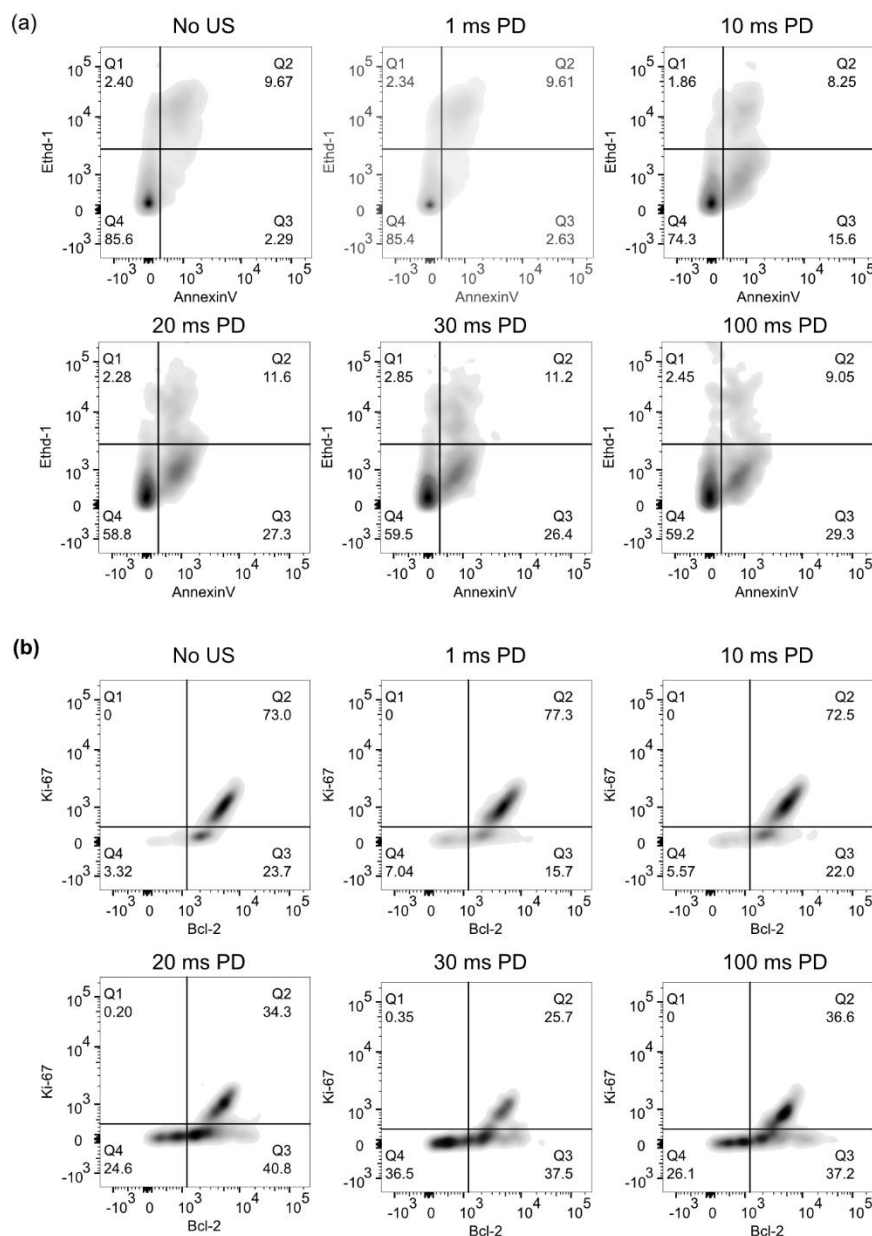


Figure 3-8 / Flow cytometry gates used for phagocytic, apoptotic analysis

a, Ethidium homodimer (Ethd-1) vs Annexin V stain generates the following quadrants. Q4: live cells, Q3: live cells undergoing apoptosis, Q2-Q1: dead cells. **b**, Ki-67 vs Bcl-2 stains used to identify Bcl2⁺ and Ki-67⁺ populations.

Chapter 4

REFINEMENT OF ONCOTRIPSY THEORY, FUTURE DIRECTIONS

4.1 Introduction

In this chapter, I will discuss the refinements made to the oncotripsy theory in light of the experimental evidence attained as described in Chapter 3. The new computational model, focusing on accumulating cytoskeletal damage and cyclic fatigue, as developed by Erika Figueroa with my experimental input, is summarized and its implications for future work in oncotripsy are discussed. Finally, this chapter concludes with a description of future directions for the oncotripsy project in combined therapy and solid tumor treatments as are being investigated by Dr. Peter Lee's group in City of Hope.

4.2 Inconsistencies between Transient Response Oncotripsy Model and Experimental Data

The experimental data did indeed show frequency-dependent and cell-type specific cytodisruption in response to low intensity pulsed ultrasound (LIPUS). However, there were some inconsistencies in the predictions from the theoretical model and our experimental results.

Firstly, the experimental data suggested that the mechanical transduction of the acoustic energy into the cell is more complex than was originally conceived in the original oncotripsy theory. Experimental evidence suggested that standing wave conditions and cell-mediated cavitation were required for oncotripsy to take effect. This suggests that there are additional mechanisms at play beyond simply the cell's response to the acoustic pressure waves. However, the frequency-dependency of the ultrasound stimulation does suggest that the oncotripsy mechanism of an inherent mechanical response of the cells is still an important part of the pathway of LIPUS cytodisruption. Though this merits further studies, we have developed a hypothesis to reconcile our experimental findings. We hypothesize that standing waves serve to enhance lipid-

cavitation [106] through cellular aggregation [107] and that the harmonic cavitation acts as a local amplifier of the ultrasound signal to induce local cell oscillation at the target frequency. The final chapter of this work includes a more detailed investigation into this theory. The cell then can respond to the acoustic signal as is amplified by the stable cavitation. This hypothesis is supported by the observations that cavitation alone is not sufficient for cytodisruption, as the healthy cells exhibited the same cavitation energy as cancer cell suspensions upon insonation, but did not have as strong of a response to ultrasound as the cancer cells. The unique predictions of the oncotripsy theory of frequency-dependence, pulse-duration-dependence, and cell-type specificity were still observed despite the dependent mechanistic role of cavitation and standing waves.

Some inconsistencies likely came from the difficulty of obtaining the precise mechanical properties to describe the viscous and elastic properties of cells. The transient response model by Heyden was defined using a literature review that cross-referenced multiple measurements of the elastic properties of hepatocellular carcinoma cells and compared them with healthy liver hepatocytes. A sensitivity analysis was also performed including measurements from other cancer and health cell models that suggested broader applicability among other cells, which is the reason that we performed experiments with a different panel of cells during our experimental validation. However, mechanical properties that describe an objects response to stress are highly dependent on the frequency at which the oscillating stress field is being applied [108]. The measuring techniques used generally assessed the cellular response to a static stress, or a dynamic stress oscillating in the sub-kHz range, as higher shear rates are challenging to assess [66, 67]. Unfortunately, it would likely be a massive undertaking to correctly ascertain the appropriate mechanical parameters from independent measurements in order to develop an accurate model from first principles. Furthermore, this would not account for the role of cavitation, which may act as a local amplifier of ultrasound in a way that is challenging to model. What is possible, however, is to fit the necessary parameters of the computational model in such a way that it recapitulates experimental data. Then such a model can be used to extrapolate the cellular response to ultrasound waveforms that were not tested experimentally, offering a guide-post for future experimentation and model validation.

We believe that the inconsistencies in the ideal frequency and pressure required to achieve an oncotripsy effect are likely due to the errors in the input parameters and could be corrected by fitting these parameters of the model with experimental data. However, one error that is difficult to account for is the inconsistency with the pulse duration required for cytodisruption. While the theory predicts that pulse durations of approximately 100 μs should be sufficient for cytodisruption, our experiments suggested that pulse durations of greater than 10 ms were required for significant cell death. With 1 MHz ultrasound, 10 ms corresponds to 10,000 cycles of ultrasound. It is very unlikely that at 10,000 cycles, the cell is still experiencing a transient response to ultrasound. In fact, the oncotripsy computational model suggests that the cell's oscillation has achieved a steady-state condition by that point of ultrasound stimulation. The transient response oncotripsy model, which suggests that cytodisruption occurs when the growth rate in cell oscillation occurs faster with cancer cells than healthy cells at target resonant frequencies that leads to cancer-selective cytodisruption, thus requires adjustment.

4.3 Reduced Cytoskeleton Constitutional Model (Figueroa)

Erica Figueroa, also at Ortiz lab, refined the oncotripsy theory to consolidate the predictions from the theory with the experimental results. This section references heavily from her pre-publication on arXiv regarding this discussion [109]. This model idealizes the cytoskeleton as a random 3D network consisting of interconnected actin filaments and microtubules spanning a rigid and heavy organelles and a rigid oscillating cell membrane. The essential novelty of the model will be the accounting of the competition between damage to the filaments under plausible failure scenarios, such as a critical elongation or force, and healing of the same filaments after the passages of a certain lag time. Such a competition is a classic example of a 'birth-death' process in evolutionary dynamics [110]. The experimental observation that LIPUS with a pulse duration of 10 ms is required for cytodisruption suggests that a potential model for the cellular response to ultrasound is one of cyclic fatigue. Rather than modeling the cells as a structure that fails as soon as deformation increases past a certain threshold, this new model considers the cell as a tensegrity structure, with cytoskeletal elements that can accumulate damage in response to stress. The computational tensegrity model consists of a random three-dimensional

network of filaments and tubules spanning a rigid and heavy nucleus and a rigid oscillating cell membrane. Critically stressed filaments (in red) are targeted for failure and removed from the network (damage), possibly to be reinstated after some lag time (healing).

The system incorporates a damage variable that represents the proportion of tensegrity elements aligned along a certain direction being broken, and thus no longer contributing to maintaining cytoskeletal stiffness. Kinetic coefficients define a “birth” and “death” process of the cytoskeletal state that enables modeling of the tensegrity structure that evolves over time in response to ultrasound stimulation. The material parameters used in this simulation were taken from literature review, as in the Heyden model, but were also tested and fitted against experimental data. This allowed for the development of a refined finite element model that could describe how damage could accumulate with pulsed ultrasound stimulation.

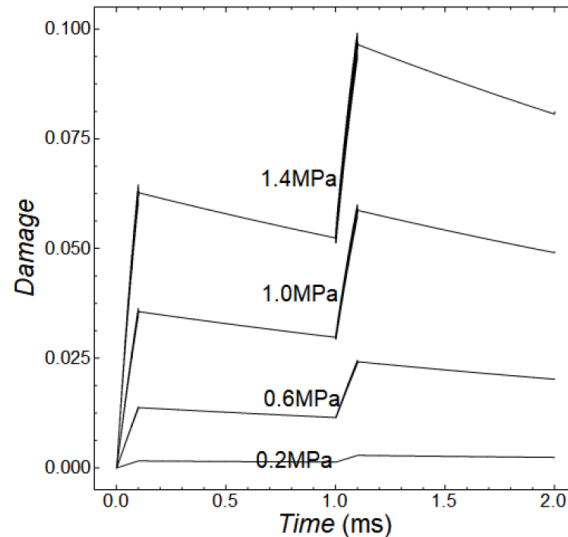


Figure 4-1 / Evolution of Cytoskeletal Element Damage during Ultrasound Stimulation

Mean of the damage of a cancerous cell predicted through finite element tensegrity model in response to ultrasound stimulation with pulse duration of 0.1 ms. Damage accumulates during insonation, and then decreases gradually during the healing process. Reproduced from [109]

This model was computationally intensive, so a simplified one-dimensional model with isotropic simplifications was developed to allow for longer time-domain simulations. The reduced model generated consistent predictions as the full finite element model. However, it had the benefit that it reduced the cell's response to ultrasound as purely a function of the interaction between a pulsed ultrasound signal and four abstract cell parameters:

- ω_0 – natural frequency of vibration
- ζ – damping ratio
- t_r – relaxation time for healing
- q_c – critical damage prior to cell death

This model allows sufficiently long simulations to investigate the role of varying pulse durations on cell models. Figure 4-2 demonstrates the strength of the cytoskeletal damage model in differentiating the effect of infrequent long pulses versus frequent short pulses. The model demonstrates that long pulses allow the accumulated damage in the cytoskeleton to reach higher peaks and accumulate to higher values than repeated shorter pulses. The presence of periods of healing between the pulses, even short periods, prevent the cell damage from achieving its maximum potential. When cell damage reaches a critical damage point q_c the cell is considered to have died in this reduced model.

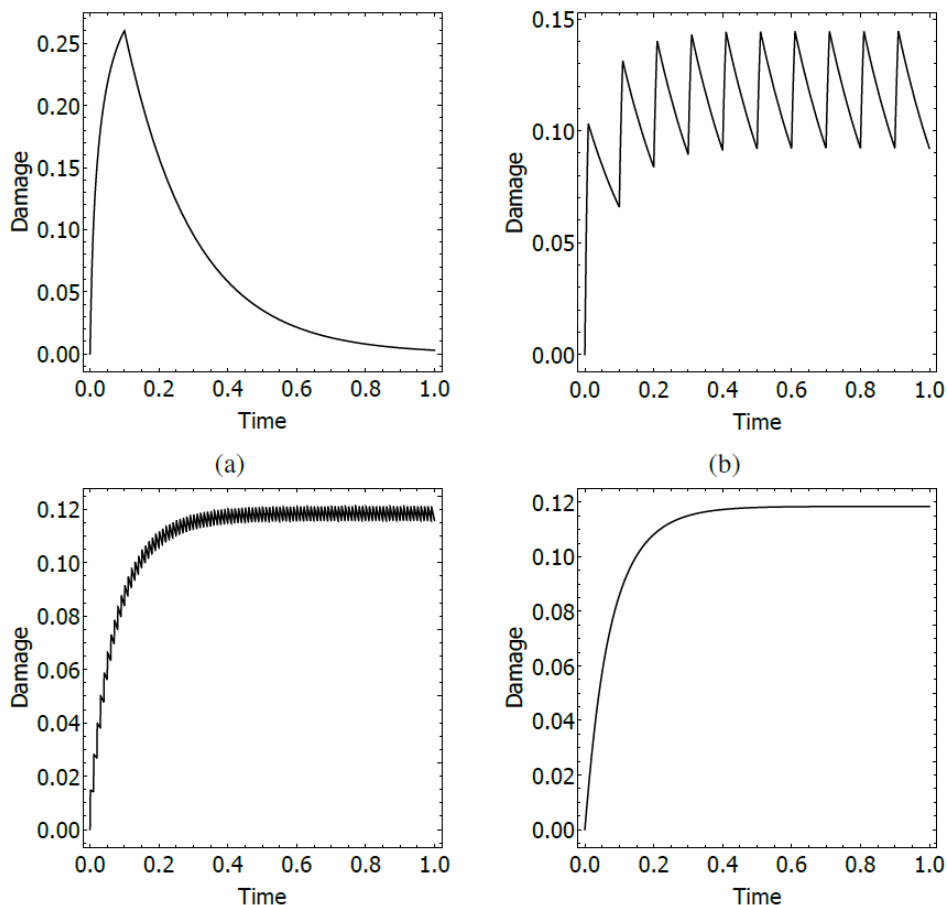


Figure 4-2 / Cytoskeletal damage evolution with reduced dynamical oncotripsy model

Mean of the damage of a cancerous cell predicted through reduced oncotripsy model in response to ultrasound stimulation with varying pulse durations. a) 100 ms PD, b) 10 ms PD, c) 1 ms PD, d) limit with infinitesimal pulse duration. Higher levels of cytoskeletal damage are achieved with long pulses. Reproduced from [109]

This reduced model allows for simulations of populations of cells with varying mechanical properties as represented by the variables above being sampled from normal distributions around specified population means. These simulations allow for the recapitulation of the sigmoidal curves of the observed increased cytodisruption with increasing pulse duration, and other experimentally

measured values. This allows for curve fitting from experimental data to enhance the extrapolative potential of the model. The natural frequency of vibration and damping ratio can be determined for a cell population by performing a frequency sweep using a high-bandwidth ultrasound transducer. The experiments described in the previous chapter of this work were performed using three low-bandwidth transducers, and as such only allowed an assessment of three frequencies. Subsequent work using multiple transducers capable of sweeping frequencies could solve for the natural frequency and damping ratio of the reduced model of oncotripsy. The relaxation time and critical damage could be calculated using the pulse duration curves as a metric of how cell damage varies based on the temporal distribution of the ultrasound stimulation. A system of cytoskeletal damage and healing in response to mechanical stresses preserve the frequency-dependence of the original system and offers a mechanistic explanation for the pulse-duration dependence of the oncotripsy effect. A full description of this model is beyond the scope of this dissertation; however, its implications provide valuable insight into how cells may respond differently to prolonged pulses of ultrasound versus repeated short pulses of ultrasound on a mechanical level. In her thesis, Erika Figueroa describes how the reduced oncotripsy model, when fit with data from experiments similar to those that I performed and described in the previous chapter, could be used to determine the ideal insonation parameters to achieve selectivity in cytodisruption of cancer cells without harming healthy cells.

4.4 Conclusions

These refinements to the computational model suggest that oncotripsy theory could serve as a valid mechanism for the experimental evidence of frequency and pulse duration-dependent cytodisruption. Further research into the oncotripsy theory should explore the testable predictions from the cytoskeletal cyclic fatigue model with newly posed experiments that both investigate the mechanism of cytodisruption as well as the effect of additional ultrasound waveforms on wider variety of cells *in vitro* and in suspension. An exploration of potential experiments that could provide further insight into the oncotripsy mechanism and into its applicability in clinically relevant contexts is included in Chapter 6 of this thesis.

Chapter 5

ALTERNATIVE WAVEFORMS FOR CELLULAR MODIFICATION / CONTROL

5.1 Introduction

In this chapter, I will describe some of the other work that I have had the opportunity to be a part of during my time at Caltech working on research in ultrasound therapeutics. These are included in my dissertation as a demonstration of how ultrasound's bioeffects are widely varied and dependent upon the ultrasound parameters used. First, I describe work that I did with Avinoam Bar-Zion to investigate the cavitation of gas vesicles in response to short pulses of high amplitude ultrasound. Then I describe a work that I did with Mohammad Abedi regarding using high intensity focused ultrasound to activate thermally controlled circuits *in vivo*.

5.2 Modification of Pulsed Ultrasound Parameters

The bulk of my thesis work has involved using low intensity pulsed ultrasound (LIPUS) to induce selective ablation in cancer cell models through a novel mechanism described as "oncotripsy" which involves a frequency-dependent mechanical response of the cell to ultrasound stimulation. However, there are many other parameters spaces that are used to achieve different bio-effects. A waveform optimized to induce cavitation will use much lower frequencies and higher pressures than LIPUS. Pulse durations may be extremely short, as the inertial cavitation event occurs only after a few cycles of insonation. In this chapter, I include a discussion of the cavitation waveform used in the gas vesicle cavitation project as a demonstration of this waveform. Conversely, a waveform optimized induce thermal effects, would high frequency, high pressure, and continuous wave, in order to maximize the power that is attenuated into tissue. In this chapter,

I include a discussion of the ultrasound waveform used in the thermal control project as a demonstration of this.

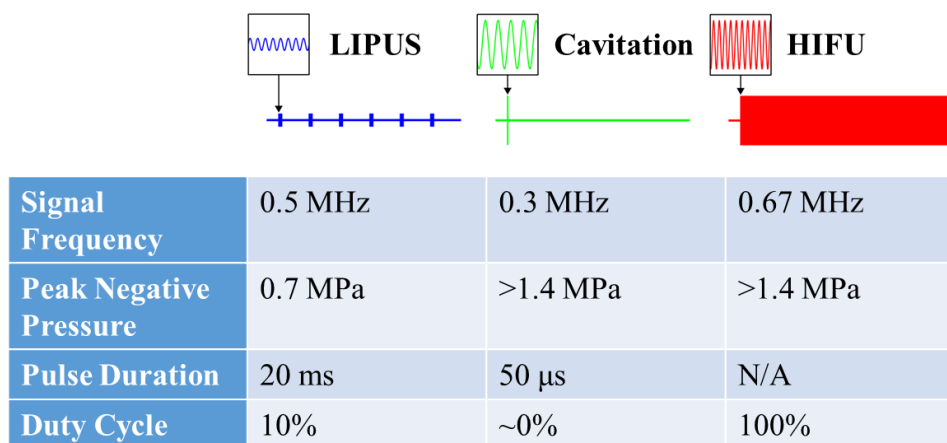


Figure 5-1/ Ultrasound Waveforms for Different Bioeffects

Three waveforms discussed in this dissertation: Low intensity pulsed ultrasound (LIPUS) uses medium frequency, low-pressure ultrasound that is pulsed with a 20 ms pulse duration to achieve bio-effects such as oncotripsy. Cavitation ultrasound uses low frequency, high pressure, short bursts of ultrasound to promote the cavitation of gas-filled cavitation nuclei. High intensity focused ultrasound (HIFU) uses high frequency, high intensity continuous wave ultrasound to maximize thermal deposition in tissue.

Ultrasound cavitation uses high pressure, short pulses to induce a contrast agent to undergo a destructive inertial cavitation event. The most common contrast agent used in lab and clinically is a lipid-stabilized microbubble. This microbubble contains a small volume of gas that maintains its cohesion due to its lipid shell. At high acoustic pressures, the bubbles undergo inertial cavitation as described in Chapter 1. The key ultrasound parameter to achieve cavitation is having

a sufficiently large peak-negative-pressure that can exert a tensile force on the contrast agent to initiate the inertial cavitation

Thermal ultrasound uses high intensity, continuous wave ultrasound, generally focused to a small area in the body, to deposit acoustic energy as heat through attenuation. It can be used as an ablative therapy such as when HIFU is applied a cancer ablation technique. However, thermal ultrasound has also been evaluated as a non-ablative therapeutic modality. Local increases in temperature have an anti-inflammatory and pain relieving effect that is being studied. The body inherently has many biochemical processes that are sensitive to changes in temperature. The key ultrasound parameter to achieve temperature increase is having a sufficiently large I_{SPTA} (spatial peak, temporal average intensity). That is, an acoustic intensity that pumps a consistent amount of thermal power into the body to overcome the natural diffusion and convection in tissue to cause a local temperature increase.

5.2 Ultrasound to Detonate Acoustically Active Biomolecules

5.2.1 Background

In work pioneered and published by lead-author Avinoam Bar-Zion, we investigate the potential for the genetically-encodable biomolecules to serve as cavitation nuclei. This approach uses gas vesicles (GVs), a unique class of genetically encoded gas-filled protein nanostructures that were recently introduced as reporter genes for ultrasound [111] and magnetic resonance imaging (MRI) [112]. I had the opportunity to participate in this research project where we hypothesized that at lower ultrasound frequencies these biomolecules can also serve as nuclei for the formation and cavitation of bubbles, allowing them to serve as therapeutic warheads. My role in this project was to use ultrafast microscopy to visualize the cavitation that is induced when high-pressure ultrasound is incident upon GV's.

GVs are cylindrical amphiphilic protein shells with diameters ranging from 45 to 250 nm and lengths of 100 to 600 nm [113]. These shells are permeable to gas but exclude water due to their hydrophobic interior surface (Fig 1a). In nature, photosynthetic bacteria and archaea produce

intracellular GV's as a mechanism for regulating buoyancy in response to environmental nutrient concentration or sunlight [114]. Purified GV's produce image contrast under high-frequency diagnostic ultrasound, based on the special physical properties of their gas-filled interior [115].

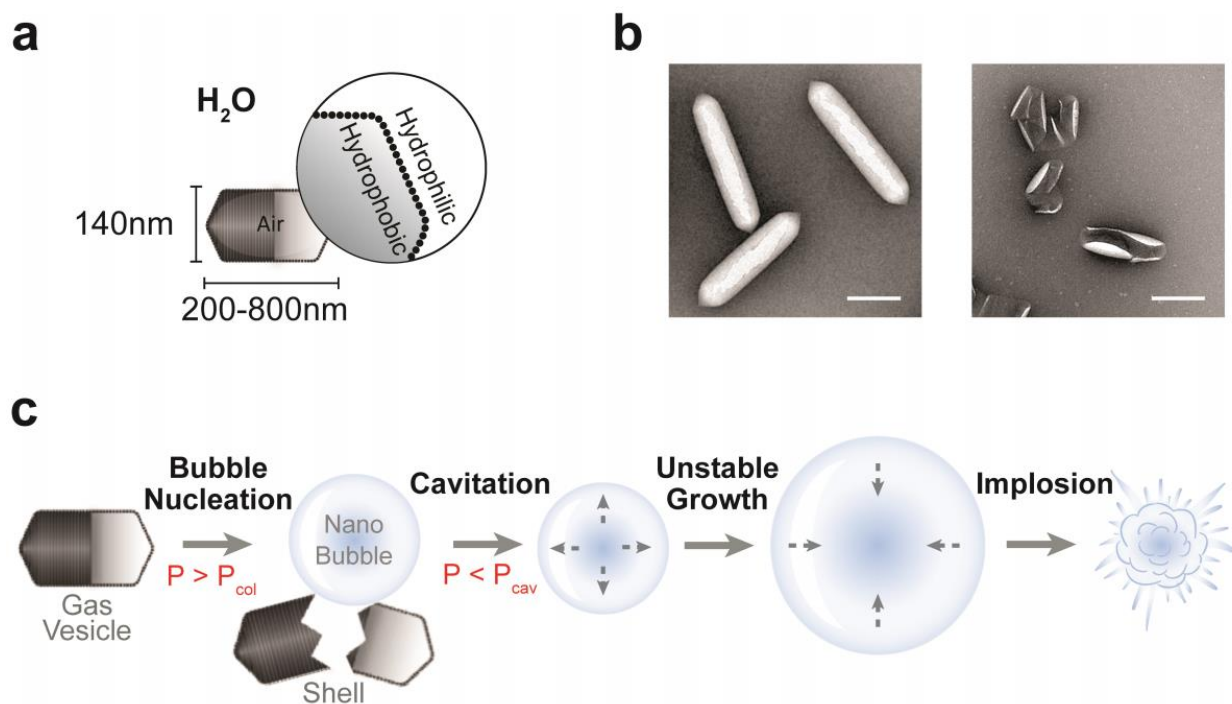


Figure 5-2 / Gas vesicles as nuclei for inertial cavitation

a, Schematic drawing of a GV. The GV's amphiphilic protein shell encloses a stable, gas-filled structure. **b**, Representative transmission electron microscopy (TEM) images of intact (left) and collapsed (right) *Anabaena flos-aquae* GV's. **c**, Proposed mechanism of GV-seeded cavitation. An ultrasound (US) pulse with a positive pressure higher than the critical collapse pressure, P_{col} , collapses the GV, resulting in the release of a nanoscale air bubble. The released nanobubble undergoes cavitation if the peak negative pressure of the US pulse reaches below the critical cavitation pressure, P_{cav} . Over several cycles, the nanobubble is converted into a micron-scale bubble, which can eventually undergo violent inertial cavitation. Scale bar represents 200 nm.

The hypothesis that GVs can nucleate bubbles for inertial cavitation arises from the fact that GVs collapse under applied acoustic pressure (Figure 5-2b), releasing the air contained inside them to the surrounding media. The ability of such collapse to take place at specific pressure thresholds, defined by GVs' DNA sequence and protein composition, has been used for background-subtracted molecular imaging [111]. Under most conditions, gas molecules released from collapsed GVs are expected to form nanoscale bubbles, which should dissolve within milliseconds due to Laplace pressure [116]. However, we hypothesized that at ultrasound frequencies in the sub-MHz range, these free bubbles could also serve as seeds for cavitation, a process in which bubbles expand and contract during the negative and positive phases of sound waves, respectively, and can grow in size through rectified gas diffusion and coalescence [117, 118]. Such processes are favored at lower ultrasound frequencies and higher peak negative pressures. In addition, bubbles can be stabilized by the presence of hydrophobic surfaces [118], such as the exposed interior of collapsed GV shells (Figure 5-2b). We envisioned that positive pressure above GVs' critical collapse threshold would break open the GVs to release gas nanobubbles, and that negative pressure would then cause these bubbles to grow. At relatively low ultrasound amplitudes, the resulting bubbles would undergo stable cavitation – a sustained periodic oscillation of gas bubble size. At relatively high amplitudes, the bubbles would undergo rapid growth and violent collapse in a process known as inertial cavitation, unleashing powerful mechanical effects²⁶ (Figure 5-2c).

5.2.2 High Speed Camera Experiments

To more directly visualize the process by which GVs nucleate the formation of cavitating bubbles, we imaged this process optically using an ultra-high frame rate camera, acquiring images at 5 million frames per second (Figure 5-3a). The GVs were attached to acoustically transparent Mylar bottomed dishes using biotin and streptavidin. Before insonation, we observed a dark pattern indicative of intact GVs (Figure 5-3b), whose gas interiors scatter visible light [114, 119]. After ultrasound was applied and reached sufficient amplitude, this dark pattern suddenly disappeared, revealing GV collapse (1.4 – 1.8 μ s, Figure 5-3b and Supplementary Fig. 3). 2.4 μ s later, we observed dark bubbles forming and cavitating inside the field of view (Figure 5-3b), and

continuing to grow in the following cycles (Figure 5-3d). Meanwhile, control dishes with biotin coating alone failed to show significant cavitation (Figure 5-3c). We further analyzed the videos to track the temporal relationship between GV collapse and bubble cavitation. After forming, bubbles grew and shrank at the frequency of the ultrasound waves (Figure 5-3d). By comparing the phase of the wave at which GVs disappear with the phase of maximal bubble growth rate, we could confirm that GVs collapse at the positive pressure peak, while maximal growth of the resulting bubbles occurs at the negative peak of the ultrasound cycle, π apart in phase (Figure 5-3e), and bubble size peaks at $3/2 \pi$, at the conclusion of rarefaction (Figure 5-3f). Similar results were seen across bubbles (Figure 5-3g). This data confirms the ability of GVs to nucleate bubble cavitation and supports the mechanistic model depicted in in Fig. 1c.

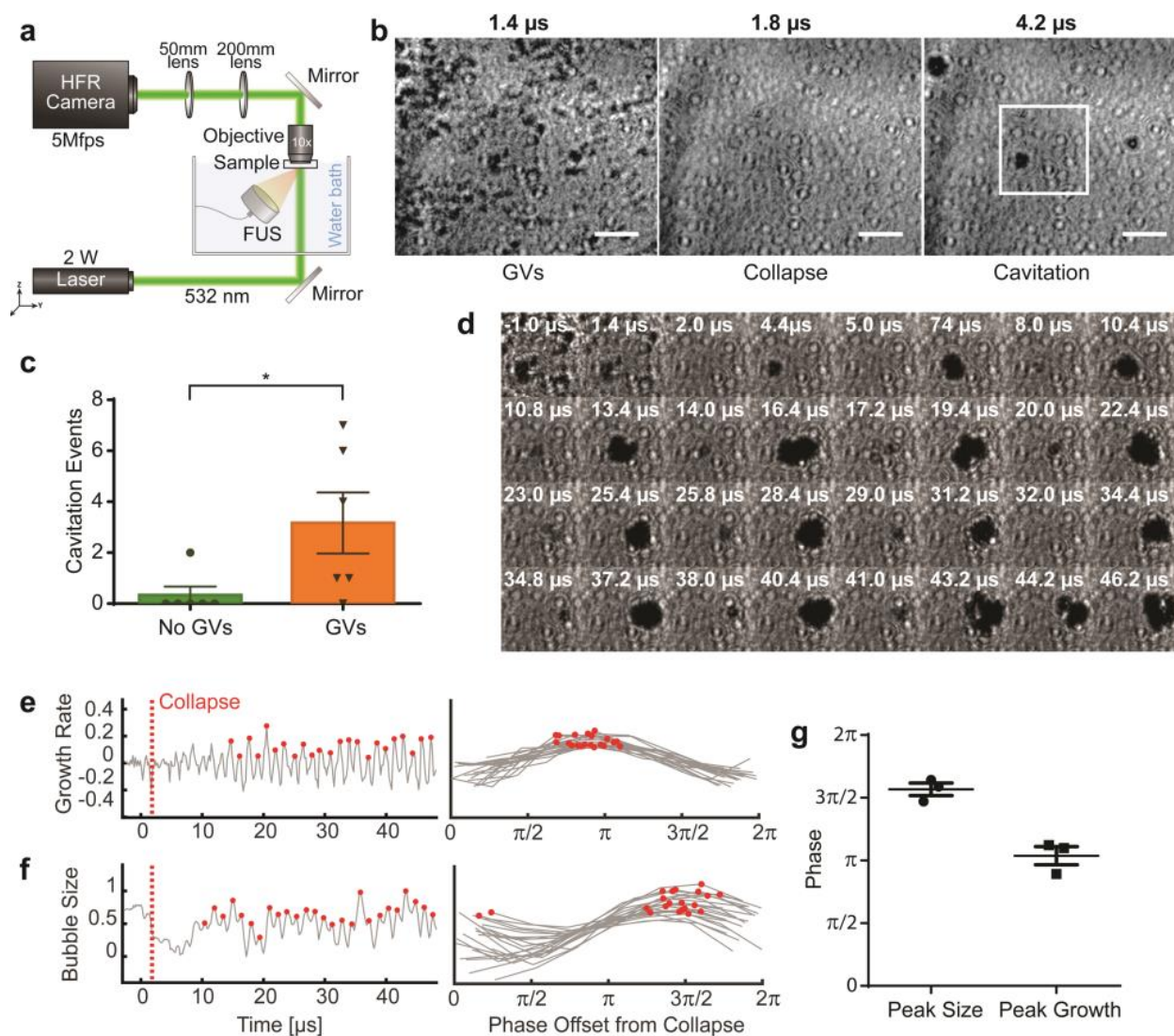


Figure 5-3 / Ultrafast optical imaging of GV-seeded bubble formation and cavitation

a, Schematic drawing of the high frame rate (HFR) camera setup enabling GV cavitation imaging at a frame rate of 5 MHz. b, HFR camera images immediately before GV collapse (left), immediately after GV collapse (middle), and after the formation of bubbles (right). c, Number of unique cavitation loci in biotinylated dishes with and without GVs, upon insonation with a single 1.4 MPa burst ($p= 0.0411$, $n=6$). FUS pulses with 30 cycles at 0.67 MHz were used unless otherwise stated. d, Representative high-speed camera frames showing every other maximum and minimum of bubble cavitation, preceded by GV collapse. e, Bubble growth rate, quantified as the

temporal derivative of the normalized average inverted pixel intensity in (d) (left). The plot on the right shows each maximum in the growth rate aligned to the phase offset from the time of GV collapse. f, Bubble size and phase offset from GV collapse analyzed from HFR images as in (e). g, Average phase offset for peak size and peak growth rate for three different regions of interest. Plots show mean \pm SEM (c, g). Scale bar represents 20 μ m (b).

5.3 High Intensity Focused Ultrasound for Thermal Control

5.3.1. Background

I also had the opportunity to work on a project with Mohamad Abedi on a currently unpublished project that uses ultrasound to activate thermally controlled genetic circuits *in vivo*. This project leverages high intensity ultrasound's capability to cause a local increase in temperature in biological tissue. While the results from this project are unpublished, I have cleared with the authors that the following limited information about my involvement in the project can be included in this dissertation.

Many biological processes are highly heat sensitive. At temperatures above 40-47 °C, cells begin suffering from hyperthermia with the initiation of several cell death pathways including heat-induced apoptosis, alterations in proteins that support DNA metabolism and mitosis, and generalized unfolding and aggregation of proteins. The effects are significantly more profound above 43 °C, with an exponential increase in the cell damage and decrease in cell survival times as temperature increases. Temperatures above 48 °C causes thermal ablation or irreversible widespread protein unfolding [120]. Thermal ultrasound ablation techniques, such as high intensity focused ultrasound, causes hyperthermia of above 60 °C which leads to complete coagulative necrosis in that area. However, cells have the capability to reverse the damage from mild hyperthermia through the activity of heat shock proteins [121]. The protein's expression is regulated by heat shock promoters in the DNA that initiate expression in response to increased temperatures. These proteins then initiate a variety of cytoprotective pathways. However, of

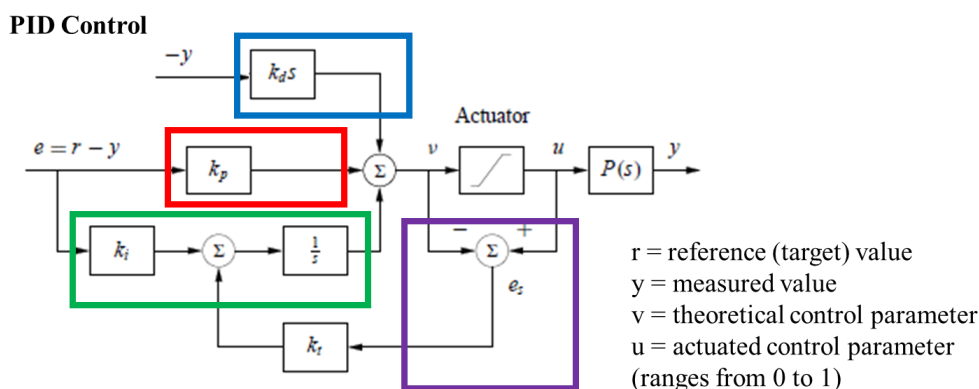
interest to many ultrasound researchers is the potential for therapeutic modalities that take advantage of the heat shock promoter's ability to control gene expression in response to temperature. Couple with noninvasive ultrasound, this allows for a completely noninvasive method of controlling genetic expression, at depth within the body. This has many advantages over other attempts to control genetic expression at depth, such as optogenetics, as ultrasound has greater penetration depth than light does in the human body.

5.3.2 Thermal Control with PID Circuit

My role in this project was to develop the *in vivo* experimental rig and help to optimize the ultrasound parameters in order to activate a genetic circuit based on native heat shock promoters placed within a bacterial agent living in tumors in an immunocompromised mouse model. Details about the bacterial agent and genetic circuit are omitted prior to publication. The experimental suspended the mouse in a temperature regulated and degassed water bath maintained at room temperature. A 0.67 MHz HIFU transducer was also placed in the water bath and targeted at a target tumor positioned on the lateral flank of the mouse. A small temperature sensitive fiber optic element was placed in the center of the tumor, and used to align the HIFU transducer.

In order to achieve the desired bioeffects, we needed to precisely and dynamically control the temperature of the tumor. We developed a confidential temperature activation sequence that we found activated the temperature sensitive genetic circuit. As such, we needed to develop a control system that allowed for rapid and accurate adjustment of the ultrasound waveform that was supplying the heat to adjust the tissue temperature. The system we developed was a PID controller with anti-windup. This system controlled the driving voltage for the HIFU transducer, which correlates with peak-negative-pressure, in order to cause the measured tumor temperature to track with a certain reference temperature that tracked with our temperature activation sequence. The ultrasound waveform used for thermal control was a continuous wave signal with the peak negative pressure being actively modulated by a PID control circuit in order to achieve a desired temperature in the targeted tissues (Figure 5-4). This technique has shown promising *in vivo* results that I look forward to sharing once this article is published. This application of ultrasound

required the use of an invasive temperature probe for the temperature feedback required for running the PID controller. This was effective for this proof of concept of the temperature activation sequence and the genetic circuit. However, in a clinically deployable application, we would likely use a non-invasive thermometry technique, such as MRI-thermometry which takes advantage of the temperature sensitive of MRI contrast within the human body [122].



Proportional control = $K_p * (r - y)$, causes rapid convergence to reference value

Integral control = $K_i * \int (r - y) dt$, eliminates steady state error

Derivative control = $-K_d * dy/dt$, minimizes oscillations around reference value

Anti-windup control: $-K_t * \int (u - v) dt$, prevents overshoot

Figure 5-4 / PID Control System Used for Thermal Control

This schema for a PID control system with anti-windup control. The reference value (r) represents the temperature of the thermal activation sequence that we have developed. This value changes over time in accordance with the progression of the thermal activation sequence. The measured value (y) is the temperature measured from the fiber optic probe. The actuated control parameter (u) represents the fraction of maximum voltage that is used to drive the ultrasound transducer. The peak negative pressure of the HIFU is directly proportional to the transducer driving voltage.

Chapter 6

CONCLUSIONS AND FUTURE EXPERIMENTS

6.1 Introduction

In this final chapter, I will describe the conclusion of this investigation of the oncotripsy theory. I shall include plans that I have developed with collaborators for future experiments to investigate the mechanism and applicability of oncotripsy theory. These include further high speed camera investigations of the role of cavitation and cell deformation in response to ultrasound, an investigation of this procedure being applied to solid tumor contexts *in vitro* and *in vivo*, and the potential for combinatorial therapy with chemotherapeutics or immunotherapeutics.

6.2 Investigation of the Mechanism of Oncotripsy

The experiments outlined in this thesis suggest that cancer-cell selective ablation can be achieved through the use of low intensity pulsed ultrasound applied at specific frequencies and pulse durations in suspension. Subsequent experiments suggested that this effect requires the ultrasound field to be in the form of standing waves and that cavitation played a mechanistically essential role in the cytodisruptive effect. The theory we propose is that the standing waves promote the formation of aggregated cavitation nuclei within the cell suspension, which then cavitate in response to ultrasound stimulation. We hypothesized that this cavitation amplifies the acoustic signal of the incident ultrasound wave, thus exposing the cell to mechanical oscillation at the incident frequency and leading to the frequency-dependent cytodisruption described in the computational simulations referenced in this thesis. This hypothesis has several testable predictions that merit investigation.

First, while we observed non-linear acoustic scattering using passive cavitation detection, this gives limited information about the interaction between the cavitating phenomena and the cells

themselves. Visualization of the bubbles and their physical interaction with the cells would be highly instructive in further understanding the mechanistic role that cavitation plays in ultrasound oncotripsy. To this end, I suggest an experiment be performed using the high speed optical microscopy setup with 10 Mfps acquisition speed as described in Section 3.6.6. This microscope was effectively able to measure the oscillation of the cells in response to ultrasound, confirming no micron-scale deformation that was resolvable by the imaging system. The imaging cartridge used by the system (**Figure 3-3**) could be modified to ensure that a robust standing wave is being generated within the imaging chamber when ultrasound is applied on it. Then, video can be acquired at multiple locations throughout the imaging chambers to search for the dynamics of cavitating bubbles. Micron size bubbles can be easily observed and measured using this setup, as depicted in **Figure 5-3**. The radius over time of the cavitating bubbles and the bubbles distance from the surrounding cells may thus be assessed. Appendix A includes a brief computational study using the Keller-Miksis equation to predict the cavitation bubble size and bubble distance from surrounding cells necessary to achieve a scattered cavitation signal that amplifies the incident ultrasound wave. This simulation predicts that bubble sizes should be on the order of micrometers may be necessary for significant signal amplification which should be visible on microscopy. However, there is some literature suggests that nano-bubble cavitation, especially stabilized by lipids, may also have mechanical transduction effects in biological tissue [123], so the absence of visible bubbles in the presence of a inertial cavitation signal detected by passive cavitation detection may be notable as well.

Further high speed microscopy experiments could provide further insight into the cytoskeletal cycle fatigue model predicted by the oncotripsy model as well. The images previously acquired lacked the contrast necessary to image intracellular elements. The insight that there was no micron-scale cellular deformation was made by observing the plasma membrane of the cell which was made visible using transmitted light microscopy using a laser illumination source. However, there are many ways to increase the image contrast to allow visualization of sub-cellular components. Pigment dyes such as methylene bind to the DNA of permeabilized cells [124], and may be applied immediately prior to insonation to visualize nuclear movement. Pigment dyes have the advantage of enhancing contrast in transmitted light microscopy setups, however, we

have done some preliminary experiments involving high speed fluorescence microscopy using a photo-multiplier tube intensifier as described in Figure 6-1.

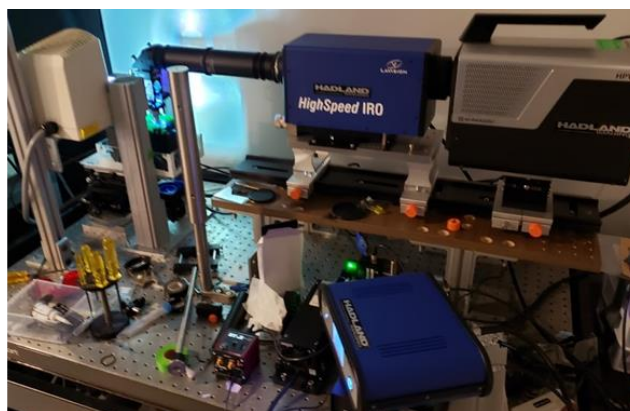
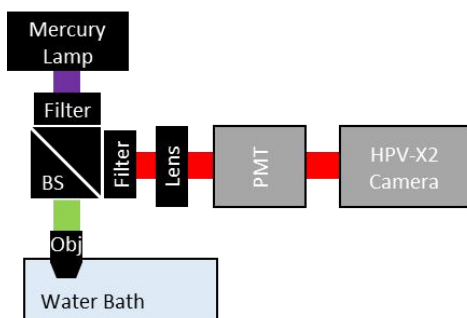


Figure 6-1 / Proposed setup for high speed fluorescence imaging

Epifluorescence imaging performed using mercury lamp illumination (Atlanta Light Bulb) and a Chroma EGFP filter set (Chroma #IN005873) that passed through water immersion microscope objective and concentrated on biological sample within water bath. Emitted fluorescent light was amplified through the use of the LaVision HighSpeed IRO intensifier, which coupled to the Shimadzu HPV-X2 camera.

In our exploratory experiments, the high speed camera used for the transmitted light microscopy (Shimadzu HPV-X2 camera) had insufficient sensitivity to detect the epi-fluorescence signal from powerful Alexa fluorophore dyes when 100 ns exposure time required for high speed imaging. With the introduction of the IRO intensifier running at maximum brightness and intensifier gain, we were able to get a very grainy image of 5 μm diameter AlexaFluor polystyrene beads at 200 ns exposure time. Future experiments may use more powerful fluorescent tags, such as quantum dots [125, 126], or aim to refine the fluorescent microscopy setup through collaborations with laboratory groups that have perfected the procedure [127]. Fluorescent microscopy would enable the use of fluorescent dyes that could be tagged to the sub-cellular

components. This could allow tracking of the differential movement of the nuclear membrane and cytoplasmic membranes, which would provide greater insight into the mechanical transduction of acoustic energy into the cell and perhaps validate the theory of cyclic fatigue being applied to the cell's cytoskeleton. Fluorophores may also allow tracking of cytoskeletal elements and be able to document cytoskeletal disassembly during insonation.

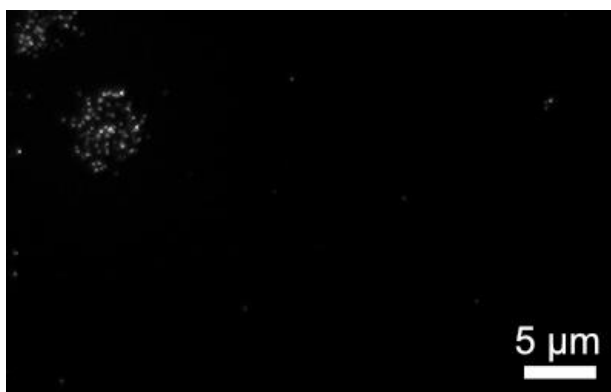


Figure 6-2 / Poor image acquisition of fluorescent dyes with high speed microscopy

Image of 5 µm diameter AlexaFluor polystyrene bead (upper left) from 200 ns exposure with 100x water immersion objective using epifluorescence microscopy setup described in Figure 6-1

In summary, the use of high speed microscopy, especially when coupled with strategies to enhance the contrast of sub-cellular components, can provide evidence to test the theory of cell-mediated cavitation leading to cytodisruption through incident ultrasound signal amplification and cytoskeletal cyclic fatigue.

6.3 Application of Oncotripsy to Solid Tumor Models

While oncotripsy provides a framework for developing a LIPUS waveform that has proven cancer selectivity in suspension cells, there are still many steps that must be taken before it can be considered as a serious clinical tool. The capability for oncotripsy theory to hold in solid tumor context must be investigated as well. The tumor microenvironment is heavily defined by the

extracellular matrix that cancer cells reside within. This extracellular matrix is comprised of a mechanically complex environment of macromolecules including collagen, elastin, and proteoglycan that has significant implications for disease progression [128]. Moreover, the cells are interconnected within this extracellular matrix and thus mechanical forces that are applied on the matrix are transduced to the cells and have documented effects on intracellular processes [129]. When considering the effect of acoustic waves on cells, it thus seems extremely important to incorporate the mechanical properties of the extra-cellular matrix. The transient response model developed by Heyden incorporated the extracellular matrix as an elastic continuum within which the cells resided. The finite element model developed in this framework still did exhibit a frequency-dependent cellular response to ultrasound. However, the first experimental investigation of this effect was primarily in suspension cells. One experiment performed with the cancer cells suspended in a solid medium of agarose, which is a poor model for the complex and interconnected tumor extra-cellular matrix environment, demonstrated only that the same waveform that induces cytodisruption in suspension induces a greatly attenuated effect in agarose. This result could be predicted in that the change in the extra-cellular mechanical properties should change the cells inherent mechanical response to ultrasound. Dedicated research in solid tumor contexts are necessary to further this understanding, and are currently being undertaken by Jian Ye and Dr. Peter Lee's group in City of Hope. Solid models can be developed *in vitro* using collagen-agarose hydrogels that simulate the mechanical properties of tumor tissue [31, 32] or through more complex models involving spheroids [130, 131] or *ex vivo* tissue samples. Alternatively, we may find it useful to jump to pre-clinical mice models, which limit the potential throughput of experimentation, but may serve as an early check to confer the viability of ultrasound oncotripsy as a valid method for cancer therapy in relevant clinical contexts.

6.4 Synergistic capabilities of oncotripsy with chemotherapy and immunotherapy

Secondly, safely implementing oncotripsy as a non-invasive, inherently selective cancer ablation system has remarkable potential in its synergistic capabilities with current therapeutic modalities. Oncotripsy theory would predict that cancer cells would be exposed to greater cytoskeletal damage from LIPUS compared to healthy cells at target waveforms. Cytoskeletal

damage may correspond to increased membrane permeability to chemotherapeutics. Pharmaceutical companies must overcome inherent challenges in cellular drug uptake and balance drug potency versus non-specific effects. Numerous anti-cancer drugs, including large protein biologics, must enter into the cellular cytoplasm in order to be effective. Moreover, research performed on the mechanical side effects of high intensity focused ultrasound (HIFU) suggests that mechanical ultrasound ablation releases antigens that may activate a systemic immune response [132]. Our *in vitro* experimental evidence included enhanced pro-phagocytic and apoptotic pathways are activated by LIPUS, which lends credence to this potential for combined therapy. As such, there may be a role for immunotherapy drugs that assist in the formation of a systemic anti-neoplastic immune response, such as anti-PD1 or TLR9 [104]. As such, a key next step for the oncotripsy project includes testing the hypothesis of enhanced chemotherapeutic uptake in cancer cells by observing synergy between chemotherapeutic agents and LIPUS cytodisruption. Next, we should investigate whether LIPUS-killed cancer cells can confer protective immunity in an immunocompetent mouse model. This can be done with cancer cells killed *in vitro* and then injected into the mouse as described in [133], or once the ideal ultrasound parameters for *in vivo* cytodisruption are determined, LIPUS could be applied *in vivo* while the effect on a contra-lateral non-treated tumor could be observed as a metric for systemic immune response.

6.5 Closed loop device for tuning oncotripsy parameters

Finally, a future goal for oncotripsy may involve recognizing the patient-to-patient variability inherent in any cancer therapeutic technique and developing a combined non-invasive imaging and therapeutic system that can apply the optimum US parameters for oncotripsy. We have access to several elastography systems that can be used to non-invasively probe the mechanical properties of tissue such as US elastography or magnetic resonance elastography [134]. The Shapiro lab has experience with elastography imaging. Such techniques can be performed on *in vitro* / *ex vivo* samples [135] or within *in vivo* contexts without requiring invasive biopsies [136]. We plan to perform high-resolution scans using various imaging modalities and correlate the imaging results with *in vitro* and *in vivo* cell disruption as assessed through our previously

validated models. We hypothesize that patterns from these scans can be correlated to the parameters necessary for targeted therapy. This would be the first step to developing a closed-loop device that can apply targeted therapy to account for cancer pleomorphism.

6.6 Conclusion

A non-invasive US system that can selectively increase the membrane permeability of target cells to uptake the drug of interest and enhance the local immune response through epitope release could have a massive synergistic effect in combined therapy. This therapy could have significant clinical benefits, particularly in clinically challenging tumors such as glioblastoma multiforme, where tumor invasion make complete surgical resection challenging and drug uptake can be poor [70]. Combining local surgical resection with regional oncotripsy that selectively targets rogue cancer cells and systemic chemotherapy/immunotherapy could remove the bulk tumor and address micro-metastasis that lead to recurrence.

APPENDIX A: KELLER-MIKSIS SIMULATION OF CAVITATING BUBBLE IN ULTRASOUND FIELD

The Keller-Miksis equation is a differential equation that describes the large radial oscillations of a bubble in a continuum of liquid that is exposed to an acoustic pressure field. This particular model suits our investigation of bubble cavitation in long pulse duration ultrasound fields, at our pressure and frequency ranges, and as such will be a good approximation for what can be expected in future experimental work investigating the oncotripsy method [137]. Our goal for this simulation is to determine whether the ultrasound waveform that was measured to induce cancer-cells selective cytodisruption (0.5 MHz, 1.4 MPa PNP due to standing wave condition) can stimulate a bubble to emit an acoustic signal that would act to amplify the 0.5 MHz mechanical signal a nearby cell would experience.

We will use the protocol described here [138] in order to model the acoustic emission of a cavitating bubble using the following set of equations:

$$\left(1 - \frac{\dot{R}}{c}\right) R\ddot{R} + \left(\frac{3}{2} - \frac{\dot{R}}{2c}\right) \dot{R}^2 = \frac{1}{\rho} \left(1 + \frac{\dot{R}}{c}\right) p_w + \frac{R}{\rho c} \frac{dp_w}{dt}, \quad (1)$$

R = instantaneous bubble radius, as a function of time

t = time

c = speed of sound in media

ρ = density of water

p_w = pressure at bubble wall

$$p_w = \left(P_0 + \frac{2\sigma}{R_0}\right) \left(\frac{R_0}{R}\right)^{3\kappa} - \frac{2\sigma}{R} - \frac{4\eta\dot{R}}{R} - P_0 - P_a \sin(\omega t), \quad (2)$$

σ = surface tension between gas-water interface

η = dynamic viscosity of water

R_0 = equilibrium radius

κ = polytropic exponent

P_a = pressure amplitude of the driving HIFU

$$P_{\text{rad}} = \rho \frac{R^2 \ddot{R} + 2R\dot{R}^2}{r}, \quad (3)$$

P_{rad} = acoustic emission

r = distance from the bubble center to the target location

Experimental data from [138] of bubble radius over time in response to similar ultrasound conditions is used to verify the validity of the Keller-Miksis equation in this context (**Figure A-1**).

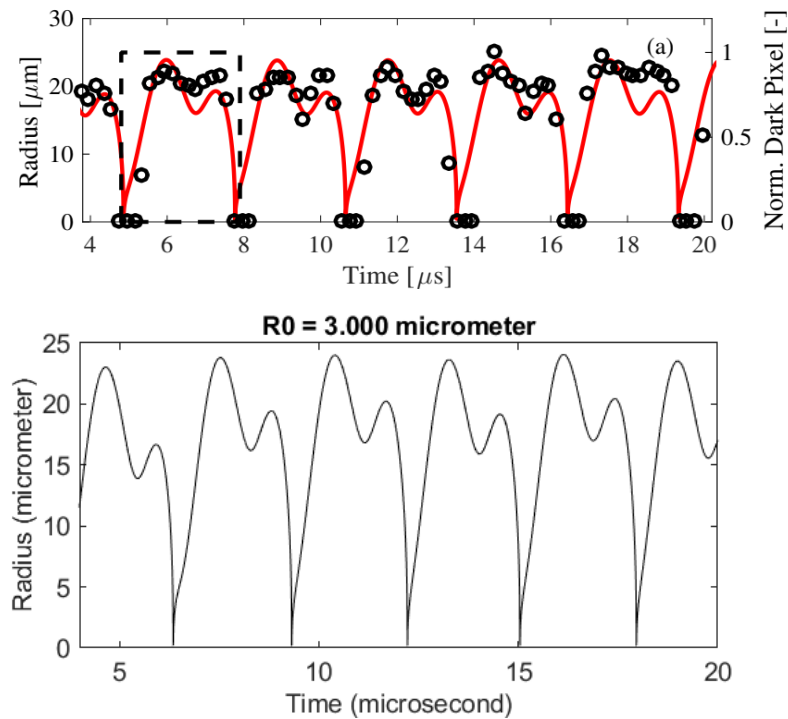


Figure A-1 / Validation of Keller-Miksis Model

Top graph reproduced from [138] includes experimental data for bubble radius over time for 1.31 MPa, 698 kHz HIFU applied on 3 μm bubbles with black circles and the Keller-Miksis model prediction in red. Bottom graph shows the Keller-Miksis model used in this appendix using $R=3 \mu\text{m}$, $\rho=998 \text{ kg/m}^3$, $\eta=1\text{e-}6 \text{ m}^2/\text{s}$, $\sigma=0.072 \text{ N/m}$, $c=1484 \text{ m/s}$, $P_0=101 \text{ kPa}$, $P_a=1.31 \text{ MPa}$ showing strong agreement with experimental data and published Keller-Miksis models.

For this simulation, we will test a range of bubble sizes with radii in the nanometer and micrometer scale, and assess the pressure emitted at distances ranging from the micrometer to millimeter scale. This will provide insight into whether pressure emissions from these cavitating bubbles will serve to amplify the input ultrasound signal and lead to frequency dependent cytodisruption.

	Name	Value
	<i>Variables</i>	
T	time	[s]
R(t)	instantaneous bubble radius	[m]
$p_w(R,t)$	pressure at bubble wall	[Pa]
$P_{rad}(R,t)$	pressure acoustic emission	[Pa]
	<i>Constants</i>	
c	speed of sound in media	1500 m/s
ρ	density of water	997 kg/m ³
σ	surface tension between gas-water interface	72.86 mN/m
κ	polytropic exponent	1.4 (adiabatic expansion)
P_a	pressure amplitude of the driving HIFU	1.4 MPa
η	dynamic viscosity of water	1.004 * 10 ⁻⁶ m ² /s
	<i>Sweep Parameters</i>	
R_0	equilibrium radius	10 ⁻⁸ – 10 ⁻⁵ m
r	distance from the bubble center to the target location	10 ⁻⁶ – 10 ⁻² m

Table A-1 / Variables and Coefficients for Keller-Miksis Simulation

Using this Keller-Miksis model, we can simulate the frequency spectra of the acoustic emissions with various equilibrium radius bubbles at various distances from the bubble center. The code for this simulation is available in the GitHub referenced in Appendix B. Matlab's stiff

ordinary differential equation solver, ODE15s, was used to solve the differential equation described by equations (1) and (2) to determine the bubble radius and its derivative over time after exposure to insonation. A simplifying simplification of a non-viscous fluid. These values were used to calculate the acoustic emission of the bubble at various distances using equation (3). The 0.5 MHz component of the acoustic emission at a specific distance from the cavitating bubbles was compared to that of the applied ultrasound signal.

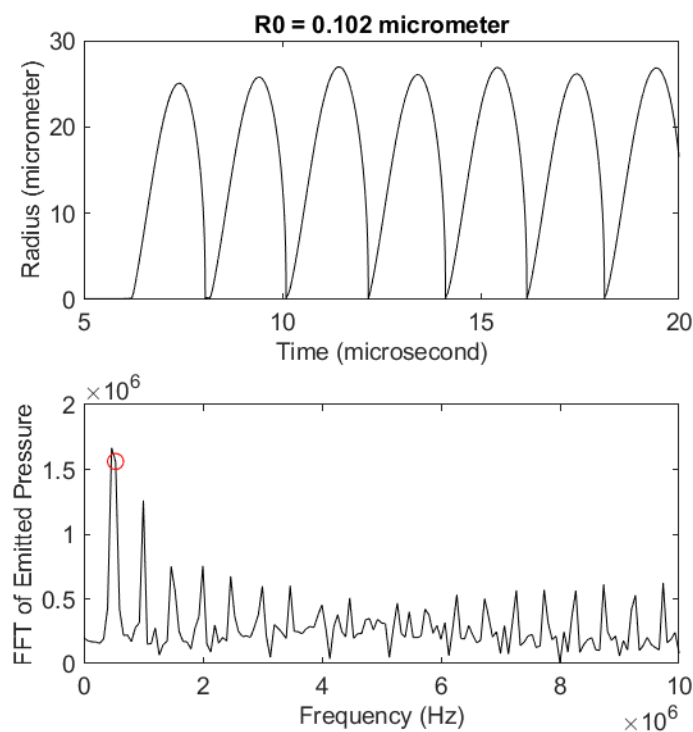


Figure A-2 / Keller-Miksis Simulated Cavitating Bubble Evolution and Pressure Emission

Keller-Miksis simulation results showing evolution of radius over time given an initial radius of 0.102 micrometers and the FFT of the pressure produced from that signal. This demonstrates the highly nonlinear response to ultrasound stimulation and the large variation in bubble size.

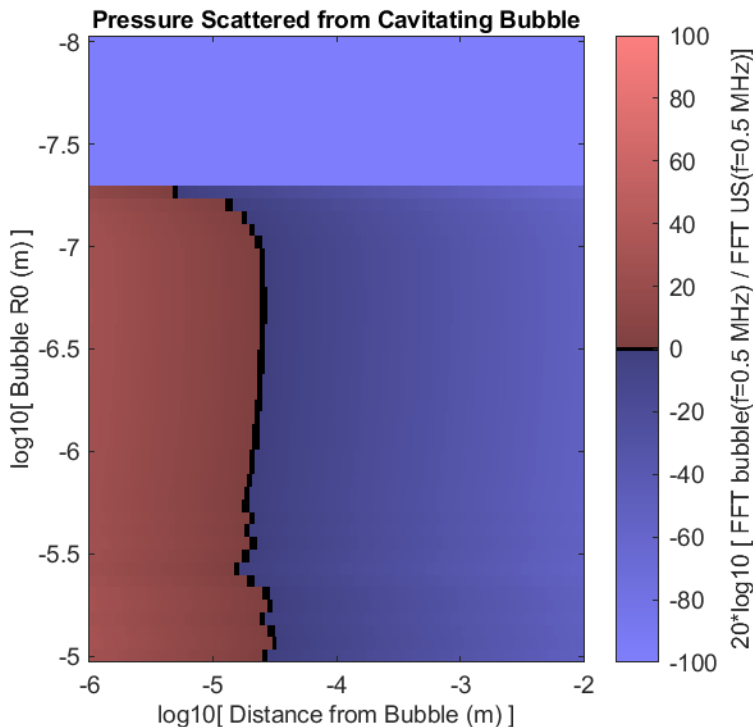


Figure A-3 / Keller-Miksis Simulated Amplification of Incident Ultrasound Pressure

Keller-Miksis simulation results showing decibel gain in the 0.5 MHz FFT of the pressure emissions from cavitating bubbles compared to the stimulating ultrasound signal. Initial bubble radius on the y-axis and distance from the bubble on the x-axis. In red regions the cavitating bubble's emitted pressure has a larger FFT signal at the stimulation frequency than the ultrasound signal.

The simulation results (**Figure A-3**) suggest that bubbles with radii greater than ~ 100 nm evoke pressure emissions that amplify the driving ultrasound signal within ~ 10 μm . While bubbles in this initial size range may be challenging to detect via optical microscopy, the simulation suggests that the bubble size may greatly expand during insonation. A bubble radius beginning at 0.1 μm may grow to 25 μm during insonation, which would be easily detectable through microscopy techniques (**Figure A-2**).

As such, further experiments using high speed microscopy could observe and track the cavitation bubbles radii over time during ultrasound stimulation. This could be used to calculate the pressure field that cells experience during insonation and correlate that with the cytodisruption caused by oncotripsy. An important finding to consider is that while the cavitating bubble primarily amplifies the driving signal at the driving frequency of the ultrasound, the emitted pressure signal does not solely contain that frequency. Instead, there are multiple harmonic peaks present on the FFT spectrum for pressure emitted from the cavitating bubble, which is an expected finding considering that cavitation is an inherently non-linear response. Future oncotripsy computational studies that model the cellular response to this phenomenon may want to consider this more complex pressure waveform, rather than the single frequency sinusoidal waveform of the driving ultrasound signal.

APPENDIX B: SCRIPTS, PROTOCOLS, AND MODELS ON GITHUB

For the reference of any experimenters who wish to adapt some of the computer scripts, experimental protocols, or CAD models that I have developed throughout my work on this project, please see attached to thesis archived versions of the following entries in the CaltechDATA repository:

<u>oncotripsy</u>	This repository includes scripts that simulate cavitating bubbles' amplification of incident ultrasound pressure waves.
<u>ultrasound_hardware_control</u>	Scripts that allow the user to conduct ultrasound experiments
<u>ultrasound_rigs</u>	Solidworks models that may be useful in designing ultrasound experimental rigs.
<u>thermal_control</u>	This repository includes scripts that allow the user to conduct thermal ultrasound experiments with closed loop control using a PID with anti-windup control system.

Updated versions of these repositories are available on my personal Github page:
<https://github.com/drmittelstein>

REFERENCES

1. Schirmmacher, V., *From chemotherapy to biological therapy: A review of novel concepts to reduce the side effects of systemic cancer treatment (Review)*. Int J Oncol, 2019. **54**(2): p. 407-419.
2. Sonnenblick, A. and M. Piccart, *Adjuvant systemic therapy in breast cancer: quo vadis?* Ann Oncol, 2015. **26**(8): p. 1629-34.
3. Lu, Z.R. and P. Qiao, *Drug Delivery in Cancer Therapy, Quo Vadis?* Mol Pharm, 2018. **15**(9): p. 3603-3616.
4. Frangioni, J.V., *New technologies for human cancer imaging*. J Clin Oncol, 2008. **26**(24): p. 4012-21.
5. Mohammadzadeh, N. and R. Safdari, *Robotic surgery in cancer care: opportunities and challenges*. Asian Pac J Cancer Prev, 2014. **15**(3): p. 1081-3.
6. Teicher, B.A., *Perspective: Opportunities in recalcitrant, rare and neglected tumors*. Oncol Rep, 2013. **30**(3): p. 1030-4.
7. Chakraborty, S. and T. Rahman, *The difficulties in cancer treatment*. Ecancermedicallscience, 2012. **6**: p. ed16.
8. J.C. Murray, J.C., *Targeting solid tumours: challenges, disappointments, and opportunities*. Advanced Drug Delivery Reviews, 1995. **17**(1): p. 117-127.
9. Seo, J. and Y.S. Kim, *Ultrasound imaging and beyond: recent advances in medical ultrasound*. Biomed Eng Lett, 2017. **7**(2): p. 57-58.
10. Tempny, C.M., et al., *Focused ultrasound surgery in oncology: overview and principles*. Radiology, 2011. **259**(1): p. 39-56.
11. Jagannathan, J., et al., *High-intensity focused ultrasound surgery of the brain: part 1--A historical perspective with modern applications*. Neurosurgery, 2009. **64**(2): p. 201-10; discussion 210-1.
12. Meyers, R., et al., *Early experiences with ultrasonic irradiation of the pallidofugal and nigral complexes in hyperkinetic and hypertonic disorders*. J Neurosurg, 1959. **16**(1): p. 32-54.
13. Lynn, J.G., et al., *A New Method for the Generation and Use of Focused Ultrasound in Experimental Biology*. J Gen Physiol, 1942. **26**(2): p. 179-93.
14. Miller, D.L., et al., *Overview of therapeutic ultrasound applications and safety considerations*. J Ultrasound Med, 2012. **31**(4): p. 623-34.
15. Tailly, G.G., *Extracorporeal shock wave lithotripsy today*. Indian J Urol, 2013. **29**(3): p. 200-7.
16. Jessica L Foley, M.E., John Snell, Arik Hananel, Neal Kassell & Jean-Francois Aubry, *Image-guided focused ultrasound: state of the technology and the challenges that lie ahead*. Imaging in Medicine, 2013. **5**(4).
17. Burgess, A., et al., *High-intensity focused ultrasound (HIFU) for dissolution of clots in a rabbit model of embolic stroke*. PLoS One, 2012. **7**(8): p. e42311.
18. Pitt, W.G., G.A. Hussein, and B.J. Staples, *Ultrasonic drug delivery--a general review*. Expert Opin Drug Deliv, 2004. **1**(1): p. 37-56.

19. Hobbie, R.K. and B.J. Roth, *Sound and Ultrasound*, in *Intermediate Physics for Medicine and Biology*. 2007, Springer New York: New York, NY. p. 343-357.
20. Cox, B., *Acoustics for Ultrasound Imaging*. 2013.
21. Hynynen, K. and R.M. Jones, *Image-guided ultrasound phased arrays are a disruptive technology for non-invasive therapy*. *Phys Med Biol*, 2016. **61**(17): p. R206-48.
22. Carovac, A., F. Smajlovic, and D. Junuzovic, *Application of ultrasound in medicine*. *Acta Inform Med*, 2011. **19**(3): p. 168-71.
23. Dewall, R.J., *Ultrasound elastography: principles, techniques, and clinical applications*. *Crit Rev Biomed Eng*, 2013. **41**(1): p. 1-19.
24. Tufail, Y., et al., *Ultrasonic neuromodulation by brain stimulation with transcranial ultrasound*. *Nat Protoc*, 2011. **6**(9): p. 1453-70.
25. Blackmore, J., et al., *Ultrasound Neuromodulation: A Review of Results, Mechanisms and Safety*. *Ultrasound Med Biol*, 2019. **45**(7): p. 1509-1536.
26. Hersh, D.S., et al., *Emerging Applications of Therapeutic Ultrasound in Neuro-oncology: Moving Beyond Tumor Ablation*. *Neurosurgery*, 2016. **79**(5): p. 643-654.
27. Hsiao, Y.H., et al., *Clinical Application of High-intensity Focused Ultrasound in Cancer Therapy*. *J Cancer*, 2016. **7**(3): p. 225-31.
28. Zhang, M., et al., *Effects of high-intensity focused ultrasound for treatment of abdominal lymph node metastasis from gastric cancer*. *J Ultrasound Med*, 2015. **34**(3): p. 435-40.
29. Unga, J. and M. Hashida, *Ultrasound induced cancer immunotherapy*. *Adv Drug Deliv Rev*, 2014. **72**: p. 144-53.
30. Van Leenders, G.J., et al., *Histopathological changes associated with high intensity focused ultrasound (HIFU) treatment for localised adenocarcinoma of the prostate*. *J Clin Pathol*, 2000. **53**(5): p. 391-4.
31. Couture, O., et al., *Review of ultrasound mediated drug delivery for cancer treatment: updates from pre-clinical studies*. *Translational Cancer Research*, 2014. **3**(5): p. 494-511.
32. Xu, Z.L., et al., *Activation of tumor-infiltrating antigen presenting cells by high intensity focused ultrasound ablation of human breast cancer*. *Ultrasound Med Biol*, 2009. **35**(1): p. 50-7.
33. Aubry, J.F., et al., *The road to clinical use of high-intensity focused ultrasound for liver cancer: technical and clinical consensus*. *J Ther Ultrasound*, 2013. **1**: p. 13.
34. McGahan, J.P., et al., *Hepatic ablation with use of radio-frequency electrocautery in the animal model*. *J Vasc Interv Radiol*, 1992. **3**(2): p. 291-7.
35. Malietzis, G., et al., *High-intensity focused ultrasound: advances in technology and experimental trials support enhanced utility of focused ultrasound surgery in oncology*. *Br J Radiol*, 2013. **86**(1024): p. 20130044.
36. Ghorbani, M., et al., *Review on Lithotripsy and Cavitation in Urinary Stone Therapy*. *IEEE Rev Biomed Eng*, 2016. **9**: p. 264-83.
37. Kelman, C.D., *Phaco-emulsification and aspiration. A new technique of cataract removal. A preliminary report*. *Am J Ophthalmol*, 1967. **64**(1): p. 23-35.
38. Khokhlova, V.A., et al., *Histotripsy methods in mechanical disintegration of tissue: towards clinical applications*. *Int J Hyperthermia*, 2015. **31**(2): p. 145-62.
39. Collis, J., et al., *Cavitation microstreaming and stress fields created by microbubbles*. *Ultrasonics*, 2010. **50**(2): p. 273-9.

40. Azagury, A., et al., *The synergistic effect of ultrasound and chemical penetration enhancers on chorioamnion mass transport*. J Control Release, 2015. **200**: p. 35-41.
41. Wolloch, L., et al., *Fetal membrane transport enhancement using ultrasound for drug delivery and noninvasive detection*. Pharm Res, 2015. **32**(2): p. 403-13.
42. Guck, J., et al., *Optical deformability as an inherent cell marker for testing malignant transformation and metastatic competence*. Biophys J, 2005. **88**(5): p. 3689-98.
43. Gal, N. and D. Weihs, *Intracellular mechanics and activity of breast cancer cells correlate with metastatic potential*. Cell Biochem Biophys, 2012. **63**(3): p. 199-209.
44. Williams, C.M. and K. Maunder, *Fatty acid compositions of inositol and choline phospholipids of breast tumours and normal breast tissue*. Eur J Clin Nutr, 1993. **47**(4): p. 260-7.
45. Azagury, A., et al., *Ultrasound Effect on Cancerous versus Non-Cancerous Cells*. Ultrasound Med Biol, 2016. **42**(7): p. 1560-7.
46. Wood, A.K. and C.M. Sehgal, *A review of low-intensity ultrasound for cancer therapy*. Ultrasound Med Biol, 2015. **41**(4): p. 905-28.
47. Yoshida, T., et al., *Combination of doxorubicin and low-intensity ultrasound causes a synergistic enhancement in cell killing and an additive enhancement in apoptosis induction in human lymphoma U937 cells*. Cancer Chemother Pharmacol, 2008. **61**(4): p. 559-67.
48. Nomikou, N., Y.S. Li, and A.P. McHale, *Ultrasound-enhanced drug dispersion through solid tumours and its possible role in aiding ultrasound-targeted cancer chemotherapy*. Cancer Lett, 2010. **288**(1): p. 94-8.
49. Li, H., et al., *Potential of scutellarin on human tongue carcinoma xenograft by low-intensity ultrasound*. PLoS One, 2013. **8**(3): p. e59473.
50. Wang, L.Y. and S.S. Zheng, *Advances in low-frequency ultrasound combined with microbubbles in targeted tumor therapy*. J Zhejiang Univ Sci B, 2019. **20**(4): p. 291-299.
51. Bar-Zion, A., et al., *Acoustically Detonated Biomolecules for Genetically Encodable Inertial Cavitation*. bioRxiv, 2019: p. 620567.
52. McLaughlan, J.R., et al., *Characterisation of Liposome-Loaded Microbubble Populations for Subharmonic Imaging*. Ultrasound Med Biol, 2017. **43**(1): p. 346-356.
53. Nelson, T.R., et al., *Ultrasound biosafety considerations for the practicing sonographer and sonologist*. J Ultrasound Med, 2009. **28**(2): p. 139-50.
54. Ye, P.P., J.R. Brown, and K.B. Pauly, *Frequency Dependence of Ultrasound Neurostimulation in the Mouse Brain*. Ultrasound Med Biol, 2016. **42**(7): p. 1512-30.
55. Feril, L.B., Jr., et al., *Therapeutic potential of low-intensity ultrasound (part 1): thermal and sonomechanical effects*. J Med Ultrason (2001), 2008. **35**(4): p. 153-60.
56. Della Rocca, G.J., *The science of ultrasound therapy for fracture healing*. Indian J Orthop, 2009. **43**(2): p. 121-126.
57. ter Haar, G.R. and D. Robertson, *Tissue destruction with focused ultrasound in vivo*. Eur Urol, 1993. **23 Suppl 1**: p. 8-11.
58. Shen, Z.Y., et al., *The effects of low-frequency ultrasound and microbubbles on rabbit hepatic tumors*. Exp Biol Med (Maywood), 2014. **239**(6): p. 747-57.
59. Wiklund, M., *Acoustofluidics 12: Biocompatibility and cell viability in microfluidic acoustic resonators*. Lab Chip, 2012. **12**(11): p. 2018-28.

60. Lekka, M., *Discrimination Between Normal and Cancerous Cells Using AFM*. Bionanoscience, 2016. **6**: p. 65-80.
61. van Diest, P.J., E. van der Wall, and J.P. Baak, *Prognostic value of proliferation in invasive breast cancer: a review*. J Clin Pathol, 2004. **57**(7): p. 675-81.
62. Cross, S.E., et al., *Nanomechanical analysis of cells from cancer patients*. Nat Nanotechnol, 2007. **2**(12): p. 780-3.
63. Ignatiadis, M., M. Lee, and S.S. Jeffrey, *Circulating Tumor Cells and Circulating Tumor DNA: Challenges and Opportunities on the Path to Clinical Utility*. Clin Cancer Res, 2015. **21**(21): p. 4786-800.
64. Halpern, P.H.G.a.S., *Nuclear-Nucleolar Volume Ratio in Cancer*. American Association for Cancer Research Journals, 1935. **25**(4): p. 802-806.
65. Venkatesh, S.K., et al., *Magnetic Resonance Elastography of Liver Tumors- Preliminary Results*. AJR Am J Roentgenol, 2008. **190**(6): p. 1534-40.
66. Schrader, J., et al., *Matrix stiffness modulates proliferation, chemotherapeutic response, and dormancy in hepatocellular carcinoma cells*. Hepatology, 2011. **53**(4): p. 1192-205.
67. Swaminathan, V., et al., *Mechanical stiffness grades metastatic potential in patient tumor cells and in cancer cell lines*. Cancer Res, 2011. **71**(15): p. 5075-80.
68. Pogoda, K., et al., *Compression stiffening of brain and its effect on mechanosensing by glioma cells*. New J Phys, 2014. **16**: p. 075002.
69. Kondziolka, D., et al., *The biology of radiosurgery and its clinical applications for brain tumors*. Neuro Oncol, 2015. **17**(1): p. 29-44.
70. Cohen-Inbar, O., Z. Xu, and J.P. Sheehan, *Focused ultrasound-aided immunomodulation in glioblastoma multiforme: a therapeutic concept*. J Ther Ultrasound, 2016. **4**: p. 2.
71. Bruix, J., M. Reig, and M. Sherman, *Evidence-based Diagnosis, Staging, and Treatment of Patients With Hepatocellular Carcinoma*. Gastroenterology, 2016.
72. Vauthey, J.-N., *Metastatic Cancer of the Liver*, in *Gastrointestinal Cancer*, J.A. Ajani, et al., Editors. 2005, Springer New York: New York, NY. p. 165-183.
73. Lee, H., et al., *Mechanical Properties of Normal Breast Cells and Metastatic Cancer Cells in Co-Culture*. Biophysical Journal. **112**(3): p. 124a.
74. Heyden, S. and M. Ortiz, *Oncotripsy: Targeting cancer cells selectively via resonant harmonic excitation*. JMPS (under review), 2016.
75. Miller, D.L., *Safety assurance in obstetrical ultrasound*. Semin Ultrasound CT MR, 2008. **29**(2): p. 156-64.
76. Mittelstein, D.R., et al., *Selective ablation of cancer cells with low intensity pulsed ultrasound*. Applied Physics Letters, 2020. **116**(1): p. 013701.
77. Hermine, O., J.C. Ramos, and K. Tobinai, *A Review of New Findings in Adult T-cell Leukemia-Lymphoma: A Focus on Current and Emerging Treatment Strategies*. Adv Ther, 2018. **35**(2): p. 135-152.
78. Watts, J. and S. Nimer, *Recent advances in the understanding and treatment of acute myeloid leukemia*. F1000Res, 2018. **7**.
79. Micalizzi, D.S., S. Maheswaran, and D.A. Haber, *A conduit to metastasis: circulating tumor cell biology*. Genes Dev, 2017. **31**(18): p. 1827-1840.
80. Osman, R., et al., *Calreticulin Release at an Early Stage of Death Modulates the Clearance by Macrophages of Apoptotic Cells*. Front Immunol, 2017. **8**: p. 1034.

81. Tsamandas, A.C., et al., *The potential role of Bcl-2 expression, apoptosis and cell proliferation (Ki-67 expression) in cases of gastric carcinoma and correlation with classic prognostic factors and patient outcome*. *Anticancer Res*, 2009. **29**(2): p. 703-9.
82. Noriega, S., G. Hasanova, and A. Subramanian, *The effect of ultrasound stimulation on the cytoskeletal organization of chondrocytes seeded in three-dimensional matrices*. *Cells Tissues Organs*, 2013. **197**(1): p. 14-26.
83. Samandari, M., et al., *Ultrasound induced strain cytoskeleton rearrangement: An experimental and simulation study*. *J Biomech*, 2017. **60**: p. 39-47.
84. Carugo, D., et al., *Contrast agent-free sonoporation: The use of an ultrasonic standing wave microfluidic system for the delivery of pharmaceutical agents*. *Biomicrofluidics*, 2011. **5**(4): p. 44108-4410815.
85. Leskinen, J.J. and K. Hynynen, *Study of factors affecting the magnitude and nature of ultrasound exposure with in vitro set-ups*. *Ultrasound Med Biol*, 2012. **38**(5): p. 777-94.
86. Qiu, Y., et al., *Acoustic devices for particle and cell manipulation and sensing*. *Sensors (Basel)*, 2014. **14**(8): p. 14806-38.
87. Hwang, J.H., et al., *Correlation between inertial cavitation dose and endothelial cell damage in vivo*. *Ultrasound Med Biol*, 2006. **32**(10): p. 1611-9.
88. Williams, J.C., Jr., et al., *Effect of macroscopic air bubbles on cell lysis by shock wave lithotripsy in vitro*. *Ultrasound Med Biol*, 1999. **25**(3): p. 473-9.
89. Sapozhnikov, O.A., et al., *Effect of overpressure and pulse repetition frequency on cavitation in shock wave lithotripsy*. *J Acoust Soc Am*, 2002. **112**(3 Pt 1): p. 1183-95.
90. Bailey, M.R., et al., *Use of overpressure to assess the role of bubbles in focused ultrasound lesion shape in vitro*. *Ultrasound Med Biol*, 2001. **27**(5): p. 695-708.
91. Heyden, S. and M. Ortiz, *Investigation of the influence of viscoelasticity on oncotripsy*. *Computer Methods in Applied Mechanics and Engineering*, 2017. **314**(Supplement C): p. 314-322.
92. Heyden, S. and M. Ortiz, *Oncotripsy: Targeting cancer cells selectively via resonant harmonic excitation*. *Journal of the Mechanics and Physics of Solids*, 2016. **92**: p. 164-175.
93. Heyden, S. and M. Ortiz, *Investigation of the influence of viscoelasticity on oncotripsy*. *Computer Methods in Applied Mechanics and Engineering*, 2017. **314**: p. 314-322.
94. Paoletti, C., et al., *Significance of Circulating Tumor Cells in Metastatic Triple-Negative Breast Cancer Patients within a Randomized, Phase II Trial: TBCRC 019*. *Clin Cancer Res*, 2015. **21**(12): p. 2771-9.
95. Apetoh, L., et al., *Toll-like receptor 4-dependent contribution of the immune system to anticancer chemotherapy and radiotherapy*. *Nat Med*, 2007. **13**(9): p. 1050-9.
96. Michaud, M., et al., *Autophagy-dependent anticancer immune responses induced by chemotherapeutic agents in mice*. *Science*, 2011. **334**(6062): p. 1573-7.
97. Casares, N., et al., *Caspase-dependent immunogenicity of doxorubicin-induced tumor cell death*. *J Exp Med*, 2005. **202**(12): p. 1691-701.
98. Mattarollo, S.R., et al., *Pivotal role of innate and adaptive immunity in anthracycline chemotherapy of established tumors*. *Cancer Res*, 2011. **71**(14): p. 4809-20.
99. DeNardo, D.G., et al., *Leukocyte complexity predicts breast cancer survival and functionally regulates response to chemotherapy*. *Cancer Discov*, 2011. **1**(1): p. 54-67.

100. Denkert, C., et al., *Tumor-associated lymphocytes as an independent predictor of response to neoadjuvant chemotherapy in breast cancer*. J Clin Oncol, 2010. **28**(1): p. 105-13.
101. Ladoire, S., et al., *In situ immune response after neoadjuvant chemotherapy for breast cancer predicts survival*. J Pathol, 2011. **224**(3): p. 389-400.
102. West, N.R., et al., *Tumor-infiltrating lymphocytes predict response to anthracycline-based chemotherapy in estrogen receptor-negative breast cancer*. Breast Cancer Res, 2011. **13**(6): p. R126.
103. Halama, N., et al., *Localization and density of immune cells in the invasive margin of human colorectal cancer liver metastases are prognostic for response to chemotherapy*. Cancer Res, 2011. **71**(17): p. 5670-7.
104. Silvestrini, M.T., et al., *Priming is key to effective incorporation of image-guided thermal ablation into immunotherapy protocols*. JCI Insight, 2017. **2**(6): p. e90521.
105. Tse, J.R. and A.J. Engler, *Preparation of hydrogel substrates with tunable mechanical properties*. Curr Protoc Cell Biol, 2010. **Chapter 10**: p. Unit 10 16.
106. Krasovitski, B., et al., *Intramembrane cavitation as a unifying mechanism for ultrasound-induced bioeffects*. Proc Natl Acad Sci U S A, 2011. **108**(8): p. 3258-63.
107. Li, P., et al., *Acoustic separation of circulating tumor cells*. Proc Natl Acad Sci U S A, 2015. **112**(16): p. 4970-5.
108. Guz, N., et al., *If cell mechanics can be described by elastic modulus: study of different models and probes used in indentation experiments*. Biophysical journal, 2014. **107**(3): p. 564-575.
109. E. F. Schibber, D.R.M., M. Gharib, M. G. Shapiro, P. P. Lee, M. Ortiz, *A Dynamical Model of Oncotripsy by Mechanical Cell Fatigue: Selective Cancer Cell Ablation by Low-Intensity Pulsed Ultrasound (LIPUS)*. arXiv, 2019.
110. Nowak, M.A., *Evolutionary dynamics*. 2006: Harvard University Press.
111. Shapiro, M.G., et al., *Biogenic gas nanostructures as ultrasonic molecular reporters*. Nat Nanotechnol, 2014. **9**(4): p. 311-6.
112. Lu, G.J., et al., *Acoustically modulated magnetic resonance imaging of gas-filled protein nanostructures*. Nat Mater, 2018. **17**(5): p. 456-463.
113. Pfeifer, F., *Distribution, formation and regulation of gas vesicles*. Nat Rev Microbiol, 2012. **10**(10): p. 705-15.
114. Walsby, A.E., *Gas Vesicles*. Annual Review of Plant Physiology, 1975. **26**(1): p. 427-439.
115. Lakshmanan, A., et al., *Molecular Engineering of Acoustic Protein Nanostructures*. ACS Nano, 2016. **10**(8): p. 7314-22.
116. Ferrara, K., R. Pollard, and M. Borden, *Ultrasound microbubble contrast agents: fundamentals and application to gene and drug delivery*. Annu Rev Biomed Eng, 2007. **9**: p. 415-47.
117. Ashokkumar, M., et al., *Bubbles in an acoustic field: an overview*. Ultrason Sonochem, 2007. **14**(4): p. 470-5.
118. Kwan, J.J., et al., *Ultrasound-Propelled Nanocups for Drug Delivery*. Small, 2015. **11**(39): p. 5305-14.

119. Walsby, A.E., *Gas-filled structures providing buoyancy in photosynthetic organisms*. Symp Soc Exp Biol, 1972. **26**: p. 233-50.
120. Roti Roti, J.L., *Cellular responses to hyperthermia (40-46 degrees C): cell killing and molecular events*. Int J Hyperthermia, 2008. **24**(1): p. 3-15.
121. Wang, H.Y., et al., *Hyperthermia stress activates heat shock protein expression via propyl isomerase 1 regulation with heat shock factor 1*. Mol Cell Biol, 2013. **33**(24): p. 4889-99.
122. Zhu, M., Z. Sun, and C.K. Ng, *Image-guided thermal ablation with MR-based thermometry*. Quant Imaging Med Surg, 2017. **7**(3): p. 356-368.
123. Adhikari, U., A. Goliaei, and M.L. Berkowitz, *Nanobubbles, cavitation, shock waves and traumatic brain injury*. Phys Chem Chem Phys, 2016. **18**(48): p. 32638-32652.
124. Hu, X., et al., *A Simple and Efficient Method for Preparing Cell Slides and Staining without Using Cytocentrifuge and Cytoclips*. Int J Cell Biol, 2015. **2015**: p. 813216.
125. Chang, J.C. and S.J. Rosenthal, *Single quantum dot imaging in living cells*. Methods Mol Biol, 2013. **991**: p. 149-62.
126. Jaiswal, J.K., et al., *Use of quantum dots for live cell imaging*. Nat Methods, 2004. **1**(1): p. 73-8.
127. Gelderblom, E.C., et al., *Brandaris 128 ultra-high-speed imaging facility: 10 years of operation, updates, and enhanced features*. Rev Sci Instrum, 2012. **83**(10): p. 103706.
128. Suki, B. and J.H. Bates, *Extracellular matrix mechanics in lung parenchymal diseases*. Respir Physiol Neurobiol, 2008. **163**(1-3): p. 33-43.
129. Kalli, M. and T. Stylianopoulos, *Defining the Role of Solid Stress and Matrix Stiffness in Cancer Cell Proliferation and Metastasis*. Front Oncol, 2018. **8**: p. 55.
130. Aydin, O., et al., *Noninvasive Ablation of Prostate Cancer Spheroids Using Acoustically-Activated Nanodroplets*. Mol Pharm, 2016. **13**(12): p. 4054-4065.
131. Muenzner, J.K., et al., *Generation and characterization of hepatocellular carcinoma cell lines with enhanced cancer stem cell potential*. J Cell Mol Med, 2018. **22**(12): p. 6238-6248.
132. van den Bijgaart, R.J., et al., *Thermal and mechanical high-intensity focused ultrasound: perspectives on tumor ablation, immune effects and combination strategies*. Cancer Immunol Immunother, 2017. **66**(2): p. 247-258.
133. Humeau, J., et al., *Gold Standard Assessment of Immunogenic Cell Death in Oncological Mouse Models*, in *Cancer Immunosurveillance: Methods and Protocols*, A. López-Soto and A.R. Folgueras, Editors. 2019, Springer New York: New York, NY. p. 297-315.
134. Sarvazyan, A.P., et al., *Shear wave elasticity imaging: a new ultrasonic technology of medical diagnostics*. Ultrasound Med Biol, 1998. **24**(9): p. 1419-35.
135. Nicolas, E., et al., *Biomechanical characterization of ex vivo human brain using ultrasound shear wave spectroscopy*. Ultrasonics, 2018. **84**: p. 119-125.
136. Deffieux, T., et al., *Shear wave spectroscopy for in vivo quantification of human soft tissues visco-elasticity*. IEEE Trans Med Imaging, 2009. **28**(3): p. 313-22.
137. Hu, Z., J. Xu, and T.A. Bigelow, *Comparison of Gilmore-Akulichev's, Keller-Miksis's and Rayleigh-Plesset's equations on therapeutic ultrasound bubble cavitation*. The Journal of the Acoustical Society of America, 2014. **136**(4): p. 2280-2280.

138. Johansen, K., J.H. Song, and P. Prentice, *Validity of the Keller-Miksis equation for "non-stable" cavitation and the acoustic emissions generated*. 2017 Ieee International Ultrasonics Symposium (Ius), 2017.